



HAL
open science

Non reciprocal passive components on LTCC ferrite substrate

Shicheng Yang

► **To cite this version:**

Shicheng Yang. Non reciprocal passive components on LTCC ferrite substrate. Optics / Photonics. Université Jean Monnet - Saint-Etienne; Carleton university (Ottawa), 2015. English. NNT: 2015STET4020 . tel-01628200

HAL Id: tel-01628200

<https://theses.hal.science/tel-01628200>

Submitted on 3 Nov 2017

HAL is a multi-disciplinary open access archive for the deposit and dissemination of scientific research documents, whether they are published or not. The documents may come from teaching and research institutions in France or abroad, or from public or private research centers.

L'archive ouverte pluridisciplinaire **HAL**, est destinée au dépôt et à la diffusion de documents scientifiques de niveau recherche, publiés ou non, émanant des établissements d'enseignement et de recherche français ou étrangers, des laboratoires publics ou privés.



Thèse

Pour obtenir le grade de Docteur délivré par
L'UNIVERSITE JEAN MONNET DE SAINT ETIENNE
ET

Carleton University

Discipline: Optique, Photonique et Hyperfréquence

Présenté et soutenue publiquement

par

Shicheng YANG

Le 2 Octobre 2015

Composants passifs non réciproques hyperfréquences sur substrat ferrite LTCC

Non reciprocal passive components on LTCC ferrite substrate

JURY

O. PICON	Professeur, Université Paris-Est Marne-la-Vallée, France	Rapporteur
A. JACOB	Professeur, University Hamburg-Harburg, Germany	Rapporteur
L. ROY	Professeur, Carleton University, Canada	Directeur de thèse
J. R. BRAY	Professeur, Royal Military College, Canada	Examineur
R. AMAYA	Professeur Associé, Carleton University, Canada	Examineur
P. FERRARI	Université Joseph Fourier, France	Examineur
B. BAYARD	Maître de conférence HDR, Université Jean Monnet de Saint Etienne, France	Examineur
D. VINCENT	Professeur, Université Jean Monnet de Saint Etienne, France	Directeur de thèse

Abstract

This thesis investigates passive non-reciprocal components (mainly circulators) based on ferrite Low Temperature Co-fired Ceramic (LTCC) substrate. The external magnets used in conventional circulators must be strong to overcome the ferrite's demagnetization field. The novel circulator presented herein uses an embedded winding within the ferrite substrate to magnetize the material from the inside, thereby significantly reducing the demagnetization effects. Because of the controllability of the bias field, the resulting device is also multifunctional: when the windings are energized by a current, the device operates as a dynamic circulator in which the circulation direction can be changed by switching the direction of the current. Unlike other LTCC circulators with external magnets, the proposed device can even operate as a power splitter by removing the bias current. A circulator prototype has been characterized in three states: unbiased, biased by winding and biased by winding and external magnets. When no current is applied, the transmission of each port is about -5 dB with a return loss better than 20 dB at 14.8 GHz. When a current of 300 mA is injected into the winding, the measured insertion loss and isolation of the circulator is approximately 3 dB and 8 dB, respectively, whereas the return loss is better than 20 dB at 14.2 GHz. When external magnets are added in addition to the current of 200 mA, the insertion loss and isolation is improved to 1.6 dB and 23 dB, respectively at 14.2 GHz. The variation of the circulator's working frequency is 0.6 GHz. This is

achieved firstly by the change of the internal magnetization M when the dc current is less than 120 mA, then the heat in the substrate due to the winding introduces more frequency shifting. The total size ($L*W*H$) is 8mm*8mm*1.1mm.

The conventional Y-junction stripline circulator has one ferrite disk surrounded by a dielectric material. The design of the circulator presented here uses only the ferrite LTCC material. The material exposed under the magnetic bias shows the ferrite properties and the remaining shows the dielectric properties. It has been demonstrated that a passive ferrite component like circulator could be realized on the ferrite LTCC substrate without adding other materials. Therefore, this circulator could be easily integrated with other rf components such as antennas, amplifiers, filters, etc in System-on-Package (SoP).

The conventional circulator with stripline structure is designed to operate at a specific frequency. To expand the bandwidth, we usually work on the shape of the circulator's center conductor, or operate the circulator in the "edge-guided" mode. In order to increase the bandwidth, the 3D design ability of LTCC technology can be used. In this thesis, we present a new wideband circulator operating at K-band. The design is realized by stacking two circulators (gyrators) with different working frequencies into the ferrite LTCC substrate to expand the overall bandwidth. The obtained bandwidth by the simulator Ansys HFSS is 11 GHz (15.5 GHz to 26.5 GHz) which covers the K-band. The reflection and isolation are over 20 dB and the insertion loss is between 1.5 dB and 3 dB.

In this thesis, we investigate the original circulator design fully embedded in ferrite LTCC, study the performance of a ferrite LTCC circulator with integrated winding and present coplanar circulators and a wide-band circulator based on the ferrite LTCC substrate. All designs are realized in Ansys HFSS, Ansys Maxwell 3D and CST Studio at University of Saint Etienne, Laboratory Hubert Curien UMR CNRS 5516 and at

Carleton University. The fabrication is operated by VTT Technical Research Centre of Finland and the measurements are performed at Royal Military College of Canada.

Acknowledgments

I am particularly indebted to my supervisors Dr. Didier Vincent and Dr. Langis Roy for the unconditional support, valuable guidance and endless patience they generously provided during the course of this work.

I graciously thank Dr. Barry Syrett for accepting to be my co-supervisor at Carleton University for the last three months and being present at my defense.

I would like to express my special thanks of gratitude to Dr. Joey R. Bray for his guidance during this thesis and allowing me to perform the measurements in Royal Military College of Canada. His valuable feedback and enthusiasm for research made my doctoral study a very enjoyable and rich experience.

A very significant thanks to Dr. Atif Shamim at King Abdullah University of Science and Technology for his financial assistance with the fabrication of the circulators.

I am grateful to PICON Odile, JACOB Arne, AMAYA Rony, FERRARI Philippe and BAYARD Bernard, who serve on my thesis examination committee for their time and efforts. Their assistance can never be appreciated enough.

I wish to express my sincere thanks to all staff of Laboratory LT2C and the department of electronics at Carleton University, for providing me with all the necessary facilities for the research.

Finally I would also like to thank my parents YANG Chengzhang and LIU Yingxiu

and my wife LIN Zhuo, who support me to finish this thesis within the limited time.

Table of Contents

Abstract	i
Acknowledgments	iv
Table of Contents	vi
List of Tables	xi
List of Figures	xii
1 Introduction	1
2 Current state of rf ferrite devices	6
2.1 Introduction	6
2.2 Circulators	8
2.2.1 Introduction	8
2.2.2 Main characteristics of a circulator	11
2.2.3 Different types of circulator	14
2.2.4 Different conceptions of circulator	17
2.2.5 Circulators based on LTCC technology	27
2.2.6 Applications of circulators	29
2.3 Isolators	31

2.3.1	Introduction	31
2.3.2	Different conceptions of ferrite isolators	31
2.3.3	Applications of isolator	34
2.4	Ferrite switch	34
2.5	Ferrite phase shifters	35
2.5.1	Introduction	35
2.5.2	Different conceptions of ferrite phase shifters	36
2.6	Conclusion	38
3	Magnetic materials	41
3.1	Introduction	41
3.2	Classes of magnetic materials	42
3.2.1	Diamagnetism	43
3.2.2	Paramagnetism	44
3.2.3	Ferromagnetism	45
3.2.4	Antiferromagnetism	46
3.2.5	Ferrimagnetism	47
3.3	Ferrite materials	47
3.3.1	Introduction	47
3.3.2	Different types of ferrite	49
3.4	Basic properties of ferrite materials	50
3.4.1	Models of permeability tensor	50
3.4.2	Demagnetization factors	60
3.4.3	Effect of loss	61
3.4.4	Hysteresis loop	62
3.4.5	Magnetization M_s	65

3.4.6	Curie Temperature T_c	65
3.4.7	Linewidth ΔH	65
3.4.8	Effective linewidth ΔH_{eff}	65
3.4.9	Spin wave linewidth ΔH_k	66
3.4.10	Permittivity and loss tangent	67
3.5	Ferrite LTCC	68
3.5.1	Introduction	68
3.5.2	Characterization of ESL 40012	69
3.5.3	Rf behavior of saturated ferrite	75
3.5.4	Rf behavior of partially magnetized ferrite	79
3.5.5	Conventional LTCC fabrication process	81
3.5.6	Recent ferrite LTCC research works	82
3.6	Conclusion	84
4	Modeling and realizations of circulators	87
4.1	Introduction	87
4.2	CPW on ferrite LTCC	88
4.2.1	Introduction	88
4.2.2	Demagnetized ferrite $H_i = 0$	89
4.2.3	Ferrite biased transversely	89
4.2.4	Prototype of a tunable attenuator	91
4.3	Different structures of circulators	93
4.3.1	Stripline circulator	94
4.3.2	Microstrip circulator	95
4.3.3	Coplanar circulator	96
4.4	Theory of stripline junction circulators	97

4.5	Ferrite LTCC circulator with external magnet	104
4.5.1	Theory and design	104
4.5.2	Measurement	109
4.6	Ferrite LTCC circulator with integrated winding	110
4.6.1	Bias winding design	111
4.6.2	Y-junction edge-guided circulator design	116
4.6.3	Measurements	123
4.6.4	Retro Analysis	133
4.6.5	Power Capability IP3	136
4.6.6	Comparison and conclusion	139
4.7	Coplanar ferrite LTCC circulators	140
4.7.1	Introduction	140
4.7.2	Design of coplanar circulators	140
4.7.3	Measurements	141
4.8	Wideband circulator by stacking two circulators	144
4.8.1	Introduction	144
4.8.2	Theory and design	145
4.8.3	Simulation	147
4.9	Conclusion	149
5	Conclusion and perspectives	152
5.1	Conclusion	152
5.2	Perspectives	156
	List of References	158
	Publications	169

List of Tables

2.1	Comparison of main characteristics of current state of circulators . . .	16
2.2	Performance of different LTCC circulators	29
4.1	Compare of circulators realized with LTCC technology	149

List of Figures

2.1	Circulator separates the transmission and reception signals	8
2.2	Circulator consists of three ports oriented by 120°	10
2.3	Different shapes of circulator's center conductor	10
2.4	JQL Electronics: a. Coaxial circulator; b. Drop-in circulator; c. Surface Mount circulator; d. Microstrip circulator; e. High Power Waveguide circulator [1]	14
2.5	Principle construction of a phase shift circulator [2]	18
2.6	Principle construction of a Faraday rotation circulator [3]	19
2.7	Principle construction of a ring circulator: T is reciprocal T-junction and PS is non-reciprocal phase shifter [4]	21
2.8	Principle construction of a stripline junction circulator [5]	22
2.9	Standing wave pattern of a junction circulator: a. unmagnetized b. magnetized below resonance c. magnetized above resonance [2]	23
2.10	Principle construction of an edge guided circulator	24
2.11	Principle construction of a lumped element circulator [6]	25

2.12	Self-biased circulator at K_u band: (a) Cross section view of the junction resonator and quarter-wave microstrip line (b) Hysteresis loops of magnetically oriented M-type strontium hexaferrite. Perp refers to the measurement performed with the external field perpendicular to the sample surface, and par to the measurement with the field applied within the sample surface [7]	26
2.13	Non-reciprocal response based on (a) ferromagnetic media, and (b) angular-momentum-biased metamaterials. In ferromagnetic media, an external static magnetic bias (B) splits degenerate atomic states with opposite spin. Similarly, an externally applied angular-momentum vector splits counter-rotating degenerate modes of an azimuthally-symmetric ring, enabling nonreciprocity [8]	28
2.14	Circulator used as duplexer	29
2.15	Combining networks for radio links: (a) solution based on filters; (b) solution based on circulators [2]	30
2.16	Two possible configurations of resonance isolator: (a) E-plane ferrite (b) H-plane ferrite [9]	32
2.17	Geometry and electric fields of a field displacement isolator [9]	33
2.18	Diagram of an isolator by adding a matched load to one of a circulator's ports	33
2.19	Diagram of a ferrite switch based on circulator	35
2.20	Nonreciprocal Faraday rotation phase shifter [9]	36
2.21	Geometry of a latched phase shifter (a) using a ferrite toroid (b) using 2 ferrite slabs [10]	37
2.22	Reggia-Spencer phase shifter [10]	38
3.1	Atomic and magnetic behaviour of diamagnetism [11]	43

3.2	Atomic and magnetic behaviour of paramagnetism [11]	45
3.3	Atomic and magnetic behaviour of ferromagnetism [11]	46
3.4	Atomic and magnetic behaviour of antiferromagnetism [11]	47
3.5	Atomic and magnetic behaviour of ferrimagnetism [11]	48
3.6	A spinning electron: Spin magnetic dipole moment (\vec{m}) and angular momentum vectors (\vec{s}) [9]	52
3.7	Geometric relation of different elements of permeability tensor . . .	55
3.8	Demagnetization factors of some simple shapes [12]	61
3.9	An example of magnetic hysteresis loop [13]	63
3.10	Definition of the linewidth ΔH [9]	66
3.11	Definition of the effective linewidth ΔH_{eff} [14]	67
3.12	Definition of the spin wave linewidth ΔH_k [14]	68
3.13	Photo of ESL 40012 ferrite tape ('green' tape)	69
3.14	LTCC (a) solenoid transformer unit cell cross section and (b) toroid transformer tilted front view [15]	70
3.15	Measured hysteresis curves from the LTCC transformers [15]	70
3.16	B-H curve (first magnetization) used in EM simulator	71
3.17	Attenuation constant in terms of frequency	72
3.18	Major magnetization curves of the ESL 40012 sample at different sample temperatures, magnetic polarization B(T) versus magnetic field H(A/m). The maximum magnetic field was 5 kA/m for all curves.	73
3.19	The VSM (Vibrating Sample Magnetometer) measurement performed by laboratory LT2C shows that the magnetization saturation $\mu_0 M_s$ loses 50% at $100^\circ C$	74
3.20	μ' and κ' in terms of σ	76

3.21	μ'' and κ'' in terms of σ	77
3.22	μ_{eff} in terms of σ	78
3.23	κ on μ in terms of σ	79
3.24	κ and μ in terms of internal magnetization M	80
3.25	$\frac{\kappa}{\mu}$ and μ_{eff} in terms of internal magnetization M	81
3.26	Typical multilayer ceramic substrate manufacturing process [16]	82
4.1	Design of a CPW on ferrite LTCC	88
4.2	Photo of a fabricated CPW on ferrite LTCC	89
4.3	Measurement configuration of the CPW with an external electromagnet	89
4.4	Measured S-parameters when ferrite is totally demagnetized	90
4.5	Simulated S-parameters when ferrite is totally demagnetized	90
4.6a	Comparison of S21 and S12 between simulation and measurement when ferrite is biased transversely with internal magnetic field $H_i=660$ Oe	91
4.6b	Comparison of S11 and S22 between simulation and measurement when ferrite is biased transversely with internal magnetic field $H_i=660$ Oe	91
4.7	Measured resonance frequencies under different bias fields	92
4.8	Comparison of measured and calculated resonance frequencies under different bias fields	93
4.9	Prototype of a tunable attenuator with windings in series	93
4.10	Principle construction of a stripline junction circulator: (1) two metal grounds; (2,3) center conductor; (4) ferrite disk; (5) V is the coupling angle; (6) u is the height of the ferrite disk; (7) H_i is the bias field; (8) d is the thickness of conductors; (9) R radius of the center conductor [5]	94
4.11	Principle construction of a microstrip junction circulator [17]	96

4.12	Top view of the signal line and the ground plane of a hexagonal circulator with CPW structure [18]	97
4.13	Circulator coordinate reference	98
4.14	Stripline circulator configuration	105
4.15	Calculated S-parameters in Matlab	106
4.16	Parameters of an edge-guided circulator	107
4.17	Edge-guided circulator's 3D design	108
4.18	Simulated S-parameters in HFSS when port 3 is matched: a circulator working at 15 GHz	108
4.19	The measurement of the CPW verifies the calibration and demonstrates that the loss below 10 GHz is strong	109
4.20	The measurement of the circulator shows the working frequency is 15 GHz	110
4.21a	The dc winding consists of 4 coils below the circulator and 2 coils above it	111
4.21b	Hexagonal coil dimensions	112
4.21c	2D conceptual sketch of the biasing magnetic flux	113
4.22a	Magneto-static simulation of winding in ferrite LTCC with a B-H curve: \mathbf{Bi} along Z axis	113
4.22b	Magneto-static simulation of winding in ferrite LTCC with a B-H curve: \mathbf{Bi} along X axis on layer 6 (circulator inner conductor)	114
4.22c	Magneto-static simulation of winding in ferrite LTCC with a B-H curve: \mathbf{Bi} along X axis on layer 9	115
4.23	Edge-guided hexagonal circulator 3-D design for LTCC implementation	117

4.24	The simulated S-parameters in Matlab by employing Green and Sandy's partially magnetized tensor model when $\mu M=200$ mT and $R=1.79$ mm	119
4.25	The simulated S-parameters in Matlab with Green and Sandy's partially magnetized tensor model under different internal magnetization μM	120
4.26	The circulator's working frequency in terms of the internal magnetization μM	121
4.27	Transition from CPW transmission line to stripline	121
4.28a	Magnetic bias model in HFSS	122
4.28b	Simulated S-parameters in HFSS and Matlab	124
4.29	Prototypes of the ferrite LTCC circulator	125
4.30	S-parameters measurement configuration	125
4.31	CPW transmission line measurement: S-parameters	126
4.32	Measured S-parameters: Circulator without current	126
4.33	Measured S-parameters with current: S21 and S12 in terms of current	127
4.34a	Comparison of measurement and HFSS: S21 and S12	128
4.34b	Comparison of measurement and HFSS: S11 and S22	128
4.34c	Circulator with an opposite direction of 300 mA dc current: S-parameters	129
4.35	Measurement probe station photo	129
4.36a	Magneto-static simulation of the magnets in ferrite LTCC with a B-H curve: Bi along Z axis	130
4.36b	Magneto-static simulation of the magnets in ferrite LTCC with a B-H curve: Bi along X axis	130
4.37a	S-parameters with magnets: S21 and S12 in terms of current	131

4.37b	S-parameters with magnets: S11 and S22 in terms of current	131
4.37c	Isolation and transmission curves when windings with the current is biased that opposes the magnetic fields of the magnet	133
4.37d	μ_{eff} in terms of magnetization saturation $\mu_0 M_s$ with $\mu M = 0.2T$ when the ferrite is partially magnetized using the model of Green and Sandy	133
4.38a	Magnetic bias model in CST	134
4.38b	Comparison of measured and simulated S21 and S12 by CST when internal magnetization μM is 200 mT	135
4.38c	Comparison of measured and simulated S11 and S22 by CST when internal magnetization μM is 200 mT	135
4.38d	Simulated circulator's frequency variation (S11 in dB) in terms of magnetization μM	136
4.39	IP3 measurement details	137
4.40	Swept-Power IMD Test when current I=0 mA	137
4.41	Swept-Power IMD Test when current I=350 mA	138
4.42	Swept-Power IMD Test when current I=430 mA	139
4.43	Comparison of circulators realized by ferrite LTCC and conventional LTCC technology	139
4.44	Design of a coplanar circulator (top view) [17]	141
4.45	Fabricated CPW and coplanar circulators operating at different fre- quencies	142
4.46	Measured S-parameters: coplanar circulator operating at 18 GHz . .	143
4.47	Measured S-parameters: coplanar circulator operating at 22 GHz . .	143
4.48	Measured S-parameters: coplanar circulator operating at 27 GHz . .	144
4.49a	Design of a wideband circulator by stacking two circulators	145

4.49b	Ferrite LTCC layers configuration	146
4.50a	Distribution of magnetic field H_i in ferrite LTCC	147
4.50b	Internal bias field B_i in terms of Z	148
4.51	S-parameters by co-simulation in HFSS and Maxwell 3D	149

Chapter 1

Introduction

In recent years, multi-standard systems such as GSM, UMTS, LTE, 4G/5G have been employed in cellular radio handsets. In addition, a carrier aggregation (CA) service has been started and cognitive radio terminals with reconfigurable rf front-end circuit are in the developmental stage for the next-generation of communication systems. Since mobile handsets using the multi-standard systems are handling a large number of frequency bands, the rf circuits of the handsets have been becoming more and more complex with many signal paths corresponding to various frequency bands. On the other hand, the mobile data transfer rates have been enhanced and the frequency bands have been extending to higher frequencies. Therefore a miniaturized and tunable rf front-end architecture for frequency division duplexing (FDD) system is very effective for simplifying the circuit configuration [19]. In wireless radar applications, circulator seems to be the most suitable microwave device as a duplexer, because the transmission and reception signals have the same frequency, hence they cannot be separated by frequency filtering. Essentially, circulator allows duplex (bi-directional) communication when a single path is used. It avoids interaction between the receiver and the transmitter, permitting them to use a shared antenna.

In order to miniaturize rf circuits, we introduce the Low Temperature Co-fired

Ceramics (LTCC) technology. Since LTCC has a 3D design ability, therefore the size of the circuits could be greatly reduced. Furthermore, as the fired temperature is below 1000°C, LTCC could apply low loss metals (Au, Ag, Pt etc) as conductors. Consequently, compared with applications based on other materials like resin, LTCC applications have relatively low losses and high microwave performance. In addition, the thermal expansion coefficient of LTCC applications is competitive compared with resin materials and other ceramic materials. More important, LTCC could be combined with many other materials with different characteristics, therefore various types of components could be integrated and built into LTCC substrates. For these reasons, LTCC is regarded as one of the promising future technologies for the integration of components and substrates for rf applications [16]. Application of LTCC technology is now widely spread and is a good candidate for SoP (System-on-Package) system. Its presence is well established in high frequency applications [20,21], sensor applications, component packaging, chemical reactors and bio-medical applications [22].

Unfortunately, conventional LTCC technology does not work for ferrite devices which require non-reciprocal materials. Some researchers have demonstrated a hybrid approach to realize circulators by sintering traditional LTCC substrate and ferrimagnetic materials together [23–25]. This hybrid method creates an internal cavity using conventional LTCC technology where a piece of ferrimagnetic material is put in and then sintered (cofired together). The disadvantages of this approach are: 1. the ferrimagnetic material should be able to be co-fired (compatible) with the non-magnetic ceramic LTCC substrate; 2. an external magnet is necessary to generate the static magnetic bias; 3. the demagnetizing field cannot be avoided.

Meanwhile, a new technology, ferrite LTCC technology, which is originally used to design inductors, now could be used to design high frequency tunable devices with integrated winding, such as tunable antenna [26–28], tunable filter [29] and tunable

phase-shifter [30]. Ferrite LTCC substrate is a ferrite material, therefore we can embed a winding into the substrate, creating the dc magnetic bias from the inside. By using this elegant solution, we can remove the external magnets (or electromagnets) and avoid the demagnetization fields. In addition to eliminating the demagnetization effect, the required bias field strength can be further reduced by operating the ferrite in the partially magnetized state instead of saturation state [28].

Having this new technology, we present this thesis to firstly investigate original circulator design fully embedded in ferrite LTCC substrates, then study the performance of a ferrite LTCC circulator with integrated winding and finally investigate coplanar circulators and a wide-band circulator. For the ferrite LTCC circulator with integrated winding, the controllability of the cores bias field makes this prototype device multifunctional: when no bias field is present, it behaves as a power splitter; with bias, it behaves as a circulator and the direction of circulation can be switched by reversing the direction of the DC current; finally, when used with small external magnets, the DC current can be used to change the circulators working frequency. The proposed device could be used in many applications. For instance, when used between a transmitter and a pair of antennas, the circulator/splitter could be used to control the radiation pattern: it could either feed the two antennas at the same time, or power only one of them for a chosen direction or polarization. Based on this principle, a more complex feed network could also be realized by applying more than one circulator/splitter to achieve pattern and polarization diversity. Switchable circulators can also be used to control the direction of propagation through a transmitarray.

Chapter 2 is about the current state of ferrite rf devices. Firstly, the basics of circulators will be introduced, followed by the main characteristics of a circulator such as the transmission, isolation, bandwidth, power capability, etc. Then, different

types and conceptions of circulators are presented, including the phase-shift circulator, Faraday rotation circulator, ring circulator, junction circulator, the circulators realized by LTCC technology etc. The applications of circulators such as decoupling, combining and isolating are also proposed. Since ferrite isolator is an important ferrite device, various conceptions of ferrite isolators are also presented. Phase shifter, which is widely used in phased array antennas, is discussed in this chapter along with several conceptions. Finally, other ferrite devices, like ferrite switch is briefly described.

The objective of Chapter 3 is to present the magnetic materials. In general, there are diamagnetic, paramagnetic, ferromagnetic, antiferromagnetic and ferrimagnetic materials. Usually, ferrimagnetic materials, or ferrite is employed in microwave devices because of their high resistivity (not conducting), low dielectric loss and reasonable dielectric constant. We will present the characterization of ferrite materials by explaining the dielectric loss, hysteresis loop, magnetization saturation, Curie temperature, linewidth (including effective linewidth and spin wave linewidth) etc. Different permeability tensor theories for saturated, partially magnetized and demagnetized ferrite are presented. In particular, the ferrite LTCC tape ESL 40012, which is used in this thesis, is described, along with the properties under different magnetized conditions (saturated and partially magnetized). Since ferrite LTCC's fabrication process is not accessible to the authors, only the conventional LTCC process is demonstrated.

The modelization and realization of ferrite LTCC circulators is located in Chapter 4. This chapter starts by studying a CPW transmission line on the ferrite LTCC substrate. This work allows to have a first manipulation of designing rf devices on this substrate. Then we briefly introduce different structures of circulators including the stripline, microstrip and coplanar structure. The stripline structure is chosen in this thesis to realize circulators because the two metal grounds of the stripline

provide a rf shielding while allowing the magnetostatic bias field into the ferrite core. The theory of a stripline junction circulator is presented in detail with mathematical calculations in Matlab. Then, two ferrite LTCC circulators are realized: the first is a stripline circulator with external magnets. This work demonstrates, for the first time, the feasibility of a circulator on this substrate. The second is a ferrite LTCC circulator with integrated winding which magnetizes the ferrite from the inside. This circulator is multifunctional. When the winding is energized by a current, the device operates as a dynamic circulator in which the circulation direction can be changed by switching the direction of the current. Besides, the proposed device can even operate as a power splitter by removing the bias current. Then several coplanar circulators are also realized to find the maximum frequency which the substrate could support. Finally a wide band circulator by stacking two circulators with different operating frequencies is proposed and simulated.

Chapter 2

Current state of rf ferrite devices

2.1 Introduction

Microwave passive non-reciprocal devices such as circulators, switches, isolators and phase shifters use an important type of material: ferrite. Ferrites allow electromagnetic waves to penetrate and then the waves interact with the internal magnetic moments within the ferrite. Besides, ferrites are magnetic ceramic materials instead of magnetic metals which are conductors, therefore ferrites are favorable as microwave device substrates. The microwave propagation in ferrite devices is controlled by a dc magnetic field which could be static or tunable. The ferrite devices can be linear or nonlinear, and reciprocal or nonreciprocal. Nowadays, microwave systems widely use ferrite components and various types of ferrite materials are employed according to the design requirements. A number of devices have been developed across a wide range of microwave spectrum for various power levels and are now commercially available over the last 50 years. As an example, adjustable phase shifters are used in the shipboard Aegis systems and ground-based Patriot where the agile beam phased array radars and beam steering components are employed. By changing the applied dc magnetic field (hence internal magnetization), a rf within the ferrite phase shifters

could obtain different phase shifts. These devices are based on gyromagnetic effects of ferrites leading to the properties of microwave phase shift. Circulators based on ferrites are desired in radar systems to be duplexers which isolate transmitters from receivers. In addition, selective filter banks also employ circulators as switches.

Studies of microwave ferrite devices suggest that one or more of the following effects could be used to explain their behaviors [31]: ” *Faraday rotation* - the rotation of the plane of polarization of a microwave as it propagates through a ferrite in the direction of the magnetization. *ferromagnetic resonance* - the strong absorption that can occur when an elliptically polarized rf magnetic field is perpendicular to the direction of magnetization. *field displacement* - the displacement of the field distribution transverse to the direction of propagation resulting in more or less field in the ferrite region. *nonlinear effects* - at higher power levels amplification and frequency doubling are possible and subsidiary losses can occur. *spin waves* - short-wavelength waves of magnetization that can propagate at any angle with respect to the direction of magnetization. If the wavelength of such a wave is comparable to the dimensions of the ferrite sample, it is called a magnetostatic wave (MSW)” [31].

A strong understanding of the microwave circuit theory, electromagnetic theory and magnetic materials is necessary in the development of ferrite devices [32]. Although many research efforts have been taken in this area, the demands for miniaturized size, broader fractional bandwidths, higher operating frequencies, and reduced costs are still expected to meet [31] leading to many challenges to be addressed. Our knowledge about the microwave circuit theory has been advanced by the study of ferrite devices [31].

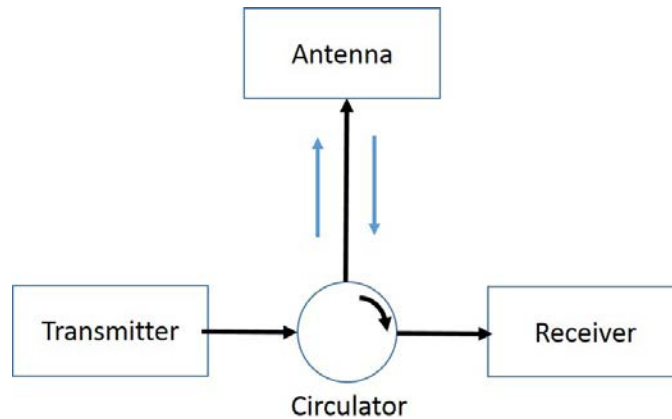


Figure 2.1: Circulator separates the transmission and reception signals

2.2 Circulators

2.2.1 Introduction

Currently most telecommunication systems operating at microwave frequencies are based on the technology of rf circuits. Passive non-reciprocal components such as phase shifters, isolators, circulators, tunable antennas are widely used in wireless telecommunication systems like radar system, cellphone base station, satellite communication system, etc. Essentially, circulators provide traffic between different signal ports in one direction and not in the other. Therefore circulators are employed in microwave applications as duplexers to separate the transmission and reception signals when only one shared antenna (and one carrier frequency) is used (see Figure 2.1). A three-port circulator can also be used as an isolator by connecting one of the circulator's ports to a matched load which absorbs the reflected energy. This sort of isolator serves to protect a source against any reflected energy, especially in microwave applications with high power.

The brief history of circulators is [33]: In the early 1950's, we saw the first commercial microwave circulator. Faraday rotation circulator was one of the most famous

circulators [34]. There were later resonance isolators [34] and differential phase shift circulators [35], which were easy to be constructed and had high power-handling capabilities. Then, field-displacement devices came into our sight [36], along with junction circulators in the early 1960's. An important moment in 1962, H. Bosma developed a theory to explain the operation of a Y-junction circulator [5, 37]. The theory employs the Green function approach to calculate the distribution of rf fields in a stripline Y-junction circulator. Later, a theory explaining the rotation of the rf standing-wave in a circulator's ferrite disk was proposed by Fay and Comstock. It describes two rotating waves under the biasing field [38]. The "continuous frequency tracking" conditions for a wide-band junction microstrip circulator were then developed by Wu and Rosenbaum [39]. Afterwards, many researchers discussed how to realize low loss and wide-band circulators [40–42]. Self-biased waveguide and microstrip circulators were then developed utilizing hexagonal ferrite by Weiss, Watson, and Dionne [43]. Recently, in 2015, the modeling and characterization of a self-biased circulator working at 41 GHz was demonstrated in [44]. In addition, circulator with SIW (Substrate Integrated Waveguide) based on nano-composite ferrite was also proposed [45]. Circulators, as passive non-reciprocal devices known for a long time are still under research to improve the performance and achieve the miniaturization.

Circulator could have different structures, like stripline, microstrip, coplanar structure etc. Taking a stripline circulator as an example, it usually consists of three access ports oriented at 120° (see Figure 2.2) [46] to each other around a center conductor. Various shapes (see Figure 2.3) are possible to be the center conductor [47]. The material that creates the non-reciprocity, often a ferrite disk, is separated by the center conductor.

The performance of the circulator shown in Figure 2.2 could be expressed by the

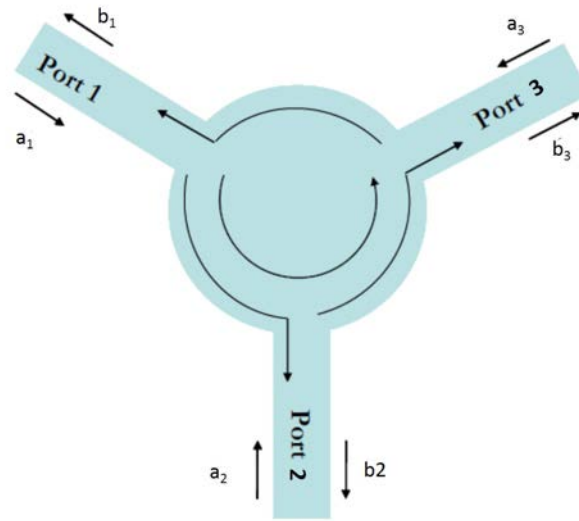


Figure 2.2: Circulator consists of three ports oriented by 120°

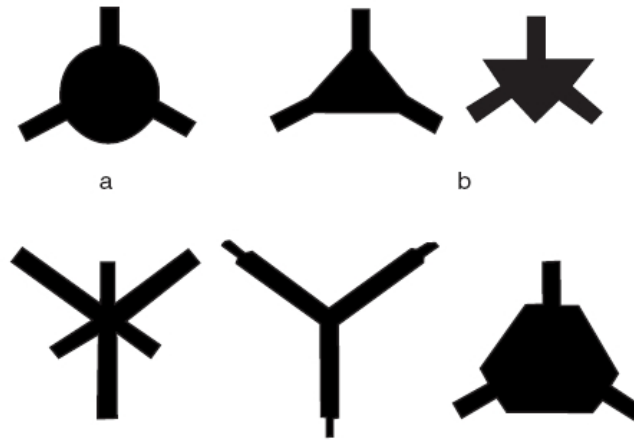


Figure 2.3: Different shapes of circulator's center conductor

matrix of S-parameters (Equation (2.1)):

$$b = S \times a \Rightarrow \begin{pmatrix} b_1 \\ b_2 \\ b_3 \end{pmatrix} = \begin{pmatrix} S_{11} & S_{12} & S_{13} \\ S_{21} & S_{22} & S_{23} \\ S_{31} & S_{32} & S_{33} \end{pmatrix} \times \begin{pmatrix} a_1 \\ a_2 \\ a_3 \end{pmatrix} \quad (2.1)$$

The parameters S_{11} , S_{22} and S_{33} are the reflection coefficients at port 1, 2 and 3, while the parameters S_{21} , S_{32} and S_{13} are the transmission parameters between the ports and correspond to the insertion loss of the device. Finally, the parameters S_{12} , S_{23} and S_{31} are the coefficients of inverse transmission and correspond to the isolation between the ports (see Figure 2.2). The signal flows in an anti-clockwise movement in this case and the signal sequence is as follows: $1 \rightarrow 2 \rightarrow 3 \rightarrow 1$. The S-parameter matrix is given, in the ideal case (without losses), by Equation (2.2):

$$S = \begin{pmatrix} 0 & 0 & 1 \\ 1 & 0 & 0 \\ 0 & 1 & 0 \end{pmatrix} \quad (2.2)$$

2.2.2 Main characteristics of a circulator

A circulator's performance is mainly characterized by the isolation, insertion loss, bandwidth, power capability, temperature and in some cases, frequency tunability.

Isolation

Circulator, as an important component in microwave applications, is required that the device has a high isolation level. Isolation measures the separation of signal levels on adjacent ports of a device. High isolation (in dB) value leads to a low interference of the signal between one port and the other. The value of isolation relates to the Voltage Standing Wave Ratio (VSWR). Taking a circulator whose port 3 is connected to a matched load as an example: if a poor match (e.g. $VSWR=2$) at port 3 is observed, the expected isolation is below 10 dB, but if a good match load is used as the termination, the VSWR match could be improved to 1.1 which

corresponds to an isolation over 20 dB. However, if impedance match changes at all the three ports, active intelligence (compensation of matching) could be employed. This remains to be explored by future work.

Insertion loss

Insertion loss is another important parameter for circulators. Generally, the insertion loss is significant at high frequencies. Accordingly, a low insertion loss is desired to avoid wasting precious power. The typical value of the insertion loss for a circulator working at X band is <0.5 dB.

Bandwidth

The bandwidth is the frequency range where it ensures a value of desired reflection, isolation and insertion loss. The fractional bandwidth is commonly used which is the bandwidth of a device divided by the center operating frequency. Commercialized circulators usually have a fractional bandwidth over 3% of the working frequency. Some circulators could even cover one or several bands such as the band X, Ku, K, Ka, etc.

Power capability

The power capability is an issue of the linearity of circulators. Circulators are considered to be linear devices and usually work under P1 dB compression point or IP3 point. High power is usually necessary for radar systems where high energy radars/antennas are used. The power capability varies according to different manufactures and applications, typically 2 - 250 Watts. More power can be achieved at the expense of device's size and cooling systems. As an example, a single junction

isolator (based on a circulator) with an internal 10 W load capability could be manufactured by MECA Electronics [48]. However, for safe heat transfer and derating, the recommended maximum power that the device could operate with is 2 W. Meanwhile, arming an external load would make heat transfer to an external heat sink, consequently higher isolator power level could be achieved easily at the cost of the size.

Temperature

The saturation magnetization M_s of ferrite material is a strong function of temperature, decreasing as temperature increases. This effect can be understood by noting that the vibrational energy of an atom increases with temperature, making it more difficult to align all the magnetic dipoles [9]. At a high enough temperature (threshold), the thermal energy is greater than the energy supplied by the internal magnetic field, and a zero net magnetization results. This temperature is called the Curie temperature, T_C [9, 49]. The typical maximum operating temperature is $75^\circ C$ according to JQL Electronics Inc [1].

Frequency tunability

Circulator's frequency tunability is usually achieved by changing the static external magnetic bias field provided by a bulky electromagnet. Conventional circulators work under saturated state, so the external magnet need to overcome the demagnetization field. In order to increase the internal magnetic field by 0.1 T, extra 80 KA/m magnetic H field is required, leading to the difficulty of designing a compact tunable device. Recently, researchers have demonstrated that an integrated winding in ferrite LTCC ESL 40012 could easily change the internal magnetic field from 0 to 0.4 T using a H field less than 2.5 KA/m under partially magnetized state [15]. This idea

could be used to design compact tunable devices [26–30]..

2.2.3 Different types of circulator

Commercialized circulators could be classified into different categories according to their connections (see Figure 2.4 [1]):

- Coaxial circulator
- Drop-in circulator
- Surface-mount circulator
- Microstrip circulator
- Waveguide circulator

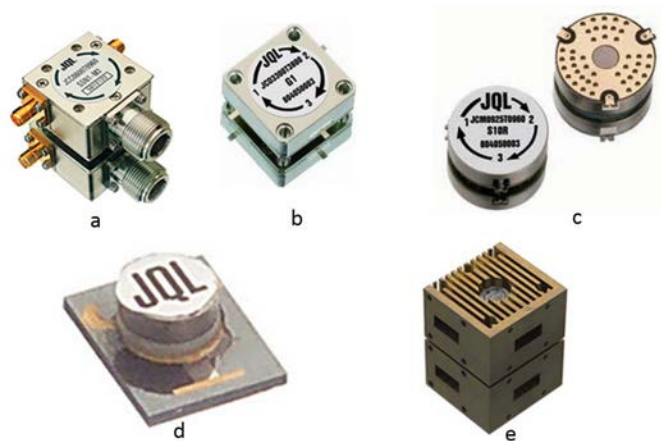


Figure 2.4: JQL Electronics: a. Coaxial circulator; b. Drop-in circulator; c. Surface Mount circulator; d. Microstrip circulator; e. High Power Waveguide circulator [1]

Typically these circulators have a broad selection of frequencies and bandwidths. They are designed for military, spatial and commercial applications. The power

capability generally ranges from several single watts to mega-watts with isolation above 18 dB per junction and low insertion loss (below 0.5 dB). They often have SMA or N connectors.

Table 2.1 shows the main performance of current commercialized circulators at X band. High power circulators are usually realized with waveguides and they can be easily found in military radar system who requires high radiation power. However, high power handling circulators come with large sizes. Compact circulators like surface-mount circulators are miniaturized at the expense of power capability.

Table 2.1: Comparison of main characteristics of current state of circulators

F(GHz)	ISO (dB)	INS Loss (dB)	Power (W)	Type	Size (mm)	Manufacture	Reference
8-12	18	0.6	10	Coaxial	15*19*13	JQL Electronics Inc	JCC8000T12K0S1
9.5-10.5	20	0.4	10	Drop-in	8.9*12.5*7.8	JQL Electronics Inc	JCD9500T10K5G1
9.5-10	20	0.4	5	Surface-mount	6.35 ϕ	JQL Electronics Inc	JCM9500T10K0G0
9-10	20	0.5	5	Microstrip	7.5*6*3.5	JQL Electronics Inc	JCS9000T10K0
9.4-9.8	40	0.4	150	Waveguide	36*90*33	JQL Electronics Inc	JCWR90-36-HP
8-12.4	20	0.4	2	Coaxial	unknown	MECA Electronics, Inc.	CS-10.200
8.2-12.4	20	0.4	250	Waveguide	41*57*60	rf Lambda	RFWC90C
7-12.4	18	0.5	10	Coaxial	32*9.91*24.13	PE PASTERNAK	PE8403
8.2-12.5	21	0.2	10-1K	Waveguide	unknown	ETG Canada	WR90

2.2.4 Different conceptions of circulator

Circulators can be realized using different conceptions which are briefly described below [2]:

- Phase shift circulator
- Circulator based on Faraday rotation
- Ring circulator
- Junction circulator
- Edge-guided mode circulator
- Lumped-element circulator
- Self-biased circulator
- Magnetic-free circulator

Phase shift circulator

Phase shift circulators are commonly applied in high power (up to Mega-Watt) radar systems [35] [50]. As an example, the conventional 4-port differential phase shift circulator is based on a rectangular waveguide, where thin ferrite slabs are loaded and transversely-magnetized (see Figure 2.5) [2].

Differential phase shift circulator is nonreciprocal and based on a differential phase shift of 90° between a magic T (whose output signals have an equal phase) and a 3-dB coupler (whose output signals have a 90° phase difference) in the device. A wave goes into port 1, then the magic T splits the wave into two waves which have equal

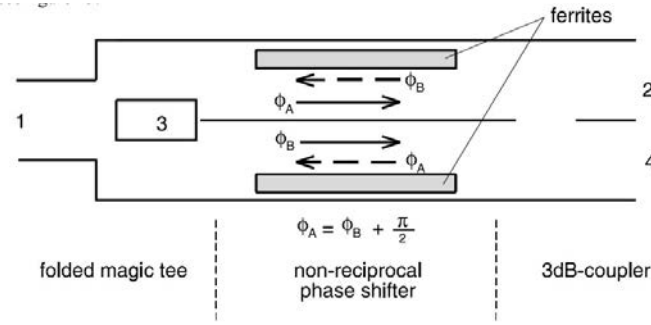


Figure 2.5: Principle construction of a phase shift circulator [2]

energy and phase. After that, the two waves enter the phase shifter which is non-reciprocal. The first wave is shifted by Φ_A , and the second wave by Φ_B , where there is a difference of 90° between Φ_A and Φ_B . In the 3 dB-hybrid, the two waves are split a second time and each wave has two equal parts, but this time, the 3-dB hybrid leads a 90° delay between two outputs. Therefore the waves cancel each other at port 4 while add each other at port 2. Similarly, a wave entering port 2 will be transmitted into port 3 and port 1 is isolated.

The geometry, magnetic losses, bias field magnetization, low power losses and high material temperature-stability (Curie temperature) performance should be considered when we design a high power phase shift circulator. The parameters of ferrite slabs, such as the thickness and length along with the permanent magnetic field are crucial to have a 90° phase shift [50]. Phase shift circulators are bulky, especially those for high continuous wave (CW) power applications.

Circulator based on Faraday rotation

The theory and design of a circulator employing a Faraday rotator is firstly discussed in [34]. These circulators rely on the Faraday rotation effect which is considered to be non-reciprocal [3, 51].

The diagram of a conventional four-port Faraday rotation circulator is shown

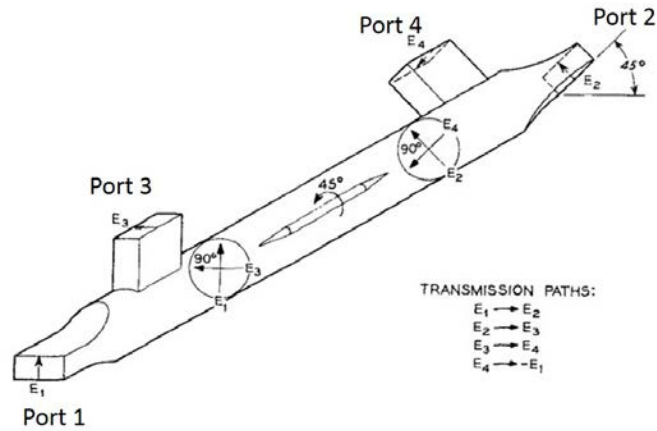


Figure 2.6: Principle construction of a Faraday rotation circulator [3]

in Figure 2.6 [3]. There are two transitions between the rectangular and circular waveguide at the two nodes of the circulator. A TE_{10} wave is injected into the left port of the rectangular waveguide, then the first transition guides the wave into a round waveguide, meanwhile the mode becomes a linearly polarized TE_{11} wave. A round ferrite rod is placed at the center of the waveguide and magnetized in the direction of the waveguide. Two circular rotating waves then obtained: one rotating clockwise, the other anti-clockwise when we look in the direction of propagation. The electron spins in the ferrite rod then interact with these two waves. One wave has the propagation speed μ_+ and the other has the μ_- . If the two rotating waves are combined after they have traveled some distance, a linear TE_{10} -wave is formed a second time with some rotating degrees. With careful calculation of the biased magnetic field and the length of ferrite rod, a rotation of 45° could be expected. Finally, the round waveguide is transformed into the rectangular waveguide via the second transition and forms the final output of the circulator (see Figure 2.6). Therefore all the input energy passes through exclusively from port 1 to port 2. In a like manner energy entering port 2 passes exclusively to port 3, energy entering port 3 passes exclusively to port 4, and

energy entering port 4 passes exclusively to port 1.

Circulators based on Faraday rotation are usually built as isolators. There are only two ports: one input and one output. Resistive sheets are employed at the other ports in order to absorb the waves, hence avoiding reflected energy. Faraday rotation isolators could work at high frequencies [52] and nowadays as optical isolators of fibre cables [53].

Ring circulator

Ring circulator is barely used in practice and mainly studied in theory [2]. A rigorous theoretical analysis of the ring circulator concept based on a network model is discussed in [54] by Weiss. A conventional three-port ring circulator is shown in Figure 2.7 [4]. The design is symmetrical and it is composed of three reciprocal T junctions and three nonreciprocal phase shifters. In theory, by choosing appropriate phase shifts, such junctions could be assembled to be a perfect circulator. Accordingly, only a small amount of nonreciprocal phase shift and internal wave amplitude are required.

A wave goes into port 1 and then is split into two waves: one follows clockwise and the other anticlockwise. The nonreciprocal phase shifters then delay the two waves. The phase shifts are carefully chosen so that they cancel each other at port 3 and add up at port 2 forming a circulation. Ring circulators present competitive mechanical characteristics (weight and size), insertion loss and bandwidth. They are possibly employed in some unique applications with high-speed switching, special power capability, etc [4, 55, 56].

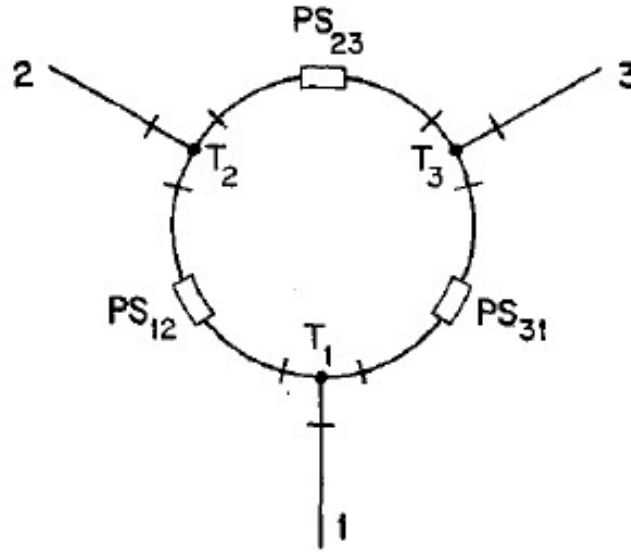


Figure 2.7: Principle construction of a ring circulator: T is reciprocal T-junction and PS is non-reciprocal phase shifter [4]

Junction circulator

The theoretical approach to the three-port symmetrical circulator is presented in [57] for the most general waveguide case. The stripline Y-junction circulator has a simple geometrical arrangement which makes it fairly easy to be studied. This is a symmetrical structure, as shown in Figure 2.8 [5], where a ferrite disk is separated by the center conductor and the three access lines are spaced by 120° . Two metal ground planes then envelop the structure. The space between the two metal grounds surrounding the ferrite disk is occupied by dielectric materials. The ferrite material is magnetized perpendicularly to the plane of the disk by a static magnetic field created by two magnets located on both sides of the structure.

The idea of a Y-junction circulator with three ports was envisaged by Carlin (1954) [58] on the theoretical basis of the processing of the S-parameters matrix of a junction with three ports. However, the current form of Y-junction circulator

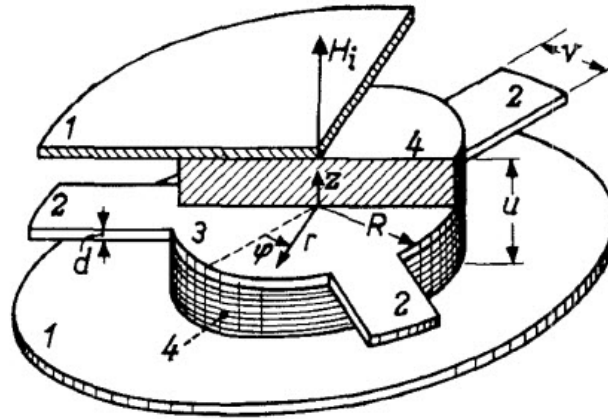


Figure 2.8: Principle construction of a stripline junction circulator [5]

and the analysis of three-port junction containing ferrites were performed by Bosma (1962) [5,37] who gives general design equations for the approximate radius of ferrite, width of stripline, operating frequency etc. Then Fay and Comstock [38] explained the operation of the rf field pattern within a circular ferrite disk (see Figure 2.9) [2]: When the biasing magnetic field is not applied, a wave goes into port 1 and then is split into two waves: one follows clockwise and the other anticlockwise possessing the same propagation speed. A standing wave pattern is hence formed in the device, leading to the coupling to port 2 and port 3. The device is therefore a power divider where half of the power goes into port 2, the other half port 3 (see Figure 2.9 a); When a biasing magnetic field is applied perpendicularly to the ferrite material, the interaction with the electron spin in the ferrite creates the propagation speed difference between the two rotating waves. The clockwise rotating wave possesses the propagation velocity γ_+ , while the anti-clockwise rotating wave γ_- . Consequently, the rotation of the standing wave pattern is observed. The angle of rotation could be adjusted by the applied dc magnetic field. Specially, if the angle of anti-clock rotation is 30° , a circulator is obtained (see Figure 2.9 b): port 3 is decoupled and the wave traverses from port 1 to port 2. Besides, if a higher biasing magnetic field is used, there is also

another circulator's operation: the standing wave pattern is rotated towards clockwise by 30° , leading to the decoupling of port 2 and all energy passes from port 1 to port 3 (see Figure 2.9 c).

The first mode is called low H_i (internal magnetic field) mode because the external static dc magnetic field is lower than the ferrite's resonance frequency. On the contrary, the second mode is called high H_i for higher static magnetic field.

Triplate junction circulators could be designed as high H_i circulators for the frequency range from 0.15 GHz to about 2 GHz to achieve potential low losses (small μ'') or as low H_i circulators for the frequency range from 1.5 GHz up to 40 GHz [2].

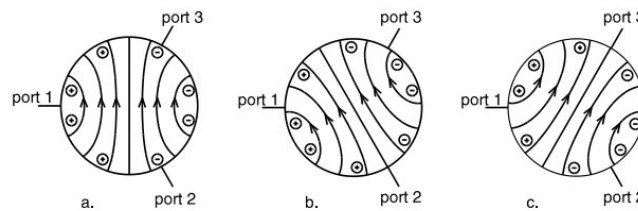


Figure 2.9: Standing wave pattern of a junction circulator: a. unmagnetized b. magnetized below resonance c. magnetized above resonance [2]

Edge-guided mode circulator

A complete study on edge guided circulators (EGC) is presented by De Santis and F. Pucci in 1975 [59]. The fundamental physical principles of edge guided wave (EGW) which underlie the EGC's operations are established in [59, 60]. Edge-guided circulators are exploited to construct broad-band circulators. In addition, broad-band isolators (up to one octave) could also be realized using edge-guided effect [61].

This effect of edge guided wave is manifested by a suitably magnetized wide strip of a microstrip or stripline gyromagnetic line. Conventionally, in triplate or microstrip lines, the distribution of rf currents is on two edges of the center conductor. When a

ferrite material is applied and biased perpendicularly to the line, the rf current leans against one edge of the inner conductor only for one propagation direction and on the other edge for the opposite direction. One of the most attractive characteristics of EGW is that it is extremely broad band [62].

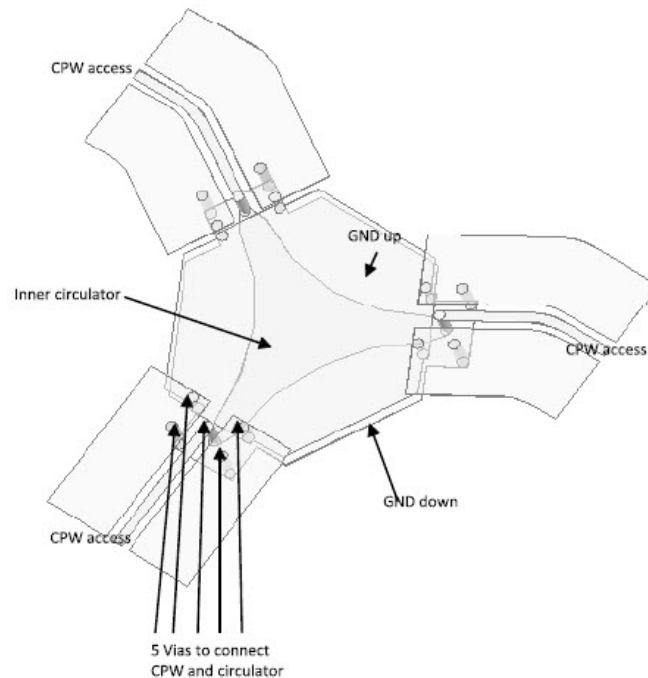


Figure 2.10: Principle construction of an edge guided circulator

Figure 2.10 shows an edge-guided mode circulator designed in this thesis. The center conductor has three smooth curves and the ferrite substrate is strongly magnetized perpendicular to the plane of the circulator. The input fields then focus on one edge of the center conductor and leave at the next port, making the third port isolated.

Lumped element circulator

The circulators described before give a bulky construction when the operating frequency is low (MHz). This is the reason why lumped element circulators are introduced [63]. The basic idea of a lumped-element circulator from the crossover ferrite circulator for VHF (Very High Frequency) and UHF (Ultra High Frequency) applications was established by Konishi in 1965 [64]. A mesh mechanism instead of an ordinary Y-stripline center conductor was proposed. The core of this circulator is a non-reciprocal ferrite crossover network junction. Figure 2.11 shows the principle design of such a junction: three conductors cross over each other and oriented by an angle of 120° . They are all connected to the same outer conductors at the other end. The inner conductors are isolated from each other. Two ferrite disks are deposited between the inner and outer conductors and magnetized by an external dc magnetic field [64, 65].

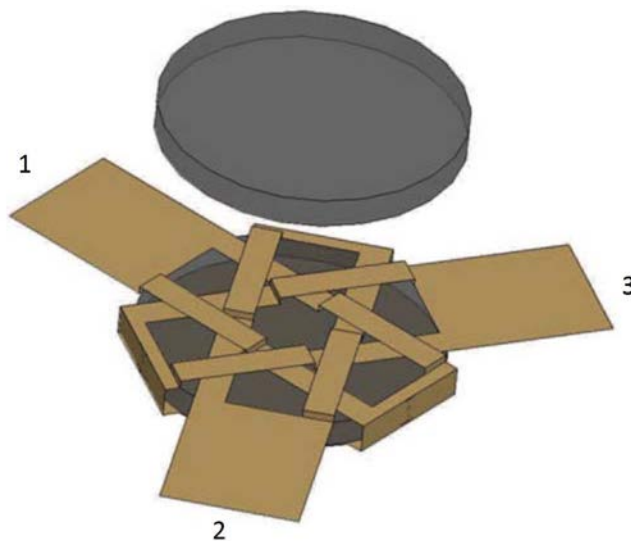


Figure 2.11: Principle construction of a lumped element circulator [6]

Since lumped-element circulator works for low frequencies and external lumped

elements could be used for tuning, they could be used in tunable cellphone applications. Recently, a reconfigurable miniaturized circulator used in mobile handsets was proposed [66]. The tunable band is from 1.71 GHz to 2.17 GHz, along with a small size ($L*W*H$) 1.2mm x 1.0mm x 0.5mm. Their port impedances are arranged by matching circuits using varactors. Besides, two supplementary varactors are also used as compensation elements for the enlargement of the frequency bandwidth.

Self-biased circulator

Ferrite used for a millimeter-frequency circulator is required to have a large magnetization saturation and low dielectric and magnetic losses [67]. The circulators presented before need huge external magnet to bias the ferrite for millimeter applications over 30 GHz [43]. However the large uniaxial anisotropy fields present in hexaferrites could be used to provide ferrimagnetic self-resonant frequencies above 40 GHz in oriented materials when they are self-biased, i.e., behave as permanent magnets. This material property could be used to get rid of the external magnets, greatly reducing the overall circulator size [33, 43, 67, 68].

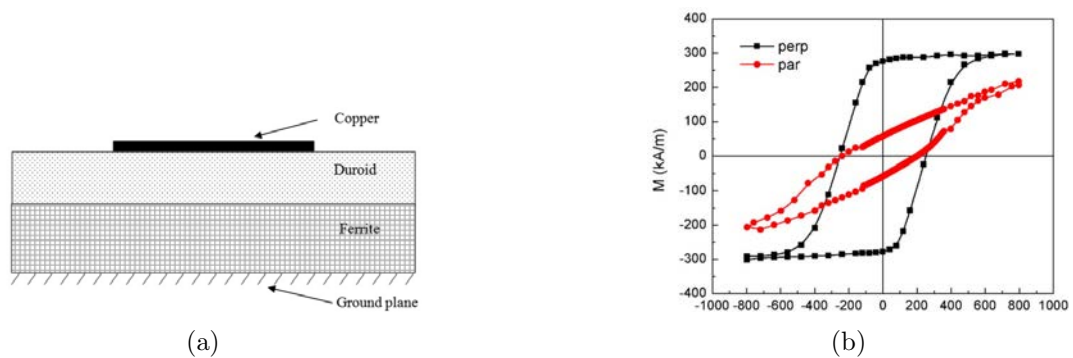


Figure 2.12: Self-biased circulator at K_u band: (a) Cross section view of the junction resonator and quarter-wave microstrip line (b) Hysteresis loops of magnetically oriented M-type strontium hexaferrite. Perp refers to the measurement performed with the external field perpendicular to the sample surface, and par to the measurement with the field applied within the sample surface [7]

Self-biased circulator designs are mainly based on the self-biased magnetic materials. The conception of this circulator which uses the microstrip structure is shown in Figure 2.12(a) and the hysteresis loops of magnetically oriented M-type strontium hexaferrite are shown in 2.12(b). Self-biased circulators usually work at high frequencies because of the high internal anisotropy field. The circulator presented in [44] has demonstrated a circulation at 41.4 GHz. However, recently a self-biased circulator working at Ku band is presented in [7] which demonstrates that the self-biased circulator can also operate below 30 GHz.

Magnetic-free circulator

A different approach to realize nonreciprocal microwave components and materials, based on biasing meta-molecules with the angular-momentum vector, has been presented in [8]. This method, theoretically introduced in [69], uses azimuthal spatiotemporal modulation to generate an effective biasing angular momentum vector, which can break time-reversal symmetry in a way analogous to magnetic bias, and can subsequently induce nonreciprocity, as envisioned in Figure 2.13. By using appropriate spatiotemporal modulation of a magnetic-free distributed-element resonating ring, an isolation over 47 dB is achieved while size is small [8]. However, the insertion loss is about 22 dB which is not competitive for a circulator working at 170 MHz.

2.2.5 Circulators based on LTCC technology

As we said before, LTCC technology is now widely spread. However, conventional LTCC tape is non-magnetic ceramic material, while non-reciprocal devices, like circulators, require magnetic material such as ferrite. In order to realize circulators on LTCC technology, researcher have developed a hybrid approach by cofiring ferrites

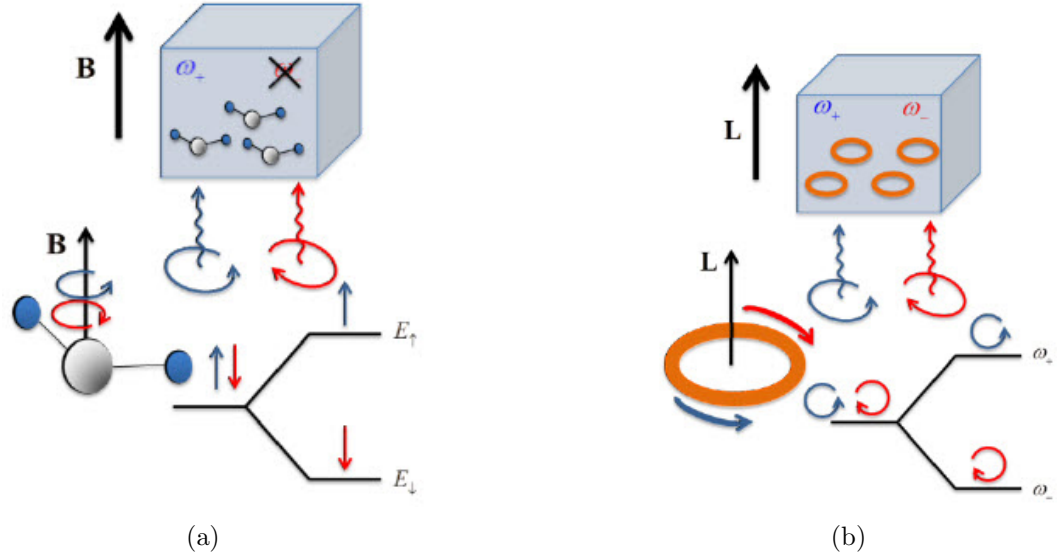


Figure 2.13: Non-reciprocal response based on (a) ferromagnetic media, and (b) angular-momentum-biased metamaterials. In ferromagnetic media, an external static magnetic bias (B) splits degenerate atomic states with opposite spin. Similarly, an externally applied angular-momentum vector splits counter-rotating degenerate modes of an azimuthally-symmetric ring, enabling nonreciprocity [8]

with non-magnetic ceramic LTCC tapes, as discussed in [23–25]. The main idea of these designs is to integrate ferrites into the conventional LTCC fabrication process to build circulators. The challenge in this development of LTCC circulators is the cofiring of laminated tapes that have different material compositions and subsequently different shrinkage rates, leading to defects, such as cracks and warpage in the fired module if care is not taken. Table 2.2 shows the performance of different LTCC circulators to date by cofiring ferrite and LTCC tape. However, the disadvantages of this approach are: 1. the ferrimagnetic material should be able to be co-fired with conventional LTCC substrate; 2. an external magnet is still necessary to generate the static magnetic bias; 3. the demagnetizing field cannot be avoided. In this thesis, we realize a circulator based on ferrite LTCC with integrated winding which magnetizes the ferrite from the inside. Therefore the external magnet is removed and we avoid the demagnetizing field [27, 30]. Furthermore, the controllability of the bias

Table 2.2: Performance of different LTCC circulators

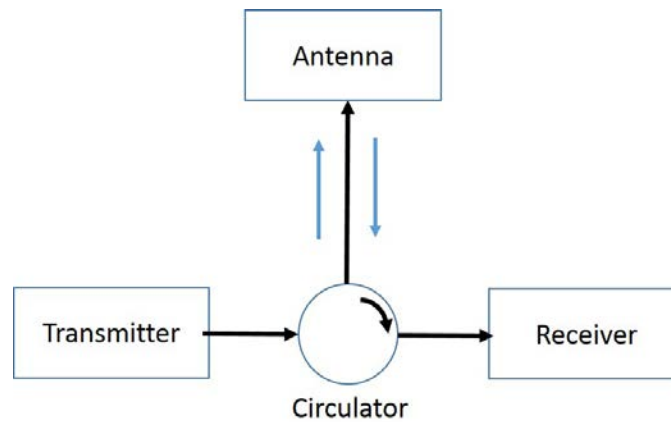
F(GHz)	ISO (dB)	INS(dB)	P(dBm)	Type	Size (mm)	Reference
7.4	25	1.7	N/A	Microstrip	N/A	T. Jensen [24]
15-17	20	0.8	N/A	Microstrip	7.5*6	Jianhua Ji [23]
5.4	23	0.5	45	Microstrip	N/A	R. Van Dijk [25]
11.8-13.2	22	1.25	42.8	Microstrip	N/A	R. Van Dijk [25]

field makes the circulator multifunctional. We will present a study on this circulator with integrated winding in Chapter 4.

2.2.6 Applications of circulators

Duplexer

The most common application of a circulator is to separate Tx and Rx signals as shown in Figure 2.14. If one transmitter and one receiver are connected to a shared antenna, two high-performance (sharp) and expensive filters are required to avoid their interaction [2, 70, 71], however, by employing a circulator for branching (duplexing), we only need an inexpensive filter at the receiver's input [2].

**Figure 2.14:** Circulator used as duplexer

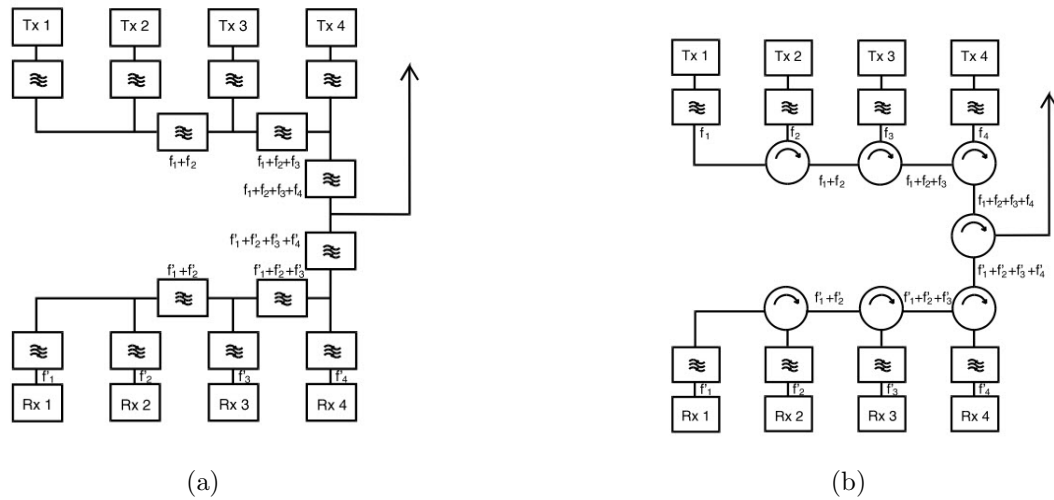


Figure 2.15: Combining networks for radio links: (a) solution based on filters; (b) solution based on circulators [2]

Combiner

Circulator can also be used as a combiner for more than one transmitter, for example, radio links. The combining of radio links turns to be challenging when the frequency is higher than 2 GHz [2]. As an example, for a station with four transmitters and four receivers (see Figure 2.15(a)), a matrix of sharp filters are used to form the combiner. The loss of each filter leads to a relatively high total loss, especially for transmitter 1 and receiver 1. In addition, the filters are not independent from each other, so that tuning one filter affects the others which makes it a difficult task. If some of the filters are replaced by circulators (see Figure 2.15(b)), the losses could be reduced and we can improve the independence between filters when tuning is performed [2]. However, this solution of circulator combining have stringent requirements for intermodulation.

2.3 Isolators

2.3.1 Introduction

Isolator is one of the important ferrite devices. A rf isolator can be considered as a diode for rf energy, allowing signal to go through in one direction only. Isolator is a two-port device and the S-parameters for an ideal isolator have the form shown by Equation (2.3). When two ports are matched, the transmission is allowed only in the direction from port 1 to port 2 and blocked in the reverse direction. The isolator must be lossy because the matrix of S-parameters is not unitary. Besides, isolators are nonreciprocal components, so that the [S] is not symmetrical [9].

$$[S] = \begin{bmatrix} 0 & 0 \\ 1 & 0 \end{bmatrix} \quad (2.3)$$

2.3.2 Different conceptions of ferrite isolators

Resonance isolators

A strong interaction with the ferrite material is expected when a circular polarized plane wave rotates in the same direction as the precessing moment of magnetic dipoles in a ferrite medium. However, a circularly polarized wave rotating in the opposite direction will have a weak interaction. This effect could be used to design isolators when the rf signal is near the gyromagnetic resonance of the ferrite.

In order to design a resonance isolator, Figures 2.16(a) and 2.16(b) show two possible configurations (E-plane and H-plane) of ferrite slab in a waveguide [9]. E-plane configuration is easy to be biased without the demagnetizing field. However the magnetic fields don't have a real circular polarization and the heat transfer from

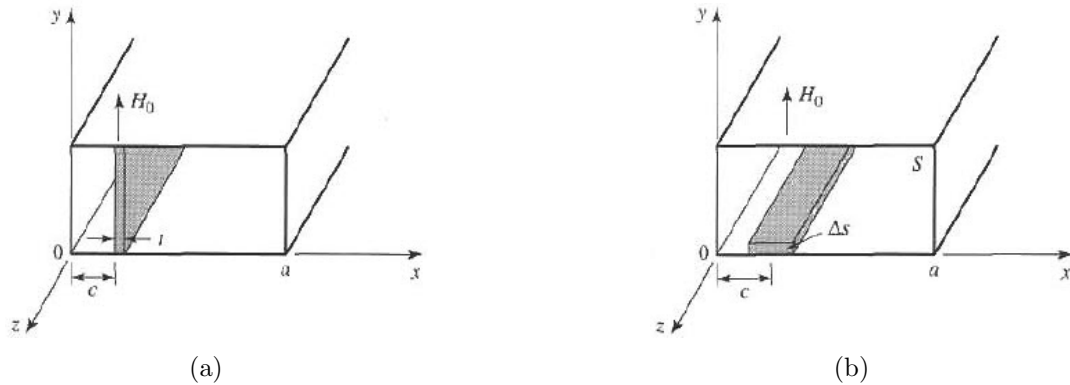


Figure 2.16: Two possible configurations of resonance isolator: (a) E-plane ferrite (b) H-plane ferrite [9]

the slab is poor. H-plane configuration allows a real circular polarization and better thermal properties, but it requires more bias field to overcome the demagnetizing field [9]. The main disadvantage of the resonance isolators is that the bandwidth is narrow.

Field displacement isolator

To improve the bandwidth and reduce the bias field, field displacement isolator could be used. There is quiet a difference of electric field distributions between the forward and reverse waves in a ferrite slab-loaded waveguide. Figure 2.17 shows that it is possible to make the electric field of the forward wave vanish, while the electric field of the reverse wave is made to be maximum at this same point (point $x=c+t$). The reverse wave will be attenuated by a thin resistive sheet which is placed in this position. Meanwhile, the forward wave can go through without being affected ($c+t < x < a$) [9]. The fractional bandwidth of field displacement isolators could be on the order of 10%. In addition, a small bias field is needed because it works below the resonance point.

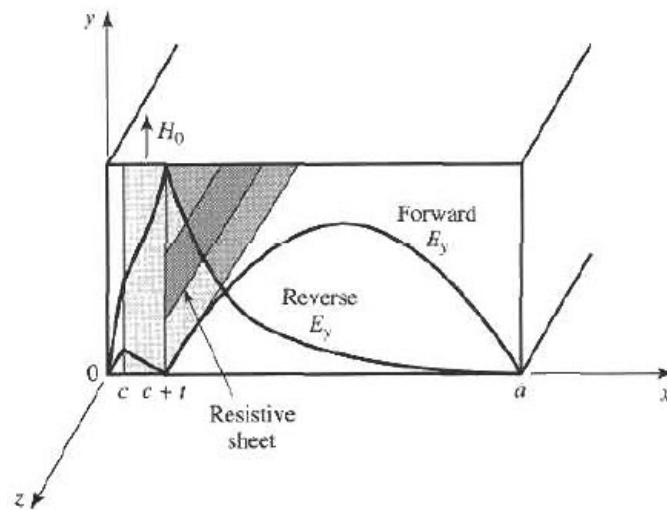


Figure 2.17: Geometry and electric fields of a field displacement isolator [9]

Using a circulator

As mentioned before, by adding a matched resistive load to one of a circulator's ports, a two-port isolator could be obtained (see Figure 2.18). If the circulator works under the resonance point, small bias field is sufficient to make this device work. Moreover, thermal transfer could also be improved because the power is absorbed externally [72].

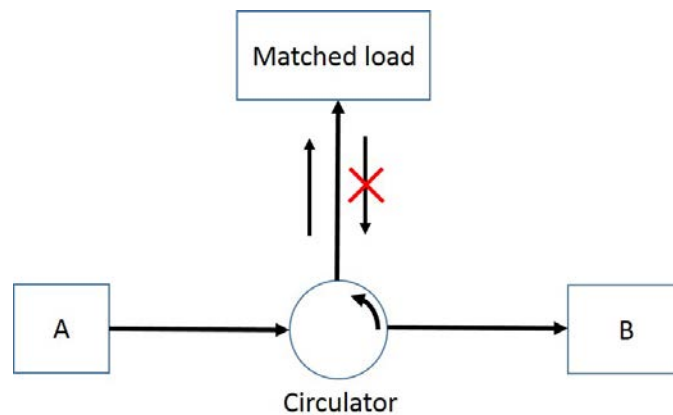


Figure 2.18: Diagram of an isolator by adding a matched load to one of a circulator's ports

2.3.3 Applications of isolator

Isolators are mainly used for decoupling. The problem that power reflecting back to generators may lead to nonlinear effects such as the instability and frequency shifting [73]. To avoid this, an isolator between the generator and the load could be applied in order to attenuate only the reflected wave and hence protect the generator [2].

Besides, in applications where cascade amplifiers are used, the change of one stage's input impedance could affect others [73]. The stability is crucial for narrow band devices because high precision of input impedance is required. The solution is to use isolators between different amplifier stages, then they can be adjusted without interacting with the others. If one stage is unbalanced, the others will also be protected and not be overloaded. Besides, we can extend greatly the interval of re-tuning power transmitters by this way. As an example, tubes (IOT's) as final amplifiers isolators is commonly recommended between the driver stages and inductive output for decoupling purpose [2].

Fading due to obstacles, for example, snow accumulation on the reflector of an antenna is a challenging problem in satellite communication in northern countries such as Finland [74]. Hence the transmitter is affected by impedance variations of the antenna. This can be avoided by employing an isolator between transmitter and the antenna.

2.4 Ferrite switch

Essentially, ferrite switch is a derivation of a three-port ferrite circulator (see Figure 2.19). In theory, wires thread a toroidal ferrite resonator, therefore, the direction of circulator's circulation could be controlled by energizing the wires with current pulses. The insertion loss is expected to be 0.15 dB per latching junction circulator,

along with 20 dB return loss and isolation. The fractional bandwidth is usually over 5% to 10%. A holding current is not required, since the switch is a latched device [75].

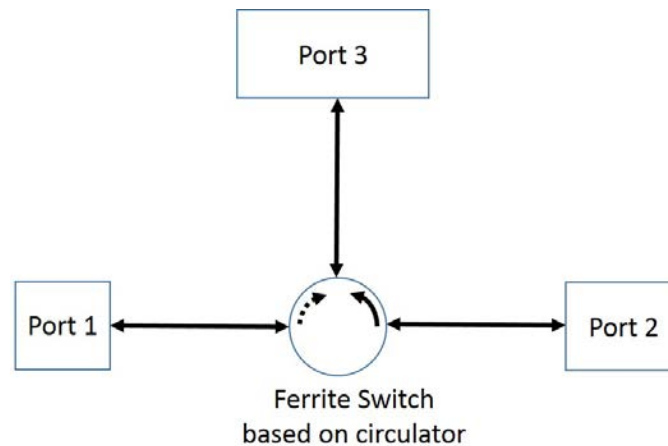


Figure 2.19: Diagram of a ferrite switch based on circulator

2.5 Ferrite phase shifters

2.5.1 Introduction

Phase shifter is among the most important applications based on ferrite materials. Basically, the ferrite phase shifter is a two-port device which provides different phase shifts by adjusting the external dc bias field applied to the ferrite. Currently, various types of phase shifters are available, either reciprocal (same phase shift in both directions) or nonreciprocal. They are in demand in phased array antenna systems where the steering-beam antennas are employed [9].

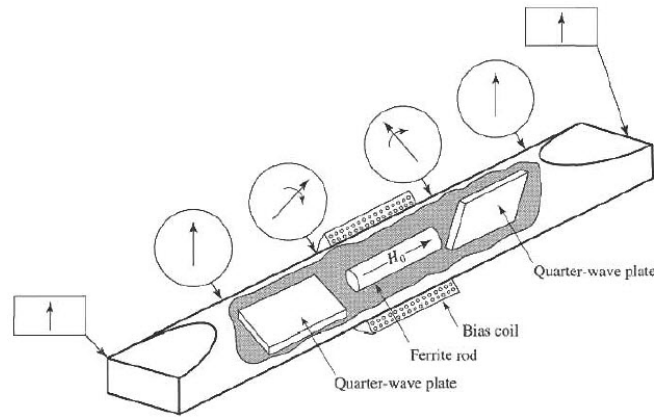


Figure 2.20: Nonreciprocal Faraday rotation phase shifter [9]

2.5.2 Different conceptions of ferrite phase shifters

Nonreciprocal/reciprocal Faraday rotation phase shifter

Circulators based on non-reciprocal Faraday rotation effect have already presented before. In fact, Faraday rotation could also be applied to design phase shifters as illustrated in Figure 2.20 [9]. A linearly polarized wave entering the input port is converted to RHCP (right hand circular polarization) wave by the first $\lambda/4$ plate, then in the ferrite region, the phase is delayed by β_+z , which can be adjusted by the bias field H_0 . Finally the second $\lambda/4$ plate converts RHCP wave back to a linear polarization. Similarly, a wave entering at the right, expects now a phase delay of β_-z because of the non-reciprocity. The modes of wave propagation are: linear $TE_{10} \rightarrow$ circular $TE_{11} \rightarrow$ linear TE_{10} . However, if nonreciprocal quarter-wave plates are used, this phase shifter could be made reciprocal, because the linearly polarized wave is converted to the same sense of circular polarization for either propagation direction [9].

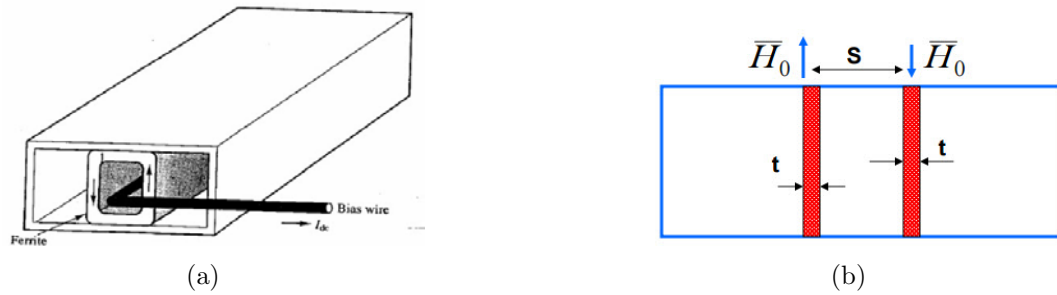


Figure 2.21: Geometry of a latched phase shifter (a) using a ferrite toroid (b) using 2 ferrite slabs [10]

Nonreciprocal latching phase shifter

When a ferrite toroid or two ferrite slabs are used in the waveguide as shown in Figure 2.21 [10], a latched phase shifter could also be realized. We magnetize the ferrite by a bias wire passing through the center of the ferrite. The rf signal is affected by the two sidewalls of toroid or the two ferrite slabs. The magnetic hysteresis of the ferrite is employed to create a phase shift which can be switched between two digital values. In practice, sections of ferrites have independent bias wires and lengths (cascade) leading to binary differential phase shifts of 45° , 90° , 180° etc.

Reggia-spencer reciprocal phase shifter

In order to get the beam position for both transmission and reception, as required in scanning antenna phased arrays used in radar or communication systems, reciprocal phase shifters are desired. The commonly used reciprocal phase shifter is the reggia-spencer phase shifter as shown in Figure 2.22 [10]. The phase shifter usually uses rectangular or circulator waveguides. We place a ferrite rod in the waveguide and magnetize it longitudinally. The electromagnetic fields are bound to the ferrite forming a circular polarized wave under the condition that the diameter of the ferrite rod exceed a threshold value. Only a relative short length is needed to obtain a large

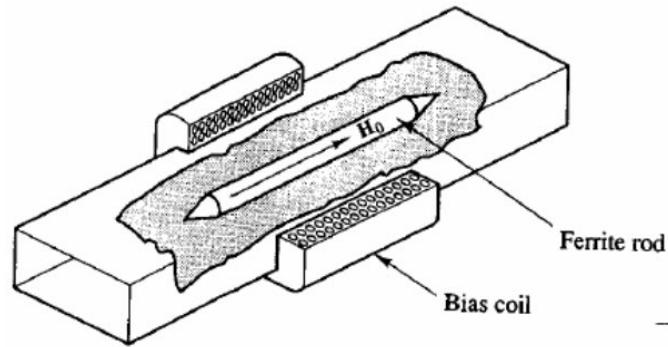


Figure 2.22: Reggia-Spencer phase shifter [10]

reciprocal phase shift. However, the phase shift is very sensitive to the operating frequency. The phase delay through the waveguide is proportional to the dc current through the coil, but independent of the direction of the propagation through the guide [9].

2.6 Conclusion

In this chapter, brief theories of microwave ferrite devices such as circulators, isolators, switches and phase shifters have been presented.

Circulators are mainly characterized by the insertion loss in the transmission direction, and the isolation in the opposite direction (blocking). The insertion loss should be as weak as possible (< 1 dB) to avoid wasting energy, while the isolation is expected to be high (> 20 dB) to reduce the interface between adjacent ports. Bandwidth of circulators could be chosen according to requirements. The typically fractional bandwidth is 10%, or a specific range of frequency, like X band which is required in radar systems. Power capability is another important character which signifies the linearity of circulators. As is known, the temperature rise in the ferrite leads to the decreasing of the magnetization saturation M_s , which degrades the

performance. The power capability varies from several single watts to mega-watts. Moreover, the circulator's frequency could be tuned by changing external magneto-static field. Comparison of different types of circulators between coaxial, drop-in, surface mount, microstrip and waveguide are also presented. Compact structures like surface mount, and microstrip circulators have miniaturized size, while waveguide circulators typically support high power. This comparison shows a global image of different circulators at X-band in terms of the insertion loss, isolation, power and size.

There are different conceptions to design circulators varying from phase shift circulator to magnetic-free circulator as discussed previously. Each conception has its own advantages. Specific requirements are desired to determine the suitable design of the circulator. In order to support extreme high power, phase shift circulator is preferred. Faraday rotation circulators are often used as isolators. Ring circulators use couplers and phase shifters, however, ring circulators are barely used in practice. Junction circulators are well studied by researchers like H. Bosma and widely used in applications. In order to obtain a wide-band performance, we can use edge-guided circulators. Lumped-element circulators are used at low frequencies with small size. We employ self-biased circulators in applications operating at high frequencies (e.g. > 30 GHz).

Particularly, circulators based on LTCC technology are discussed. LTCC is a good candidate for SiP (system-in-package) system by integrating all active or passive devices into one substrate. This leads to a high integration and miniaturizes the rf front-end circuits. Conventional LTCC technology is not suitable to design ferrite devices because the traditional tape is non-magnetic. However, ferrite devices like circulators could be integrated into the LTCC substrate by co-firing ferrite tape and hence work with other rf components such as power amplifier, filters, mixers, antennas etc.

There are various applications of circulators. The main role is to separate T/R signals. Moreover, circulators could combine several transmitters with a shared antenna. Besides, by connecting a matched load to one of the circulator's ports, an isolator could be obtained.

Isolator is another important ferrite device. Three different conceptions are presented: resonance isolator, field displacement isolator and circulator based isolator. Resonance isolator is based on the gyromagnetic resonance of ferrite, while field displacement isolator relies on the difference of electric field distributions between the forward and reverse waves in a ferrite.

Finally, ferrite switches and phase shifter are discussed. Ferrite switches are mainly realized by controlling the external dc magnetic field. We can switch the ferrite's magnetization state by a current pulse through a wire in ferrite based on ferrite's magnetic hysteresis loop. In phased array antennas systems, we can steer the antenna's beam by electronically controlling the phase shifters. Phase shifter could be designed based on Faraday rotation, which uses the non-reciprocity of ferrites. Moreover, the reggiaspencer phase shifter is a reciprocal phase-shifter. Only a relatively short length is needed to obtain a large reciprocal phase shift. However, the phase shift is very sensitive to the operating frequency.

Chapter 3

Magnetic materials

3.1 Introduction

Magnetic materials are used in many different applications and include a variety of categories. Power stations of electricity widely use magnetic materials [76]. Our storage media like computer disks and audio/video tapes also use magnetic materials as permanent magnets. In the field of medicine, we apply magnetic materials to body scanners. In our daily entertainment, magnetic materials are crucial for CD players, game consoles, loudspeakers etc. Fossil-fuel-free cars require high performance electric motors using advanced magnetic materials. Ferrimagnetic materials having high insulation are commonly used in microwave components such as circulators, phase shifters, isolators, tunable antennas, etc [32]. With the development of the telecommunications industry, high-speed data transmission and miniaturization of handsets are in demand requiring further improvement of magnetic materials [11]. Our modern society cannot work properly without magnetic materials, hence the study of magnetic materials is important to our world.

This chapter begins by outlining the various types of magnetic behaviors: diamagnetism, paramagnetism, ferromagnetism, antiferromagnetism, and ferrimagnetism.

Then different ferrimagnetic materials are presented. Moreover, the theories about ferrimagnetic materials are introduced, including the models of the permeability tensor for saturated ferrite and partially magnetized ferrite, demagnetization factor, loss, hysteresis loop, saturation magnetization, linewidth, etc. The control of the magnetic properties is one of the key aspects in designing magnets, recording media and microwave devices. Finally, ferrite Low Temperature Co-fired Ceramic (LTCC) materials are briefly discussed along with the conventional LTCC fabrication process.

3.2 Classes of magnetic materials

The ancient Egyptians, Greeks and Chinese firstly observed the magnetic phenomena and discovered the magnetic stone. Since then, human has been interested in magnetism. Many observations about the magnetic material like Fe_3O_4 were recorded by them [17].

According to the behavior of the orbital and spin motions under dc magnetic fields, the magnetic materials could be classified into different categories. These behaviors are quite different in various magnetic materials: in some materials, the interaction between the internal magnetic moments and the applied magnetic field is barely observed, while in some other materials, the interaction is firmly strong [32]. Consequently, five major categories of magnetic materials could be drawn: diamagnetic, paramagnetic, ferromagnetic, antiferromagnetic and ferrimagnetic. In other words, based on the phenomena, we can say diamagnetism, paramagnetism, ferromagnetism, antiferromagnetism, and ferrimagnetism [32].

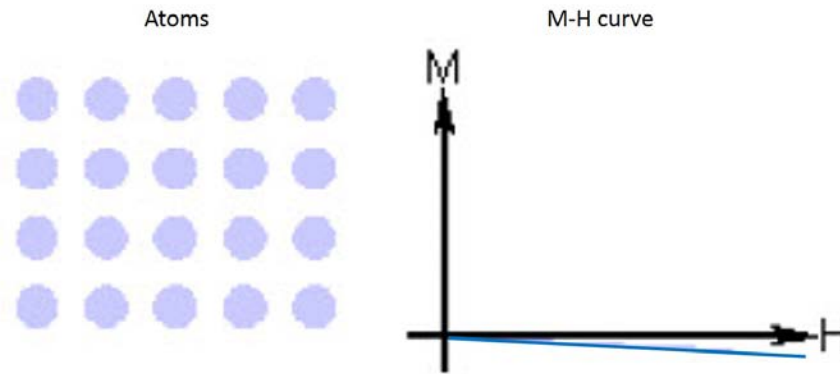


Figure 3.1: Atomic and magnetic behaviour of diamagnetism [11]

3.2.1 Diamagnetism

As in the case of covalent, the shells of the atoms in diamagnetism are closed solids. Diamagnetic materials include, for example, the semiconductors like Ge, Si, and metals such as Au, Cu, Ag, etc. When the diamagnetic material is exposed under a dc magnetic field, a negative internal magnetization appears to fight against the external applied magnetic field [32]. The susceptibility, χ , then, is negative (and weak) as shown in Figure 3.1 [11]. Diamagnetic substances contain the atoms without net magnetic moments. This is a fundamental property of this material because all the orbital shells are occupied leading to zero unpaired electrons. The M-H (M for magnetization and H for magnetic field) curve in Figure 3.1 shows that the magnetization M is in direct proportion to the applied magnetic field H, but the slope is negative (susceptibility is both negative and small).

In addition, the susceptibility χ is temperature independent which is another main character [32]. Generally, diamagnetic materials include all the non-magnetic materials like the semiconductors. However, when the semiconductors are doped with some rare earth elements such as Gd or transition metal elements such as Mn, they could be turned to be magnetic [32].

3.2.2 Paramagnetism

The diamagnetic materials, presented before, have the orbital shells which are filled and no unpaired electrons exist. However, paramagnetic materials possess atoms, molecules and lattice defects which lead to an unpaired number of electrons [32]. Hence, a non-zero total electron spin could appear.

There are some paramagnetic materials which could be attracted when an external dc magnetic field is applied because the induced internal magnetic fields appear and these fields have the same direction as the applied magnetic field [77]. Consequently, paramagnetic materials have a positive and small (usually greater than or equal to 1) susceptibility χ under the dc magnetic fields as shown in Figure 3.2 [11]. The magnetization M goes with the applied magnetic field H (see the M - H curve) in paramagnetic materials. The slope of χ and the internal magnetization are both positive. When the external magnetic field is applied, paramagnetic materials could be slightly attracted, however, when the external magnetic field is removed, the magnetic properties disappear [32].

As explained, the presence of the unpaired electrons and the realignment of the electrons are the main reasons for the paramagnetic material's magnetic behavior [77]. According to the theory of the Langevin model about paramagnetism, the magnetic moment of each atom is randomly oriented because of the thermal agitations. A slight alignment of these moments is possible when a magnetic field is applied. Then a low magnetization having the same direction as the applied field could be obtained. The alignment of magnetization becomes more difficult when the temperature increases and hence the susceptibility becomes weak, as described by the Curie Law [77].

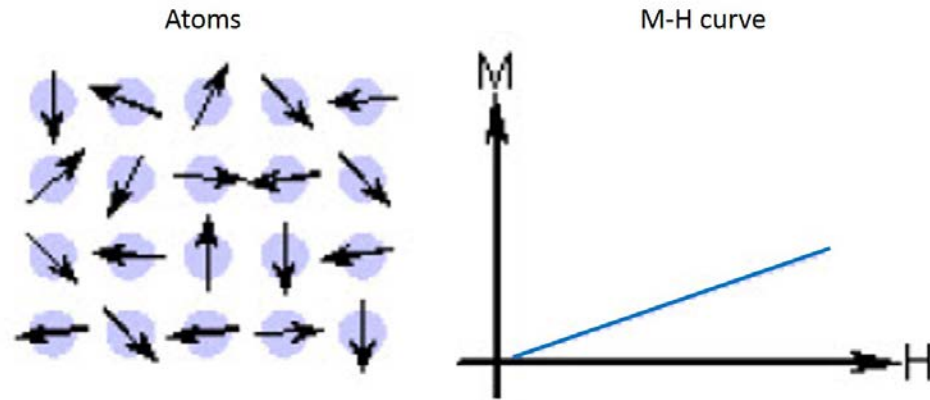


Figure 3.2: Atomic and magnetic behaviour of paramagnetism [11]

3.2.3 Ferromagnetism

Strictly, ferromagnetism is only possible when: 1. the magnetic moments of all the atoms align parallel to each other; 2. atomic magnetic moments follow the applied magnetic field's direction; 3. all atoms are settled in a lattice as shown in Figure 3.3. The fact that all moments of individual atoms are aligned results in a large and positive susceptibility χ and a residual magnetization even when we remove the external magnetic field [32]. Ferromagnetism is basically used to form permanent magnets which can be formed by applying a strong external magnetic field. If we remove the external field, ferromagnetic materials still have the ability to keep the magnetization. Ferromagnetism is widely used in industry and modern technology, especially in a number of electrical and electromechanical devices such as generators, electric motors, electromagnets, transformers, magnetic storage like voice/video tape recorders, and PC hard disks, etc [78].

Initially, a classical theory, postulated first by Weiss in 1907, describes ferromagnetism. It is assumed that there is a molecular field in the ferromagnetic material [32]. Then, the Heisenberg model was proposed. It describes an exchange interaction of the parallel alignment of the magnetic moments between neighboring moments [32].

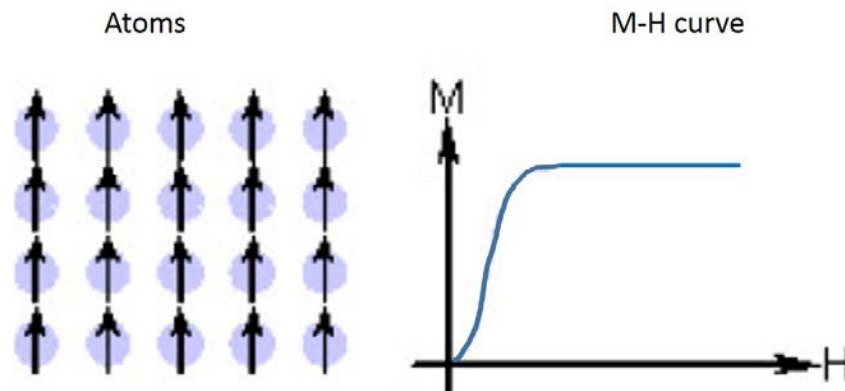


Figure 3.3: Atomic and magnetic behaviour of ferromagnetism [11]

When the temperature is lower than the Curie Temperature T_c , a hysteresis curve can be obtained showing the relation between the magnetization M and the magnetic field H . However, when the temperature goes beyond the Curie temperature, the thermal agitation becomes strong enough so that the materials turn to be paramagnetic. The Curie temperatures for some natural ferromagnetic elements are $T_c(\text{Fe}) = 1043 \text{ K}$, $T_c(\text{Co}) = 1404 \text{ K}$ and $T_c(\text{Ni}) = 631 \text{ K}$ [32].

3.2.4 Antiferromagnetism

Atoms in antiferromagnetic materials have both parallel and anti-parallel aligned magnetic moments as shown in Figure 3.4. The magnetic moments' directions alternate from atom to atom with *equal amplitude* [79]. The net magnetization is not zero so that there is still a small slope (small χ) in M-H curve. When the temperature is below Néel temperature, antiferromagnetism exists, however, the material turns to be paramagnetic when temperature is at or above the Néel temperature [80].

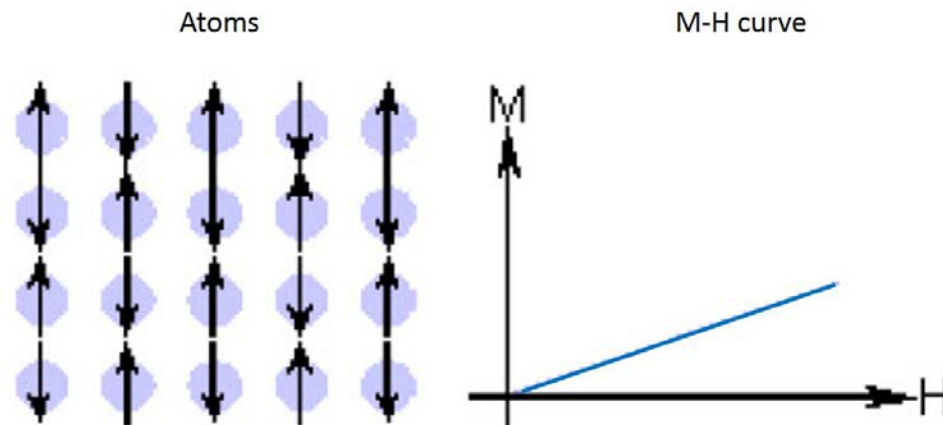


Figure 3.4: Atomic and magnetic behaviour of antiferromagnetism [11]

3.2.5 Ferrimagnetism

Similar to ferromagnetism, ferrimagnetic materials have a positive and large susceptibility which is a function of the applied field H_a . However, the atoms have *unequal* (amplitude) anti-parallel aligned magnetic moments leading to a magnetization saturation M_s [79]. Even at zero Kelvin, not all the moments in ferrimagnetic materials align parallel [32].

The main advantage of ferrimagnetic materials is that they are non-conducting, hence they are widely employed in radio frequency applications as substrates. Since ferrimagnetic material is used in microwave devices as substrates, it is also called microwave ferrite and the next section will introduce more about it.

3.3 Ferrite materials

3.3.1 Introduction

Ferrite materials are used at microwave frequencies, with a high resistivity (not conductors), a low dielectric loss ($\tan\delta \approx 10^{-3}$ or 10^{-4}) and a dielectric constant between

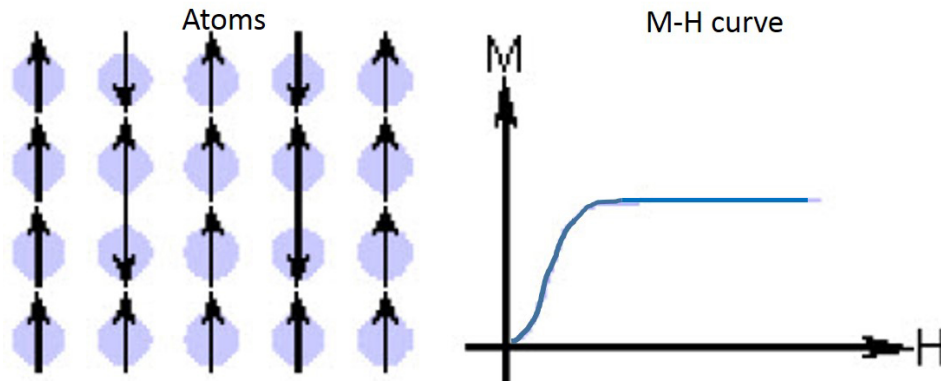


Figure 3.5: Atomic and magnetic behaviour of ferrimagnetism [11]

11 and 17. They are divided into four main categories according to their crystallographic structures [32].

The first is that of spinel ferrites, crystallizing in a face-centered cubic lattice. These are soft ferrites used in inductors, transformers, circulators etc.

The second family concerns the garnets. Their applications lie in the frequency range 0.1 - 10 GHz. YIG (Yttrium-Iron Garnet) is a well known garnet ferrite possessing a magnetic saturation $\mu_0 M_s$ around 0.18 T. Other garnet ferrites, like Y-Al (Yttrium Aluminum) ferrites which have a narrow linewidth (magnetic loss), are utilized to design low-loss devices. Moreover, Dy-Doped (Dysprosium-doped) power ferrite materials are employed for high peak power level applications because of the good temperature stability.

The third family is the hexagonal ferrites, or called hexaferrites, such as barium hexaferrite $BaFe_{12}O_{19}$. These ferrites are used in devices with high frequencies and have a high internal magneto-crystalline anisotropy field.

3.3.2 Different types of ferrite

Spinel

The spinel ferrite has a structure $MeFe_2O_4$, where Me represents the metal. Spinel structure materials are closed packed cubic where Me^{2+} and Me^{3+} are at two different crystallographic sites [79]. Ferrites with spinel crystal structure are mainly used in the frequency range 3-30 GHz [46].

Spinel ferrites are among the most important mineral oxides and a source of metals in the extractive industry. The lodestone or magnet, is the most abundant natural magnetic spinel. Spinel ferrites can be considered as derivatives of magnetite by adding the atoms of other elements like Ni, Mn, Zn, Mg, Li etc. The magnetic properties of spinel ferrites such as permeability, are sensitive to the chemical composition.

There are two principle types of spinel ferrites [14]: 1. Mn-Mg (Manganese-Magnesium) ferrites which are used in devices requiring low magnetic and dielectric losses; 2. Li (or Titanium, Zinc) ferrites which are usually used in the production of temperature-stable components operating at or above X-band.

Garnet

Ferrites with garnet structure are made up of rare-earth elements R^{3+} , such as Gd^{3+} (Gadolinium), Tb^{3+} (Terbium), Y^{3+} (Yttrium) etc and have the general formula $R_3Fe_5O_{12}$. The garnet structure is cubic and the most common form is the iron garnet and yttrium $Y_3Fe_5O_{12}$, known as YIG (Yttrium Iron Garnet). Garnets have a low saturation magnetization M_s and low Curie temperature, limiting their use in the frequency range 10 MHz to 10 GHz. They also exhibit low magnetic losses (ΔH and ΔH_{eff}). This type of ferrites is usually used in applications such as filters and oscillators, as well as in microwave non-reciprocal devices like the YIG resonator and

circulators.

Hexaferrite

The common known structure of hexaferrite is the M-type with the stoichiometric chemical formula $BaFe_{12}O_{19}$. M-type structure has a feature which is "hard", meaning a strong axial magnetic anisotropy up to 2800 kA/m, equivalent to 100 to 1000 times that of spinels or garnets. In practice, permanent magnets are commonly based on the M-type hexagonal barium hexaferrite or BaM. Another main application of this material is the high density magnetic recording medias [81]. Other structures like Z-type, W-type or Y-type, have a planar anisotropy which is "soft", allowing a high permeability in the range of microwave.

The high value of anisotropy in M-type hexaferrite allows the design of millimeter devices in the frequency range from 30 GHz to about 100 GHz. This makes them attractive for the realization of miniaturized devices which do not require huge external polarizations (operated as self-biased). These materials have a saturation magnetization around 400 kA/m ($\mu_0 M_s = 0.5T$), a linewidth greater than 4 kA/m and a Curie temperature about 450 °C [46].

3.4 Basic properties of ferrite materials

3.4.1 Models of permeability tensor

As is known, magnetic materials may be anisotropic, in which case a permeability tensor instead of a constant should be used. This section presents different theories to model permeability tensors for saturated ferrites and partially magnetized ferrites.

Polder (Saturated model)

The existence of magnetic dipole moments leads to the magnetic properties of the ferrite. The magnetic dipole moments come primarily from the electron spin. The *Landé g factor* is a constant to measure the relative contributions of the orbital moment and the spin moment to the total magnetic moment. In practice, $g=2$ is a good approximation for most microwave ferrite materials which signifies that the moment is mostly due to the electron spin. The magnetic dipole moment of an electron due to its spin is given by Equation (3.1) [9].

$$m = \frac{q\hbar}{2m_e} = 9.27 \times 10^{-24} A \cdot m^2 \quad (3.1)$$

where \hbar is Planck's constant divided by 2π , q is the electron charge, and m_e is the mass of the electron [9]. Moreover, the spin angular momentum of an electron is given by Equation (3.2).

$$s = \frac{\hbar}{2} \quad (3.2)$$

Another important constant is *gyromagnetic ratio* γ which is the ratio of the spin magnetic moment to the spin angular momentum as expressed by Equation (3.3). In addition, these two vectors are oppositely directed as shown in Figure 3.6.

$$\gamma = \frac{m}{s} = 1.759 \times 10^{11} C/Kg = 2.8MHz/Oe \quad (3.3)$$

If the ferrite medium is infinite and a magnetic bias field $\vec{H}_0 = \vec{z}H_0$ is present, the motion of the magnetic dipole moment could be derived (see Equation (3.4)) [9].

$$\frac{d\vec{m}}{dt} = -\mu_0\gamma\vec{m} \times \vec{H}_0 \quad (3.4)$$

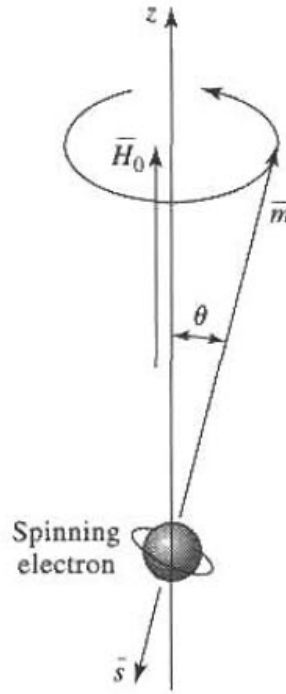


Figure 3.6: A spinning electron: Spin magnetic dipole moment (\vec{m}) and angular momentum vectors (\vec{s}) [9]

Moreover, if an applied AC field \vec{H} is present and the magnetization M reaches the saturation M_s , then the equations of motion for the forced precession of the magnetic dipoles, assuming small-signal conditions, could be expressed by Equation (3.5), where $\omega_0 = \mu_0\gamma H_0$ and $\omega_m = \mu_0\gamma M_s$.

$$\frac{d^2 M_x}{dt^2} + \omega_0^2 M_x = \omega_m \frac{dH_y}{dt} + \omega_0 \omega_m H_x \quad (3.5a)$$

$$\frac{d^2 M_y}{dt^2} + \omega_0^2 M_y = \omega_m \frac{dH_x}{dt} + \omega_0 \omega_m H_y \quad (3.5b)$$

Besides, when the AC \vec{H} field has an $e^{j\omega t}$ time-harmonic dependence, these equations could be re-written with a tensor susceptibility, $[\chi]$ to relate \vec{H} and \vec{M} as shown in Equation (3.6).

$$\vec{M} = [\chi]\vec{H} = \begin{bmatrix} \chi_{xx} & \chi_{xy} & 0 \\ \chi_{yx} & \chi_{yy} & 0 \\ 0 & 0 & 0 \end{bmatrix} \vec{H} \quad (3.6)$$

The elements of χ are given by Equation (3.7):

$$\chi_{xx} = \chi_{yy} = \frac{\omega_0\omega_m}{\omega_0^2 - \omega^2} \quad (3.7a)$$

$$\chi_{xy} = -\chi_{yx} = \frac{j\omega\omega_m}{\omega_0^2 - \omega^2} \quad (3.7b)$$

Hence Equation (3.8) relates \vec{B} and \vec{H} by the permeability tensor when the magnetic bias is in the \vec{z} direction, where μ_+ and μ_- is the effective permeability for RHCP (Right Hand Circular Polarization) wave and LHCP (Light Hand Circular Polarization) wave, respectively.

$$\vec{B} = \mu_0(\vec{M} + \vec{H}) = [\mu]\vec{H} \quad (3.8a)$$

$$[\mu] = \mu_0([U] + [\chi]) = \begin{bmatrix} \mu & j\kappa & 0 \\ -j\kappa & \mu & 0 \\ 0 & 0 & \mu_0 \end{bmatrix} \Leftarrow (\vec{z} - bias) \quad (3.8b)$$

$$\mu = \mu_0\left(1 + \frac{\omega_0\omega_m}{\omega_0^2 - \omega^2}\right) \quad (3.8c)$$

$$\kappa = \mu_0\frac{\omega\omega_m}{\omega_0^2 - \omega^2} \quad (3.8d)$$

$$\mu_+ = \mu + \kappa \quad (3.8e)$$

$$\mu_- = \mu - \kappa \quad (3.8f)$$

If the ferrite is biased in other directions, the permeability tensor could be transformed according to the change in coordinates as demonstrated by Equation (3.9a) [82] where α , β and γ is the angle against the axis x, y and z respectively. When H_0 is parallel to the axis x, it is easy to find $\cos\alpha = 1$ and $\cos\beta = \cos\gamma = 0$ leading to Equation (3.9b). When H_0 is parallel to the axis y, then $\cos\beta = 1$ and $\cos\alpha = \cos\gamma = 0$ resulting in Equation (3.9c).

$$[\mu] = \begin{bmatrix} \mu(\mu_0 \text{ when } \vec{x} \text{ biased}) & j\kappa\cos\gamma & -j\kappa\cos\beta \\ -j\kappa\cos\gamma & \mu(\mu_0 \text{ when } \vec{y} \text{ biased}) & -j\kappa\cos\alpha \\ j\kappa\cos\beta & j\kappa\cos\alpha & \mu(\mu_0 \text{ when } \vec{z} \text{ biased}) \end{bmatrix} \quad (3.9a)$$

$$[\mu] = \begin{bmatrix} \mu_0 & 0 & 0 \\ 0 & \mu & -j\kappa \\ 0 & -j\kappa & \mu \end{bmatrix} \Leftarrow (\vec{x} - \text{bias}) \quad (3.9b)$$

$$[\mu] = \begin{bmatrix} \mu & 0 & -j\kappa \\ 0 & \mu_0 & 0 \\ j\kappa & 0 & \mu \end{bmatrix} \Leftarrow (\vec{y} - \text{bias}) \quad (3.9c)$$

Figure 3.7 [82] shows the geometrical relations between μ_+ , μ_- , μ , κ , μ_{eff} and

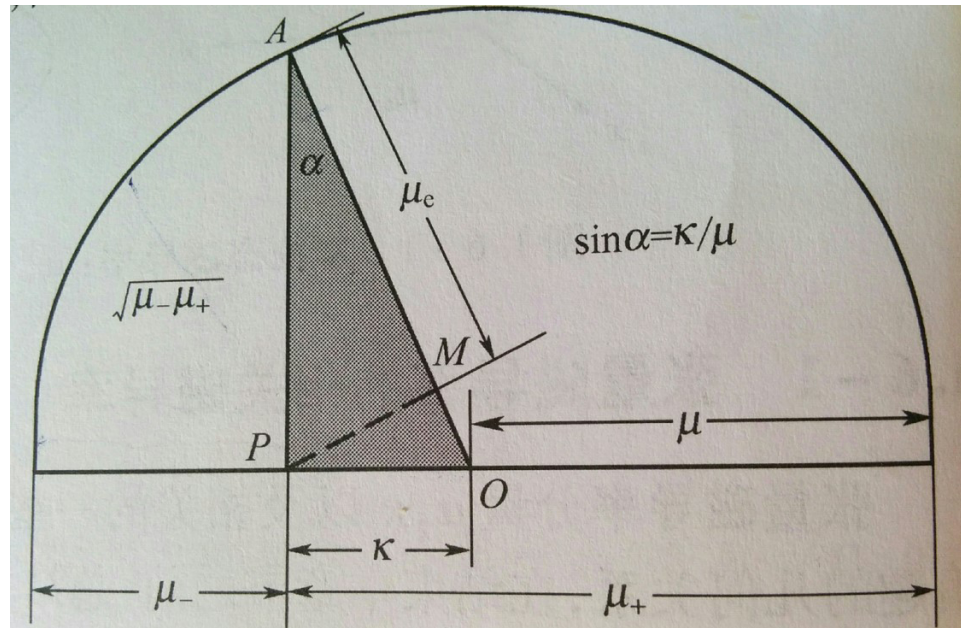


Figure 3.7: Geometric relation of different elements of permeability tensor

$\mu_+\mu_- = \mu^2 - \kappa^2$ according to Equations (3.8e) and (3.8f). The non-reciprocity increases with the increase of $\sin\alpha = \frac{\kappa}{\mu}$. Noting that when $\kappa = 0$ then $\sin\alpha = \frac{\kappa}{\mu} = 0$ leading to the disappearance of non-reciprocity.

The above is the well-known Polder model. Since ferrites are commonly used under saturated state, this model is predefined in many EM simulators to perform ferrite-based simulations. However, partially magnetized ferrites are also used, because a small internal magnetic H field could easily vary the internal magnetization M which is useful for miniaturized tunable devices [27]. Next parts will present the theories about demagnetized ferrites and partially magnetized ferrites.

Schlömann (Demagnetized Model)

Enlightened by a study of coaxial configuration where parallel and antiparallel domains are alternatively magnetized, Schlömann [83] developed his theory based on

a magnetostatic approximation. This theory takes into consideration the interactions between domains of opposite magnetization [84]. When the ferrite is completely demagnetized, the diagonal values of the permeability tensor have an accurate approximation for the isotropic permeability [84]. Schlömann shows that the permeability μ_r takes the following form as shown by Equation (3.10a), where μ_{eff} is defined in Equation (3.10b) and the H_a is the anisotropy field [83].

$$[\mu_r] = \begin{bmatrix} \mu_{eff} & 0 & 0 \\ 0 & \mu_{eff} & 0 \\ 0 & 0 & \mu_{eff} \end{bmatrix} \quad (3.10a)$$

$$\mu_{eff} = \frac{1}{3} + \frac{2}{3} \left[\frac{(H_a + 4\pi M_0)^2 - (\omega/\gamma)^2}{H_a^2 - (\omega/\gamma)^2} \right]^{0.5} \quad (3.10b)$$

Based on the assumptions of E. Schlömann, the internal field is identified with the anisotropy field of the material as the applied field is completely offset by the static demagnetizing fields. This model is only valid when a ferrimagnetic material is totally demagnetized.

Rado (Partially Magnetized Model)

Another theory, proposed by Rado [85], saying that we perform a spatial average of the responses produced by all domains in the ferrite. When the frequencies exceed the gyroresonance frequency, Rado's theory offers an accurate value for the extra-diagonal term κ , but the diagonal ones ($\mu = \mu_z = 1$) are not accurate [84]. Unfortunately, this theory does not take into consideration the interactions between adjacent areas. The results obtained by Rado are expressed by Equations (3.11a) and (3.11b), where $\omega_m = \mu_0 \gamma M_s$. It is assumed that the working frequency is much higher than the

resonant frequencies $\omega \gg \omega_0$ [46].

$$\mu = \mu_z = 1 \quad (3.11a)$$

$$\kappa = -\frac{\omega_m}{\omega} \frac{M}{M_s} \quad (3.11b)$$

Igarashi and Naito (Partially Magnetized Model)

Igarashi and Naito [86] presented a formula for the transverse diagonal term in a partially magnetized state ferrite. This model is a further improvement of the tensor model of Schlömann. In the publication [87], the expressions of the tensor terms are given by Equations (3.12a) to (3.12d), where α is a phenomenological loss term, $\omega_M = -\gamma M_s/\omega_0$, γ is the gyromagnetic ratio, μ_0 is the intrinsic permeability of free space, and ω_e is a parameter concerned with the effective dc field. However, we need to perform some preliminary measurements to determine the ω_e , especially when the magnetic field H is relatively high.

$$\mu_z = 1 + (\mu - 1)\left[1 - \left(\frac{M}{M_s}\right)^2\right] \quad (3.12a)$$

$$\mu = 1 + \frac{\omega_m(\omega_e + j\alpha\omega)}{(\omega_e + j\alpha\omega)^2 - \omega^2} \quad (3.12b)$$

$$\kappa = -\frac{\omega_m\omega}{(\omega_e + j\alpha\omega)^2 - \omega^2} \quad (3.12c)$$

$$\omega_e = \gamma H_a \quad (3.12d)$$

Gelin GPT (Generalized Permeability Model)

Previous theories use actually the average responses of each domain. For example Schlömann developed a model "magnetostatic" by taking into account the interaction domains with antiparallel magnetization. In the case where the ferrite is demagnetized, the model is in good agreement with the experiment. However, Schlömann cannot process the case of partially magnetized ferrites.

To describe the permeability of the ferrites (saturated, partially magnetized or demagnetized) correctly, a theoretical approach was developed [84, 88–90]. Mathematically, this approach means solving two coupled evolution following Equations (3.13a) and (3.13b), where n is a demagnetizing factor which depends on the shape of the ferrite, h are the microwave magnetic field, H_1 and H_2 , M_1 and M_2 , m_1 and m_2 is the static magnetic field, macroscopic magnetization, and the magnetization dynamics induced by \vec{h} in the domain 1 and domain 2, respectively.

$$\frac{d\vec{M}_1}{dt} = \gamma\vec{M}_1 \times (\vec{H}_1 + \vec{h} - n(\vec{m}_1 - \vec{m}_2)) + \frac{\alpha}{M_s}\vec{M}_1 \times \frac{d\vec{M}_1}{dt} \quad (3.13a)$$

$$\frac{d\vec{M}_2}{dt} = \gamma\vec{M}_2 \times (\vec{H}_2 + \vec{h} - n(\vec{m}_2 - \vec{m}_1)) + \frac{\alpha}{M_s}\vec{M}_2 \times \frac{d\vec{M}_2}{dt} \quad (3.13b)$$

The permeability tensor based on the Equations (3.13a) and (3.13b) allows a more rigorous description of the interaction between the rf signal and the magnetic moments in ferrites. This model also considers the dynamic interactions between adjacent magnetic fields via the Polder-Smit effect when these domains appear in the material. The interactions between the grains and the hysteresis phenomenon are also considered. By altering the dynamic demagnetizing effects between neighboring domains of the ferrite, and therefore by changing the distribution of the values of

the frequencies of gyromagnetic resonance, the Polder-Smit effect induces the spreading of magnetic losses in relation to the frequency. This has in fact been observed experimentally in unsaturated materials [46].

This model is valid for saturated, partially magnetized and demagnetized ferrites. It is accurate, however, it is difficult to be implemented into EM simulator because of the integral equations.

Green and Sandy (Partially Magnetized Model)

In this thesis, we use Green and Sandy's model. Based on the measurements of the experimental characterization cells, Green and Sandy [91] have obtained all the tensor values when ferrite is totally demagnetized. They developed the diagonal terms (μ and μ_z) which are compatible with Schlömanns formula for a totally demagnetized ferrite [84].

The equations for the tensor elements of a partially magnetized ferrite material when using Z-bias are given by Equations (3.14a) to (3.14f), where μ'_0 is the initial relative permeability of the substrate in the demagnetized state, ω is the device's operating frequency, the relative μ and κ values replace the standard elements of the Polder permeability tensor, M and M_s are the partial and saturation magnetization, respectively and n is the coefficient expressing the deviation of κ from Rado's mode.

$$\text{Permeability} = \mu_0 \begin{bmatrix} \mu & -j\kappa & 0 \\ j\kappa & \mu & 0 \\ 0 & 0 & \mu_z \end{bmatrix} \quad (3.14a)$$

$$\mu'_0 = \frac{2}{3} \left[1 - \left(\frac{\gamma 4\pi M_s}{w} \right)^2 \right]^{0.5} + \frac{1}{3} \quad (3.14b)$$

$$\mu = \mu'_0 + (1 - \mu'_0) \left(\frac{M}{M_s} \right)^{1.5} \quad (3.14c)$$

$$\kappa = n \frac{\gamma 4\pi M}{w} \quad (3.14d)$$

$$\mu_z = \mu'_0 \left(1 - \left(\frac{M}{M_s} \right)^{2.5} \right) \quad (3.14e)$$

$$\mu_{eff} = \frac{\mu^2 - \kappa^2}{\mu} \quad (3.14f)$$

The model is valid when the operating frequency is higher than the resonance, and it has been used to analyze an antenna based on a partially magnetized ferrite LTCC substrate ESL 40012 and has proven to be a good approximate model [28].

Therefore, we use Green and Sandy's model in this thesis because it is valid for our design and relatively easy to be used in our simulators. Moreover, it has been employed on ferrite LTCC ESL 40012 substrate which is also used in this thesis.

3.4.2 Demagnetization factors

When the ferrite is not infinite, the internal bias field H_0 is generally different from the externally applied field H_a . According to the boundary conditions at the surface of the ferrite, the magnetic flux \vec{B} is continuous when the applied field is perpendicular to the ferrite plate. However, the magnetic field H is not continuous. Equation (3.15) demonstrates that the internal magnetic bias field is $H_0 = H_a - M_s$. Of course, when applied field is parallel to the ferrite plate, then the magnetic field \vec{H} is continuous leading to $H_0 = H_a$.

$$B = \mu_0 H_a = \mu_0 (M_s + H_0) \quad (3.15)$$

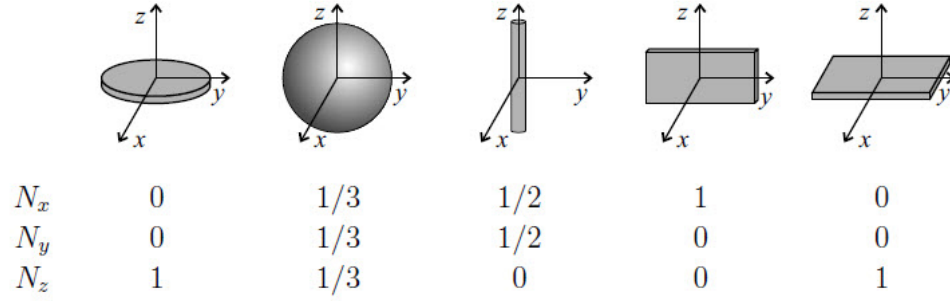


Figure 3.8: Demagnetization factors of some simple shapes [12]

Generally, the demagnetization factor (N) is used to measure the deduction of the applied field as is shown by Equation (3.16), where $N=N_x$, N_y or N_z . The demagnetization factors are defined such that $N_x + N_y + N_z = 1$. A few simple shapes' demagnetization factors are listed in Figure 3.8 [12].

$$\vec{H}_i = \vec{H}_a - N\vec{M} \quad (3.16)$$

The demagnetization factor is also related to the internal and external rf fields near the boundary of a ferrite sample. This leads to the Kittel's equation which is used to calculate the *resonance frequency* ω_r as shown by Equation (3.17), where H_a is the applied magnetic field [92].

$$\omega_r = \mu_0\gamma\sqrt{[H_a + (N_x - N_z)M_s][H_a + (N_y - N_z)M_s]} \quad (3.17)$$

3.4.3 Effect of loss

If the damping factor α is also considered, the Polder tensor elements are given by Equations (3.18) and (3.19a) to (3.19d) [9]:

$$\chi_{xx} = \chi'_{xx} - j\chi''_{xx} \quad (3.18)$$

$$\chi_{xy} = \chi''_{xy} + j\chi'_{xy}$$

$$\chi'_{xx} = \frac{\omega_0\omega_m(\omega_0^2 - \omega^2(1 - \alpha^2))}{(\omega_0^2 - \omega^2(1 + \alpha^2))^2 + 4\alpha^2\omega^2\omega_0^2} \quad (3.19a)$$

$$\chi''_{xx} = \frac{\alpha\omega\omega_m(\omega_0^2 + \omega^2(1 + \alpha^2))}{(\omega_0^2 - \omega^2(1 + \alpha^2))^2 + 4\alpha^2\omega^2\omega_0^2} \quad (3.19b)$$

$$\chi'_{xy} = \frac{\omega\omega_m(\omega_0^2 - \omega^2(1 + \alpha^2))}{(\omega_0^2 - \omega^2(1 + \alpha^2))^2 + 4\alpha^2\omega^2\omega_0^2} \quad (3.19c)$$

$$\chi''_{xy} = \frac{2\alpha\omega^2\omega_0\omega_m}{(\omega_0^2 - \omega^2(1 + \alpha^2))^2 + 4\alpha^2\omega^2\omega_0^2} \quad (3.19d)$$

Then the lossy tensor $[\mu]$ can be calculated using Equation (3.8b). The *damping factor* α has a relation with the linewidth of ferrite materials which is shown by Equation (3.20) [9]. Ferrite materials with higher linewidth ΔH have more magnetic losses. Noting that this loss is separate from the dielectric loss that a ferrimagnetic material may have at the same time.

$$\Delta H = \frac{2\alpha\omega}{\mu_0\gamma} \quad (3.20)$$

3.4.4 Hysteresis loop

Figure 3.9 [13] shows an example of a magnetic hysteresis loop regarding the induced magnetic flux density (B) in terms of the magnetic field (H). The hysteresis loop of a ferromagnetic material could be obtained by tracing the function of internal magnetic

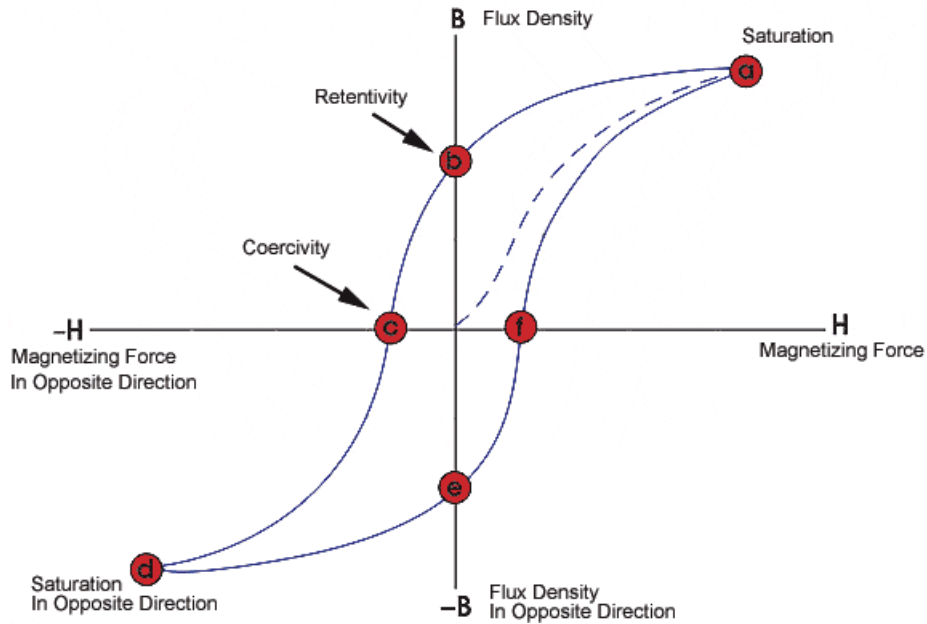


Figure 3.9: An example of magnetic hysteresis loop [13]

flux B as the applied magnetic field H . It's important to note that when the ferromagnetic material is the first time to be magnetized or it has been totally demagnetized, magnetic flux density B will follow the dashed line, also called the initial line, as shown in Figure 3.9. Magnetic field flux B is proportional to H , however, when all the magnetic moments in the ferromagnetic material are aligned, the increase of H will hardly contribute to the increase of B , hence the material reaches the saturation point (point a). Now, if we remove the applied H , the magnetic flux will drop to point b, meaning that there are still some aligned magnetic moments. This refers to the retentivity of the ferromagnetic material. The presence of retentivity is a key property for ferromagnetic, and is widely used to produce permanent magnets. It is worthwhile to note that when the magnetic field H is reversed, B will move to point c, also called the point of coercivity, which suggests that the magnetic flux is reset-off to zero (demagnetized). The magnetic field H required to release the residual magnetism of the ferromagnetic material is called coercivity [13].

Similarly, the ferromagnetic material could have the magnetic saturation when H is increased in the opposite direction. This time the saturation is the point d as shown in the figure. The release of H will move the curve to point e . The residual magnetism is the same as obtained in the opposite direction. In this case, a positive H should be used to bring B back to zero. It is noteworthy that the curve will follow the line from point f to point a instead of the initial dash line if H continues increasing [13].

Some important magnetic properties could be obtained based on the hysteresis loop:

Retentivity: The remaining internal magnetization (the point b in the hysteresis curve) of a magnetic material when the external dc magnetic field H is removed.

Residual Magnetism or *Residual Flux*: The residual magnetism equals to retentivity when the material reaches the magnetic saturation and then the applied magnetic field H is released. However, if the material does not reach the saturation, the residual magnetism is smaller than the retentivity.

Coercive Force: The magnetic field needed to bring the magnetic flux density B back to zero (the value of H at point c)

Maximum Energy Product (BH_{max}): It measures the maximum energy product of a magnetic material, which uses the unit Mega Gauss Oersteds (MGOe)

Squareness: It is the result of the saturation remanence (residual magnetization) divided by the saturation magnetization.

Material Grade: The manufactured neodymium (NdFeB) magnets are classified into different grades. Generally, the stronger magnet has higher grade. The typical range of grades is N35 to N52 for neodymium magnets. The limit for neodymium magnets is the grade N64 in theory, meaning that it isn't currently possible to realize the magnets such strong. The grade of commercialized magnets is usually N42 because N42 provides the optimal trade-off between strength and cost.

3.4.5 Magnetization M_s

As explained before, with the increase of the applied field, more magnetic dipoles are aligned, until all are aligned. In this case, \vec{M} reaches its upper limit called magnetic saturation M_s . Since the ferrite material is a soft magnetic material, a small field (close to coercive force H_c) of about 1 to few Oe is enough to get the magnetization value M close to its saturated maximum M_s (values of $\mu_0 M_s$ are in the range 29 mT to 500 mT).

3.4.6 Curie Temperature T_c

By increasing the temperature of the ferrite, the aligning of the spins parallel to the H field is more and more difficult due to the thermal agitation. The magnetization becomes null at the Curie Temperature T_c , which is in the range of $120^\circ C$ to $650^\circ C$ [14].

3.4.7 Linewidth ΔH

Figure 3.10 [9] shows the definition of the linewidth: the width of the curve of χ'' (see Equation (3.19b)) versus H_0 (internal magnetic field) where χ'' has decreased to half of its peak value. The damping factor, α , is related to the linewidth, ΔH , as explained by Equation (3.20).

3.4.8 Effective linewidth ΔH_{eff}

The insertion loss of the ferrite device is related to the magnetic loss in ferrites. The imaginary part of the permeability of the positive polarization χ'' (or μ'') indicates this loss. Generally, effective linewidth ΔH_{eff} increases when the gyromagnetic line

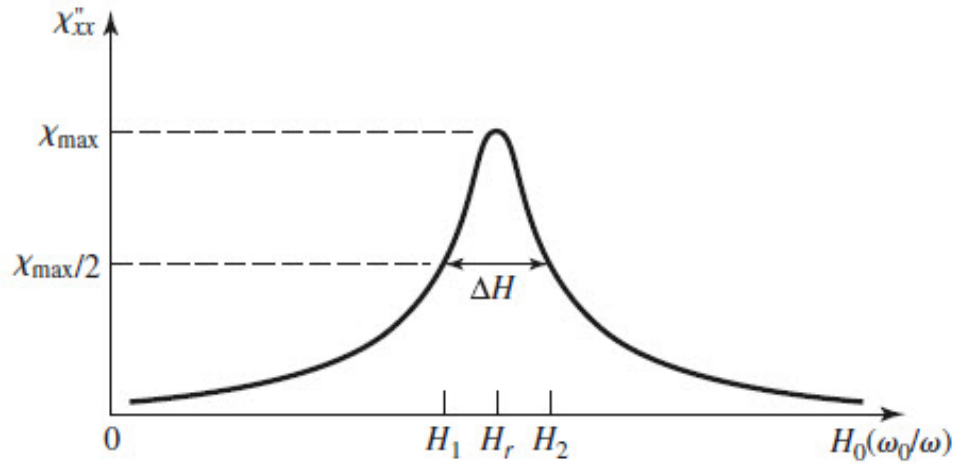


Figure 3.10: Definition of the linewidth ΔH [9]

width ΔH increases.

We commonly use a Lorentz curve to model μ'' far away from the resonance as shown in Figure 3.11 [14]. Accordingly, the effective line width ΔH_{eff} is smaller than ΔH . The reason why the line width is broadened when near the resonance is that the porosity and magneto crystalline anisotropy in ferrites increase the losses. Since the ΔH_{eff} is more accurate when the ferrite is far from resonance, there is much practical interest [14].

3.4.9 Spin wave linewidth ΔH_k

Nonlinear phenomena could be observed when the microwave power exceeds a threshold. Non-linearity brings additional magnetic loss and generates other frequencies which are not desired in our devices. The effect of non-linearity is related to the magnetic microwave field h_c which depends on the external dc magnetic field. The presence of the spin waves is usually considered as the reason of nonlinear effects, which is described by ΔH_k as shown in Figure 3.12. For a certain static magnetic field H denoted H_{sub} , there is a minimum of the microwave magnetic field h_c related

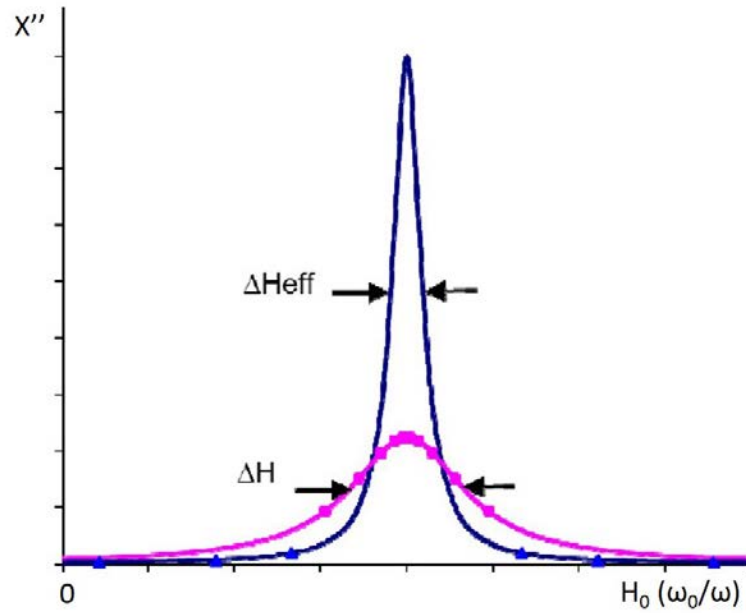


Figure 3.11: Definition of the effective linewidth ΔH_{eff} [14]

to ΔH_k as explained by Equation (3.21) [14]. The high power capability could be achieved by increasing the value of ΔH_k . The typical value of ΔH_k is from 1 to more than 20. The relation between the line widths mentioned till now is $\Delta H_k < \Delta H_{eff} < \Delta H$.

$$hc_{min} = \frac{2f\Delta H_k}{\gamma M_s} \quad (3.21)$$

3.4.10 Permittivity and loss tangent

Besides the magnetic properties, the ferrite's dielectric properties are also important for microwave applications. The relative real permittivity ϵ' determines the real wave-length and wave impedance in ferrites. The typical value is about 12 to 16. Meanwhile, the relative imaginary part of the permittivity ϵ'' or the dielectric loss tangent determines the dielectric loss. We usually measure the dielectric loss tangent

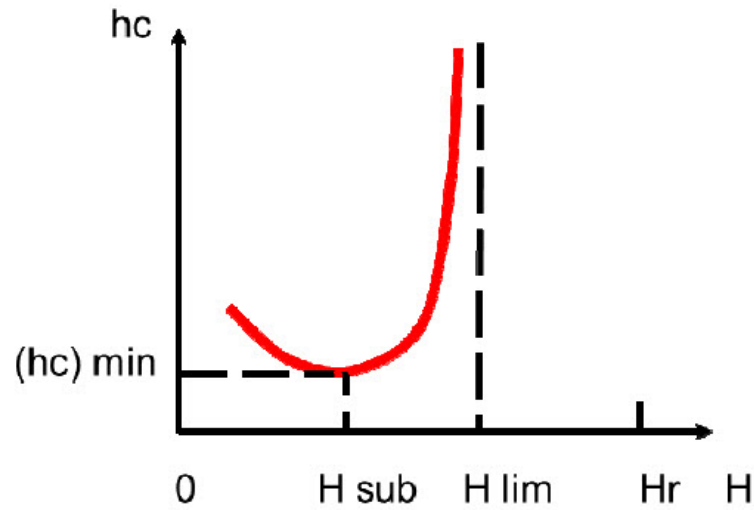


Figure 3.12: Definition of the spin wave linewidth ΔH_k [14]

$\tan\delta$ at 10 GHz. Generally, $\tan\delta$ is small and ranges between 10^{-4} and 10^{-3} for most ferrimagnetic materials at 10 GHz. Therefore, the insertion loss of the device is more affected by the magnetic losses in this range [14].

3.5 Ferrite LTCC

3.5.1 Introduction

There are currently few commercially available ferrite LTCC materials, none special for microwave. The tape used in this thesis is ESL 40012 from ESL ElectroScience (USA) which could be a magnetic tape for high frequency applications with multi-layers. These applications usually require a permeability, higher than 400. The tape is a flexible cast film as shown in Figure 3.13 where magnetic powder is dispersed in an organic matrix. In order to get a dense body, we need a fired-temperature of 885°C . We can print metallized circuits on each sheet of the tape, then a pressure/temperature combination of 14 MPa and 70°C is used to laminate several sheets.



Figure 3.13: Photo of ESL 40012 ferrite tape ('green' tape)

A silicone-coated polyester film is also employed to protect the tape from being contaminated by the environment. The polyester film also improves the mechanical strength, and convenience of handling [93].

3.5.2 Characterization of ESL 40012

Hysteresis curve

The ferrite LTCC material ESL 40012 ferrite has been already characterized by previous works [15]. Magnetostatic characterization is performed by the measurements of hysteresis. Important ferrite characteristics such as the saturation magnetization, relative permeability, squareness and coercivity could be obtained. Two different types of transformers have been designed: 1. a straight solenoid transformer completely embedded within the ferrite LTCC material (Figure 3.14(a) [15]); 2. a toroid transformer designed in which unit cells are closely spaced and the fields are more tightly contained within the windings (Figure 3.14(b) [15]).

When we inject a peak current of 650 mA into the winding, the measured hysteresis curves from the embedded transformers could be shown in Figure 3.15 [15]. The magnetic saturation B_s is measured to be 0.33 T when a magnetic field of 2.1 kA/m

is applied in the solenoid winding. The remanent flux density B_r is 0.18 T, the squareness (saturation remanence divided by saturation magnetization) is 0.55, and the coercive magnetic field H_c is 520 A/m. Similarly, we measured these parameters when toroid winding is used. However the turn density of the toroid is lower than that of the solenoid because of the different curvature of the toroid. The B-H curve for the toroid is shown in Figure 3.15 by a solid line.



Figure 3.14: LTCC (a) solenoid transformer unit cell cross section and (b) toroid transformer tilted front view [15]

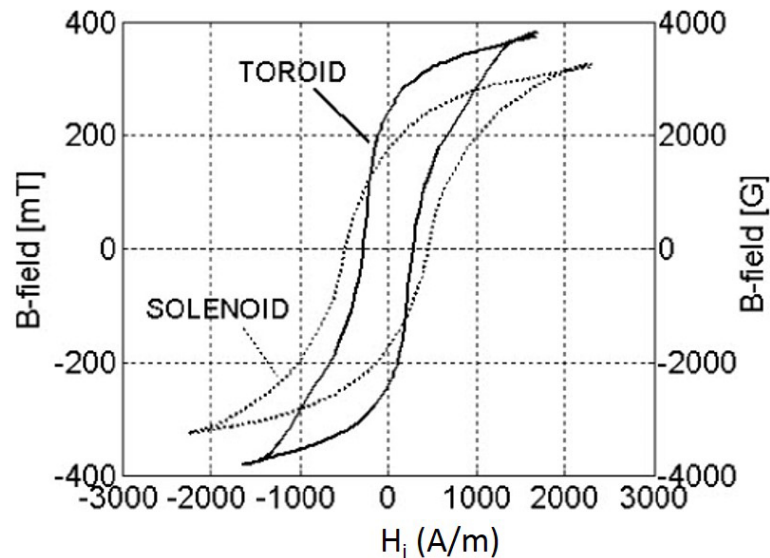


Figure 3.15: Measured hysteresis curves from the LTCC transformers [15]

Magnetic Saturation M_s

Figure 3.16 [15] shows the curve B-H which could be used to model the non-linearity in Maxwell 3D. Although saturation could not quite be achieved only with the toroid, the trend clearly indicates that the magnetization saturation $\mu_0 M_s$ approaches 400 mT instead of the 330 mT obtained using the solenoid. A small internal H-field higher than 2500 A/m is needed to saturate it. For the toroid, $B_r = 250$ mT, the squareness is approximately 0.63, and $H_c = 330$ A/m [15].

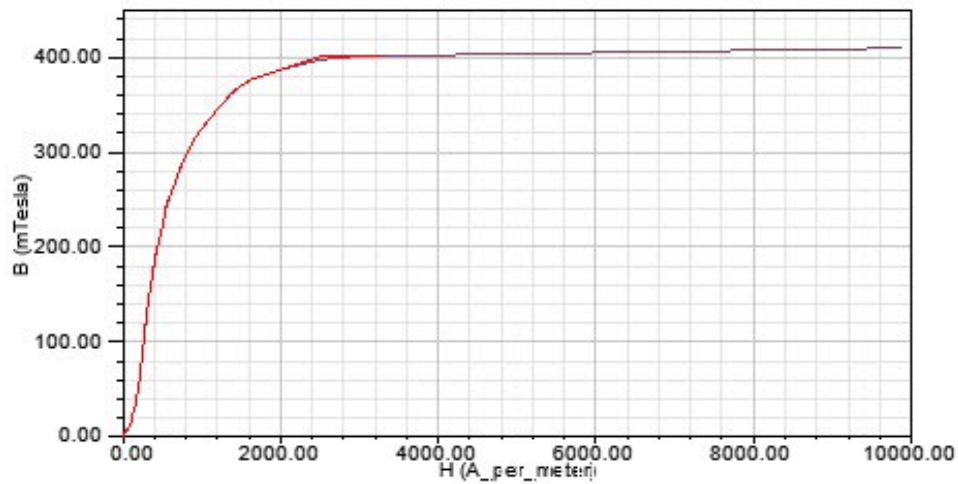


Figure 3.16: B-H curve (first magnetization) used in EM simulator

Losses

This material is very lossy below 10 GHz due to the low-field losses, especially when it is completely demagnetized as shown in Figure 3.17 [15]. The magnetization frequency is defined as $f_m = \gamma\mu_0 M_s$ (11.2 GHz). So, according to the previous remarks, an operating frequency higher than 14 GHz for our circulators is chosen far from the lossy frequency area to avoid low-field losses. Moreover, this material has a relative permittivity $\epsilon_r=14.6$ and a dielectric loss tangent 4.24×10^{-3} .

The damping factor α is found to be around 0.35 by measuring a CPW transmission line on ESL 40012 [94]. Hence the line width ΔH equals 250 Oe according to Equation (3.20) [9].

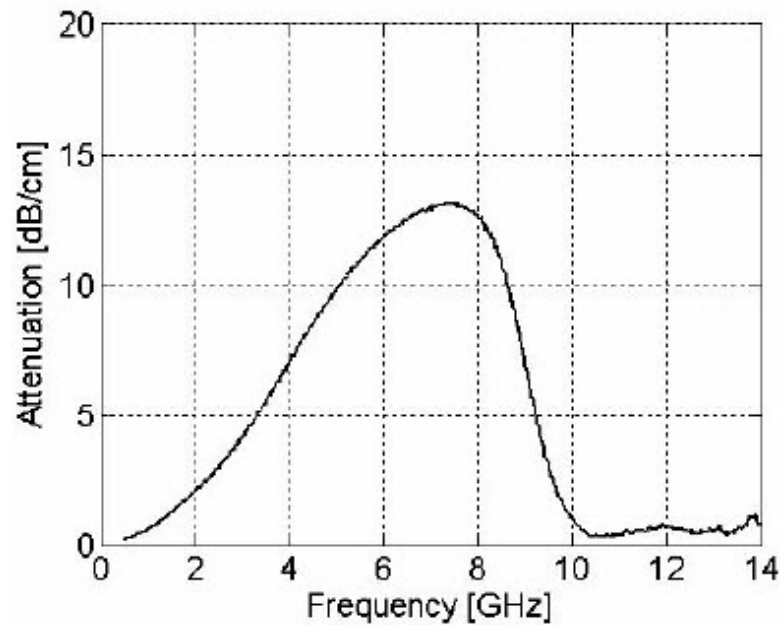


Figure 3.17: Attenuation constant in terms of frequency

Curie Temperature T_c

Ring samples using ESL 40012 LTCC tape with 64 layers were realized [95]. Then the B-H curve measurements were performed in dependence on environment temperature as shown in Figure 3.18.

From the dependence of the maximum polarization with temperature, we can estimate the value of the Curie temperature to be higher than 100°C . Saturation polarization, coercivity, as well as remanence vanish at temperatures above T_c . Due to the finite resolution of the measurement system the observation of the maximum polarization with temperature seems to give the most reliable estimate for T_c . The

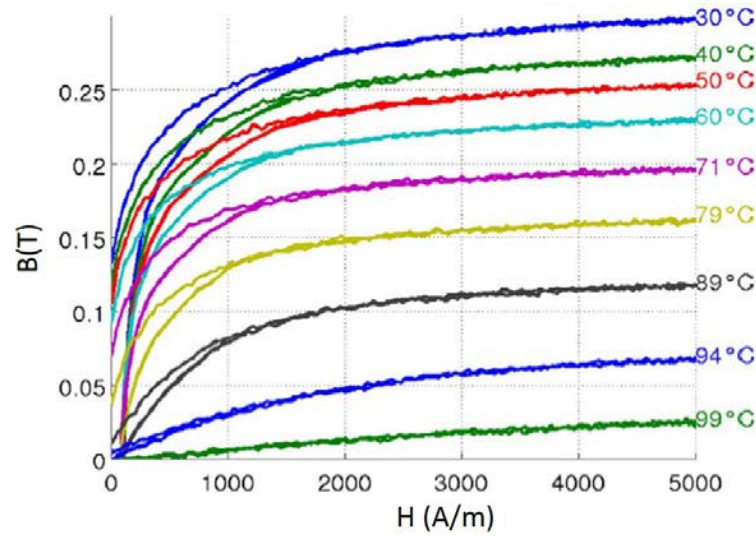


Figure 3.18: Major magnetization curves of the ESL 40012 sample at different sample temperatures, magnetic polarization B (T) versus magnetic field H (A/m). The maximum magnetic field was 5 kA/m for all curves.

maximum magnetic magnetization $\mu_0 M_s$ is 0.3 T which is in agreement with the measured $\mu_0 M_s$ in Figure 3.15 when solenoid transformer was used. However, a measurement of VSM (Vibrating Sample Magnetometer) was also performed in our laboratory LT2C showing that the magnetization saturate $\mu_0 M_s$ loses 50% at 100°C.

Other properties and summary

The principle parameters are presented before such as the hysteresis curve, magnetization saturation M_s , losses and Curie temperature T_c . The list below concludes the characterization of ferrite LTCC ESL 40012 including some other physic fired tape properties [93].

- Relative permittivity: $\epsilon_r = 14.6$
- Loss tangent: $\tan\sigma = 4.24 \times 10^{-3}$
- Magnetization saturation: $\mu_0 M_s = 0.4$ T

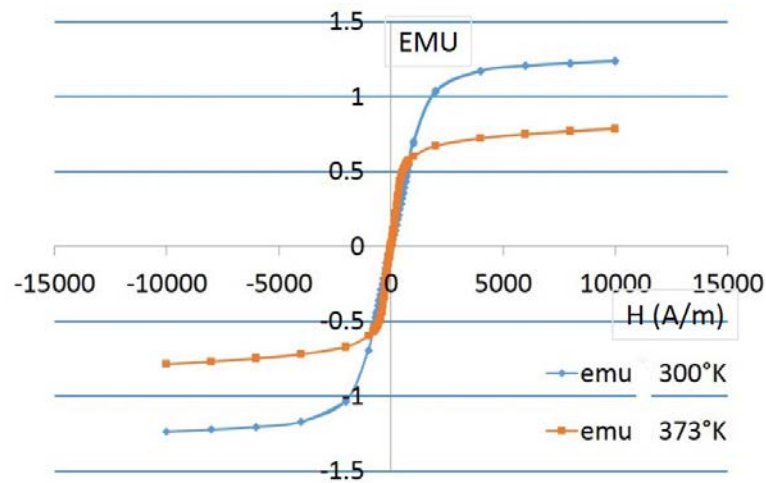


Figure 3.19: The VSM (Vibrating Sample Magnetometer) measurement performed by laboratory LT2C shows that the magnetization saturation $\mu_0 M_s$ loses 50% at 100°C

- Internal magnetic field to saturate the ferrite: $H_i > 2500\text{A/m}$
- Linewidth: $\Delta H = 250\text{ Oe}$
- B-H curve: Figure 3.16
- Remanence: $B_r = 250\text{ mT}$
- Coercivity: $H_c = 330\text{ A/m}$
- Curie Temperature: $T_c \geq 100^\circ\text{C}$
- Layer thickness: $t = 110\mu\text{m}$
- Insulation resistance: $\geq 10^8\ \Omega$
- Thermal Coefficient of Expansion: $9.4\text{ppm}/^\circ\text{C}$
- Breakdown voltage: $1000\text{V}/25\mu\text{m}$
- Fired shrinkage (x and y): 17%

- Fired shrinkage (z): 16.5%
- Fired density: 5.35 g/cm³

3.5.3 Rf behavior of saturated ferrite

Circulator's functionality lies on the ferrite material, so it is necessary to study the properties of ferrites to find the operating point of our circulators. As said before, the working frequency of our circulators is assumed to be higher than 14 GHz. In order to explain the ferrite's rf behavior with different DC magnetic fields and magnetization saturations, the elements κ and μ in Polder tensor are normalized by the operating frequency leading to the property of the ferrite itself (independent of frequency). Two variables are then defined:

- $\sigma = \gamma\mu_0 H_i/\omega$ which shows the normalized strength of the internal magnetic field H_i
- $p = \gamma\mu_0 M_s/\omega$ which shows the normalized magnetization saturation of the ferrite M_s

Then the elements κ and μ of the permeability tensor can be reformed by Equations (3.22a) and (3.22b) where α is the damping factor. The μ_{eff} and $\frac{\kappa}{\mu}$ can also be expressed in terms of p and σ as shown by Equations (3.22c) and (3.22d).

$$\mu = 1 + \frac{p(\sigma + j\alpha)}{(\sigma + j\alpha)^2 - 1} \quad (3.22a)$$

$$\sigma = \frac{p}{(\sigma + j\alpha)^2 - 1} \quad (3.22b)$$

$$\mu_{eff} = \frac{\mu^2 - \kappa^2}{\mu} = 1 + \frac{p\sigma}{\sigma^2 - 1} - \frac{p^2}{(\sigma^2 + p\sigma - 1)(\sigma^2 - 1)} \quad (3.22c)$$

$$\frac{\kappa}{\mu} = \frac{p}{\sigma^2 + p\sigma - 1} \quad (3.22d)$$

Figure 3.20 shows that when $\sigma = 1$, the material is very lossy due to the resonance ($\omega = \omega_0$) [9]. Isolators can be designed based on this resonance. The zone beyond $\sigma = 1$ is called the *high H_i zone* and the zone below $\sigma = 1$ is called the *low H_i zone*. Either high or low H_i zone could be used to operate a circulator [82]. High H_i means more powerful external magnet should be applied leading to a bigger size and more weight of the device.

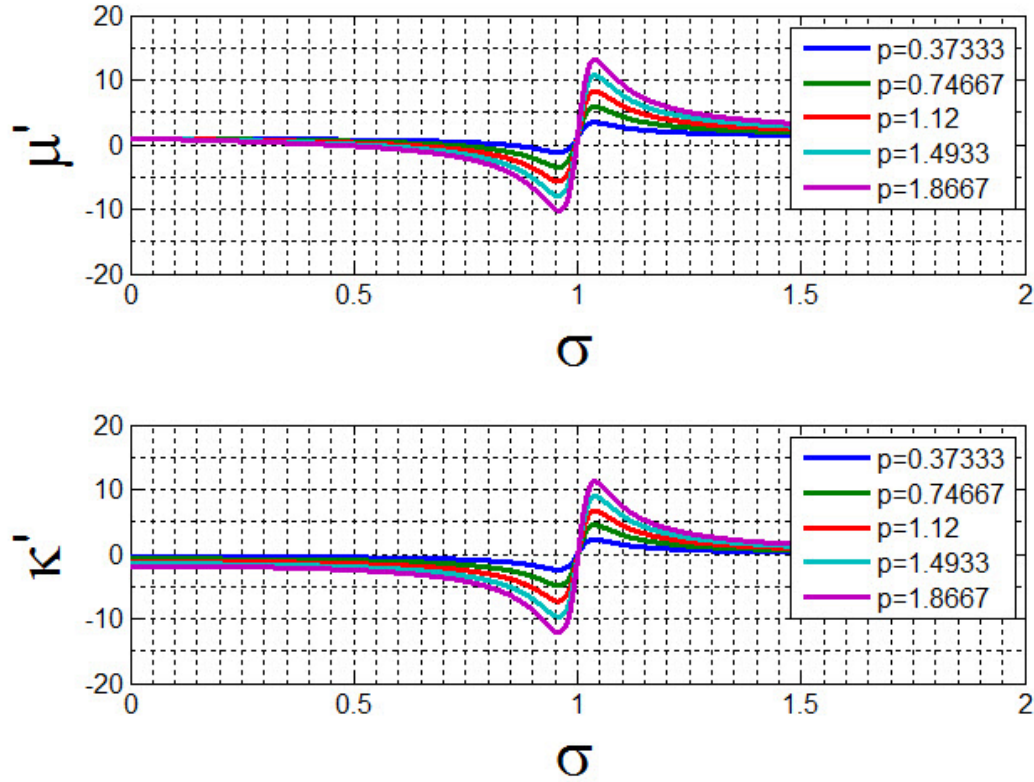


Figure 3.20: μ' and κ' in terms of σ

The second part (losses) of μ and κ along with the σ is shown in Figure 3.21. It demonstrates that the loss increases with the increase of the p . This is the reason

why a low M_s ferrite should be used to design a low frequency circulator in order to avoid unnecessary losses. In the vicinity of the resonance, the attenuation is indeed strong. Moreover, in high H_i zone, the μ'' and κ'' could be smaller than those in low H_i zone, which could be used to design low-loss devices.

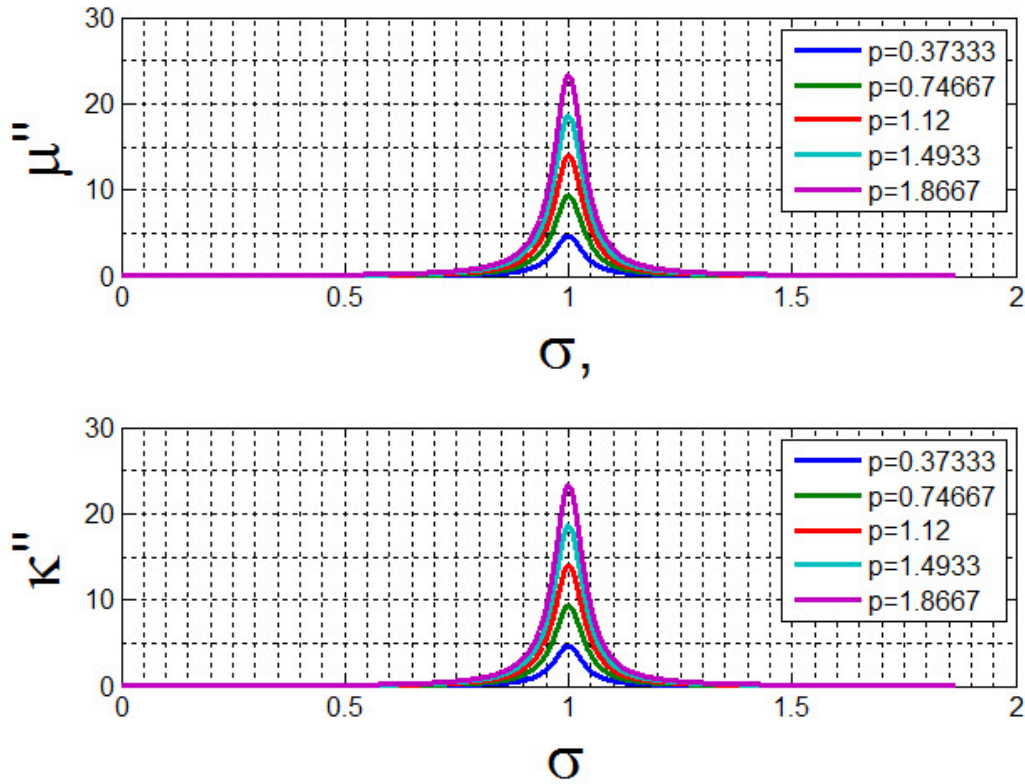


Figure 3.21: μ'' and κ'' in terms of σ

In practice, the μ_{eff} and κ_{eff} are more important, because they take into account the interaction between the ferrite and the rf signals. Figure 3.22 shows that the real resonance frequency shifts towards the left, which makes the low H_i zone smaller compared with that in Figure 3.20. In addition, the low H_i zone further shrinks with the increase of the p , which explains why high M_s ferrite is not suitable for low frequency circulator when using a low H_i injection. Besides, the μ'_{eff} becomes

negative when $p > 1$ in low H_i zone, which means the cut-off mode. So a ferrite with too high M_s doesn't work in low H_i zone. However, in high H_i zone, μ_{eff} is always positive which allows to design a circulator even a high M_s ferrite is used.

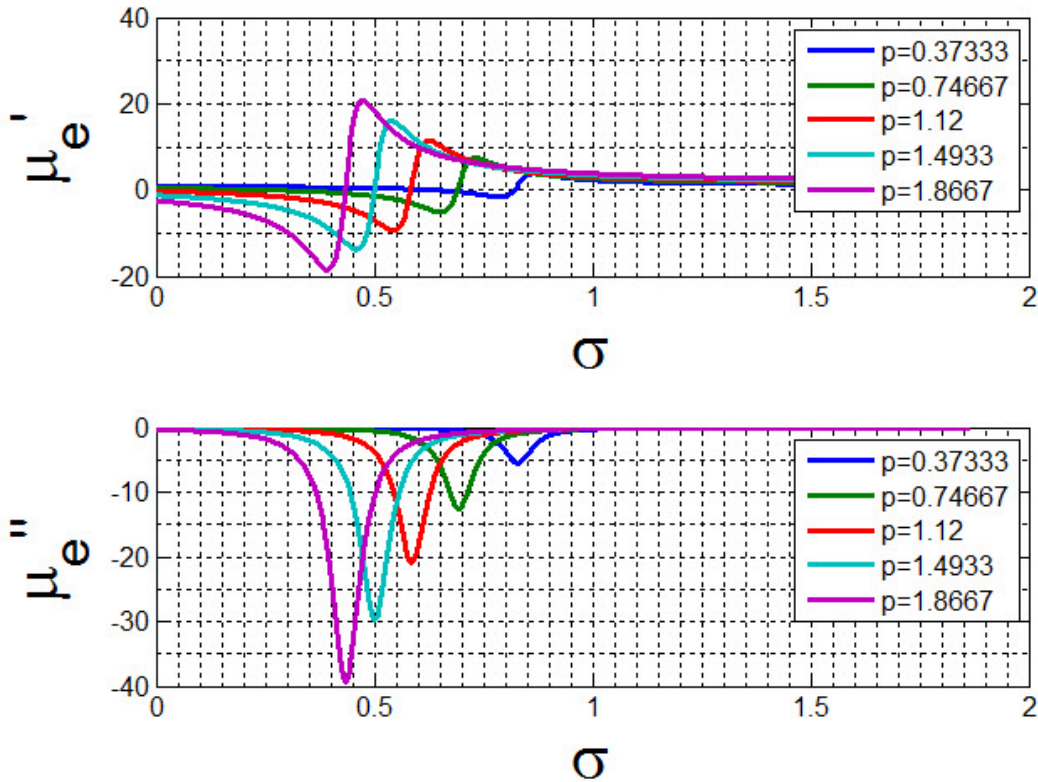


Figure 3.22: μ_{eff} in terms of σ

Figure 3.23 shows the $\frac{\kappa}{\mu}$ which indicates the capability of the non-reciprocity. As expected, higher p introduces more non-reciprocity which could be used to design high frequency circulators, but it introduces more losses. That is why it is a challenge to design high frequency circulators with low losses.

In conclusion, ESL 40012 ferrite tape has a $\mu_0 M_s = 0.4$ T, therefore, $p = 0.74667$ which is the green line when frequency $f = 15$ GHz (or $p = 0.8$ when $f = 14$ GHz). The

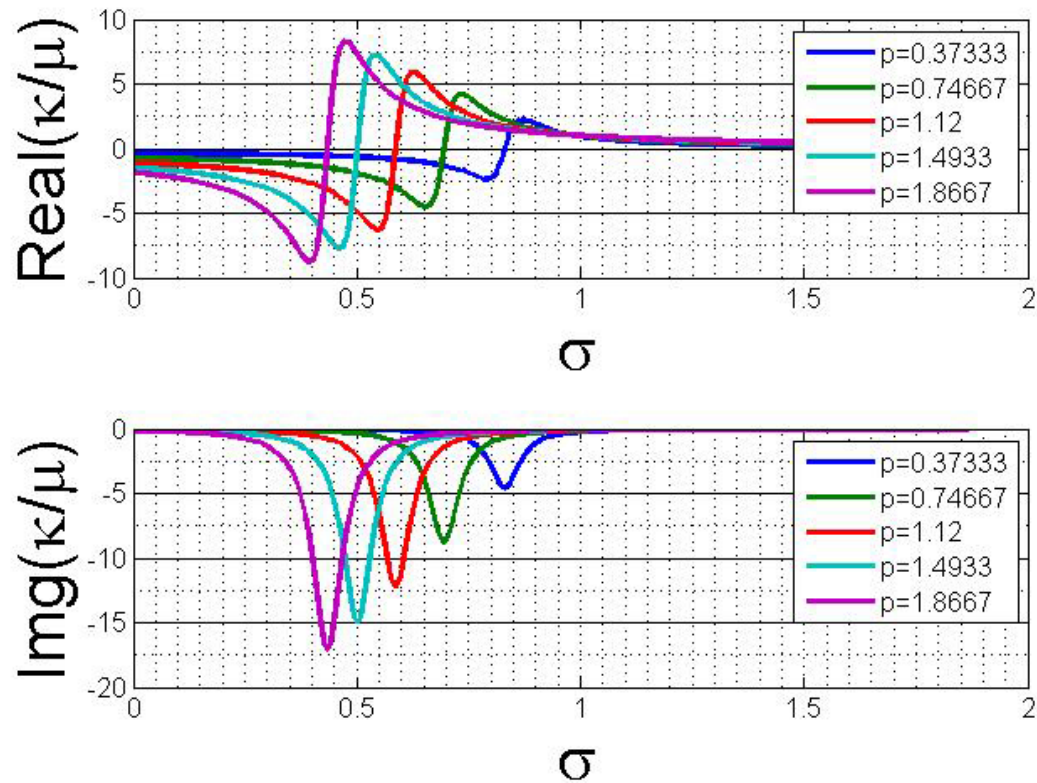


Figure 3.23: κ on μ in terms of σ

low H_i zone is then chosen to use a small internal magnetic field and have a relatively low loss.

3.5.4 Rf behavior of partially magnetized ferrite

Typically, external magnetic field intensity H is in order of 80 kA/m to saturate the ferrites and required magnets having large sizes make the system extremely bulky and unsuitable for compact SiP applications. An elegant solution to this problem of bulky electromagnets is to embed the bias windings into the ferrite substrate itself leading to the ferrite partially magnetized. Therefore, in this section, we will study the rf behavior of partially magnetized ferrites. The ferrite ESL 40012 has a $\mu_0 M_s = 400$

mT and the partially magnetized ferrite model 'Green and Sandy' (Equations (3.14a) to (3.14f)) is used to estimate the elements of the permeability tensor.

Figure 3.24 shows that the κ and μ increase with the increase of the internal magnetization M when $\mu_0 M_s = 400$ mT. As discussed before, $\frac{\kappa}{\mu}$ signifies the non-reciprocity, so higher magnetization introduces more non-reciprocity as demonstrated in Figure 3.25. The fact that μ_{eff} is a function of magnetization could be used to analyze the frequency variation of our ferrite LTCC circulator with integrated winding later.

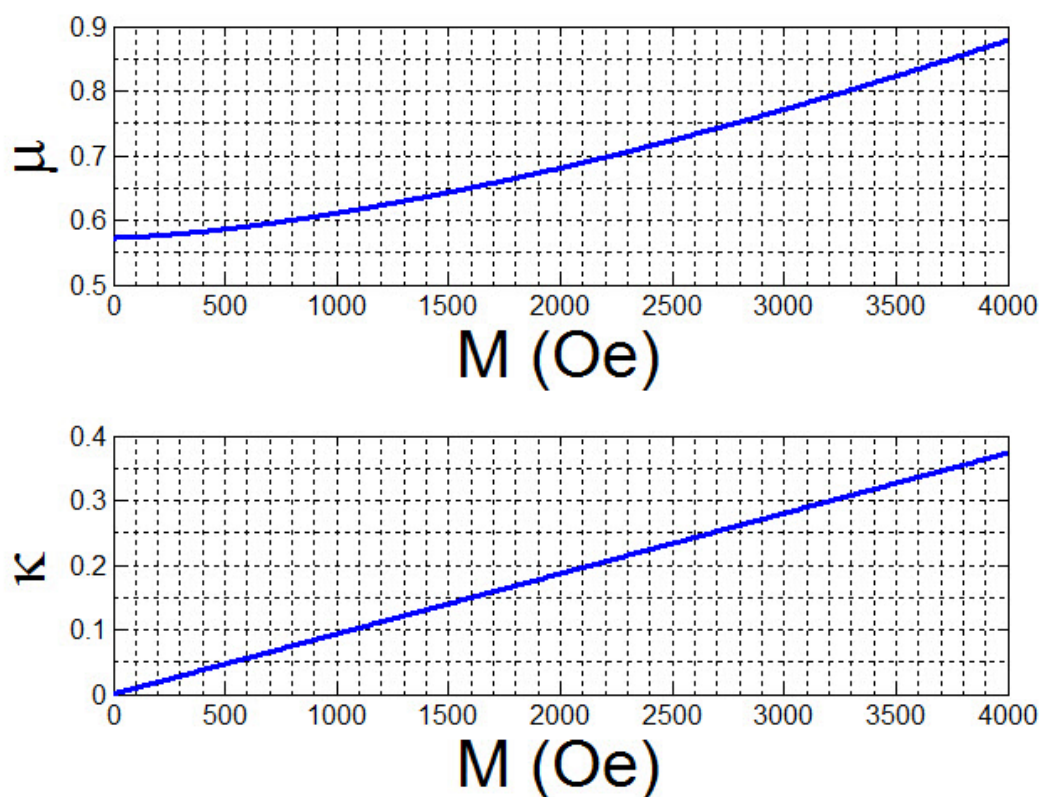


Figure 3.24: κ and μ in terms of internal magnetization M

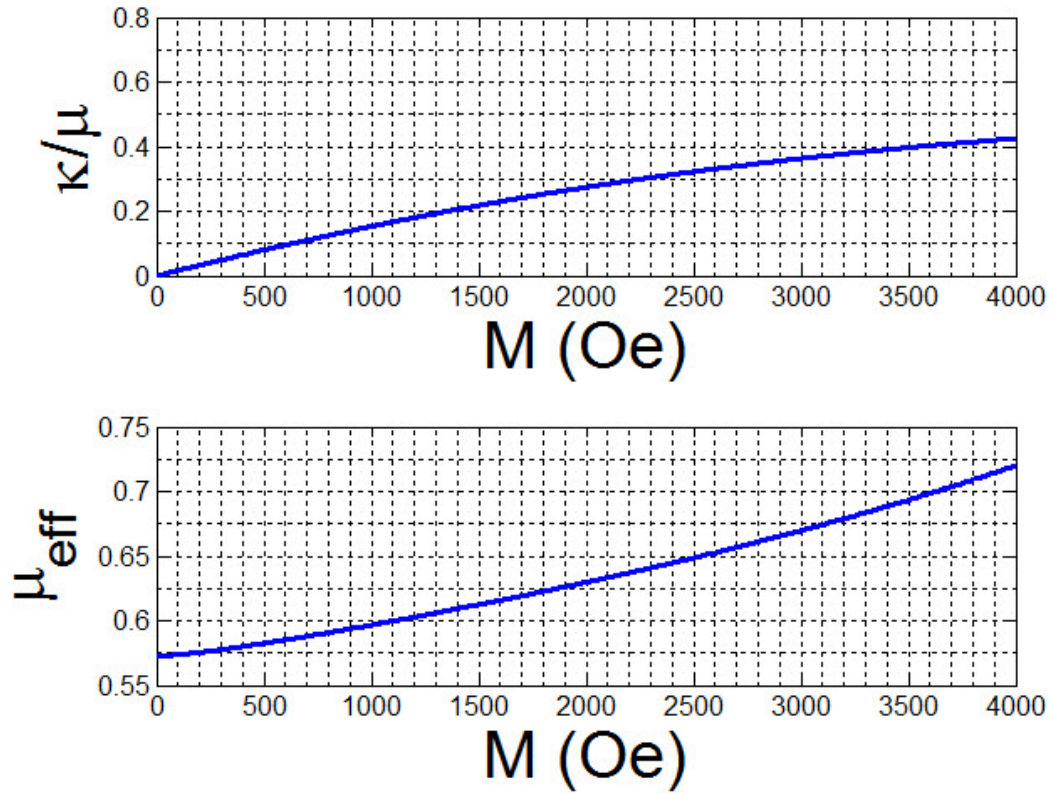


Figure 3.25: $\frac{\kappa}{\mu}$ and μ_{eff} in terms of internal magnetization M

3.5.5 Conventional LTCC fabrication process

Although the fabrication of ferrite LTCC devices may be different from that of the conventional LTCC devices, the principle procedures of fabrication are almost the same [96]. The basic manufacturing process for multilayer LTCC substrates is shown in Figure 3.26 [16]. A milky slurry is made by mixing the ceramic/magnetic powder and organic binder. The green sheet of the LTCC is then obtained by casting the slurry into the tape and cut by a doctor blade. This raw sheet is a paper-like flexible film. We can now print the desired circuits on the sheet and realize the vias. After aligning all the sheets of LTCC, a combination of temperature and pressure is used to laminate them. Finally the device is fired, according to the material's profile and

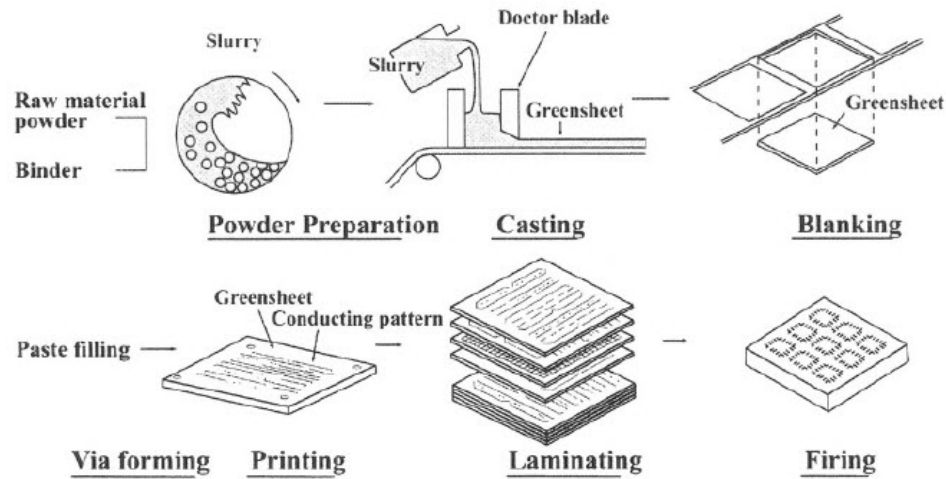


Figure 3.26: Typical multilayer ceramic substrate manufacturing process [16]

get the final structure. The challenge is the different shrinkage rates of materials such as metal and ceramic. The variation of temperature, pressure, lamination quality etc will directly affect the final device [16].

3.5.6 Recent ferrite LTCC research works

Ferrite Low Temperature Co-fired Ceramic (LTCC), which is originally used to design inductors, now could be used in high frequency applications. This section will present some recent ferrite LTCC work.

The ferrite LTCC tape from Ferro Corporation was firstly characterized using circuits that are fabricated by Dr Joey R. Bray, Dr. Kari T. Kautio and Dr. Langis Roy [96] in 2004. This work has demonstrated that high quality ferrite LTCC circuitry can be fabricated using standard processing techniques, which is an essential requirement for low cost high volume production.

In 2007, another commercial ferrite LTCC tape ESL 40012 (ESL ElectroScience) was characterized in [15]. The measured relative permittivity ϵ_r is 13.6 at 9.86 GHz. The $\tan\delta$ values is 0.004 and 0.001 at 9.86 GHz and 27.2 GHz respectively. When

toroid winding is integrated in the ferrite LTCC, the measurement extracts a magnetic saturation $\mu_0 M_s$ of 400 mT, with a remanence of 250 mT, and a coercivity of 330 A/m. The approximate linear relative permeability is 370.

Tunable antennas for SoP (system on package) application were then developed [27]. The winding embedded in the ferrite could produce a controllable magnetostatic field which could make the antenna's frequency tunable. Due to the lack of the demagnetization factor, the embedded winding greatly reduces the required bias field for a frequency tuning by over 95%. This property makes ferrite LTCC an ideal substrate for tunable system-on-package applications because we don't need bulky electromagnets.

Then a theoretical model was described to explain the partially magnetized ferrite antenna's frequency tuning [28]. The authors use the theoretical model of Green and Sandy to calculate the terms of the permeability tensor when the ferrite is partially magnetized. Then these values are used to predict the antenna's frequency shifting. Measurement shows the agreement between the calculation and simulation.

Moreover, a helical antenna has been developed using ten layers of ferrite LTCC. The helical winding is designed to act as antenna and bias coil at the same time [97]. This idea firstly reduces the size of the antenna because external bias could be removed. Besides, the integrated winding could avoid demagnetization factor, hence reduce the required tuning dc magnetic field. The measurement shows a tuning range of 10% of the operating frequency (13 GHz). The design is compact, light-weight, low cost and highly suitable for tunable microwave systems .

Besides, a half mode substrate-integrated waveguide (SIW) phase shifter based on ferrite LTCC was presented in [98]. Similar to the tunable antenna's design, the biasing is realized by integrating a winding in the ferrite LTCC substrate. This removes the external electromagnets and avoids wasting energy caused by demagnetization

field. The ferrite is partially magnetized by the winding, hence the required bias fields have been greatly reduced. The measurement demonstrates that a phase shift of 83.2° and a figure of merit of $83.2^\circ/\text{dB}$ could be achieved at the operating frequency of 13.1 GHz.

Finally, the heat effects created by embedded windings were studied [99]. By a number of simulations and measurements, the authors get a model which has a good agreement with the measurement. The study shows that the center frequency of the filter could be shifted by about 1 GHz when we heat the device externally from 0°C to 190°C . Besides, when the integrated winding is energized by 260 mA, the internal temperature is about 250°C leading to a frequency shifting more than 2%.

Circulators, as one of the important ferrite devices, have never been designed on the ferrite LTCC substrate. This is the principal purpose of this thesis. A winding could be integrated into the circulator's structure to achieve multi-functionality. Chapter 4 will present our work on the circulator design, winding design and the measurements.

3.6 Conclusion

This chapter has highlighted the different types of magnetic materials, including diamagnetic, paramagnetic, ferromagnetic, antiferromagnetic and ferrimagnetic materials. Diamagnetic materials have a negative magnetization against the applied magnetic field leading to a small and weak susceptibility. However, paramagnetic materials could be attracted by an externally applied magnetic field because of a small and positive susceptibility. Ferromagnetism is basically used to form permanent magnets because all moments of individual atoms could be aligned resulting in a large susceptibility. Antiferromagnetic materials have mixed (unpaired) parallel and antiparallel

aligned magnetic moments with equal amplitude, while the total net magnetization is still small. Ferrimagnetic materials have unequal antiparallel aligned magnetic moments leading to a large susceptibility and a saturation magnetization. Ferrimagnetic materials are non-conducting, so they are used in microwave devices.

Since ferrimagnetic materials are widely used in microwave devices, we introduce more about the ferrite. Spinel ferrites are among the most important mineral oxides and a source of metals in the extractive industry. The lodestone or magnet, is the most abundant natural magnetic spinel. The garnet structure is cubic and the most common form is the iron garnet and yttrium $Y_3Fe_5O_{12}$, known as YIG (Yttrium Iron Garnet). Permanent magnets and high density magnetic recording medias are two main applications based on the M-type hexagonal barium hexaferrite or BaM.

After talking about the different types of ferrite, we focus on the basic properties of ferrite materials. As a non-reciprocal magnetic material, a permeability tensor is used instead of a constant. Polder model is the most common known model which explains the behavior of ferrite under saturated condition. Schlömann developed a model for demagnetized ferrites. Then Rado developed a theory which provides a good approximation for the extra-diagonal term κ , but inaccurate values for the diagonal ones ($\mu = \mu_z = 1$). By using experimental characterization cells, Green and Sandy have measured all the tensor components as a function of the ferrite magnetization state. Igarashi and Naito presented a formula for the transverse diagonal term in a partially demagnetized state ferrite. This model is a further improvement of the tensor Schlömann. To describe the permeability tensor of the ferrites (saturated, partially magnetized or demagnetized) correctly, a generalized approach was developed by Gelin, Quéffélec and other researchers. We also present the demagnetization factor, because the internal bias field H_0 is generally different from the externally applied field H_a . When the damping factor is considered, the loss of ferrites could be calculated,

leading to the definition of linewidth including the linewidth ΔH , effective linewidth ΔH_{eff} and spin wave linewidth ΔH_k . Hysteresis loop is then described resulting in the definition of magnetization M_s , retentivity, residual magnetism, coercive Force, maximum energy product (BHmax) and squareness.

Ferrite LTCC is next presented. In particular, the characterization of ESL 40012 ferrite tape is introduced. We show the principle parameters including the hysteresis curve, magnetization saturation M_s , losses and Curie temperature T_c along with other physic fired tape properties. The rf behaviors of both saturated and partially magnetized ferrite are predicted by our Matlab program. Finally the recent ferrite LTCC research works are presented varying from the characterization of the substrate to tunable antennas and phase shifters designs.

In the next Chapter, we will demonstrate how to design ferrite LTCC circulators based on this ESL 40012 substrate.

Chapter 4

Modeling and realizations of circulators

4.1 Introduction

The design of a stripline Y-junction circulator is generally based on the work of H. Bosma [5]. Usually, a stripline Y-junction circulator is made of two metal plane grounds, a center conductor with three ports and a ferrite disk surrounded by dielectric materials. For this conception, ferrite materials at microwave frequencies are usually operated under the saturation state and Polder equations are employed to calculate the permeability tensor by taking into account the applied static magnetic field H_0 , the magnetization M_s , the operating frequency and the damping factor α (or ΔH), etc [37]. However, partially magnetized ferrite has advantages in frequency tunability by varying internal magnetization M easily.

In this chapter, a CPW transmission line on ferrite LTCC is firstly realized to have an intimate knowledge of ferrite LTCC design, then different structures of circulators such as stripline, microstrip and coplanar structures are described, followed by the theory and mathematical calculations of a stripline junction circulator. Three ferrite LTCC circulators are finally presented: one is with external magnets and Polder equations are applied, one is with an integrated winding employing Green and Sandy's

partially magnetized model and the last one is a wide-band circulator by stacking two circulators with different operating frequencies.

4.2 CPW on ferrite LTCC

4.2.1 Introduction

Since the ferrite LTCC technology is totally new to us, we start by design a simple CPW transmission line on it. The design of the CPW line is shown in Figure 4.1 and the fabricated one in Figure 4.2. Five layers are used and the total size (L*W*H) is 15mm*4.79mm*0.55mm. Simulations under different dc bias fields are performed to demonstrate the resonance frequencies in terms of the applied field. The measurements are performed with an external electromagnet. The CPW transmission line follows the axis \vec{x} . The two ends of the CPW are connected to the probe station, while the electromagnet is placed in \vec{y} direction, therefore the device is biased transversely as shown in Figure 4.3.

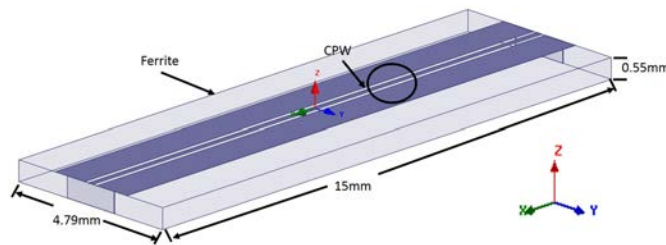


Figure 4.1: Design of a CPW on ferrite LTCC

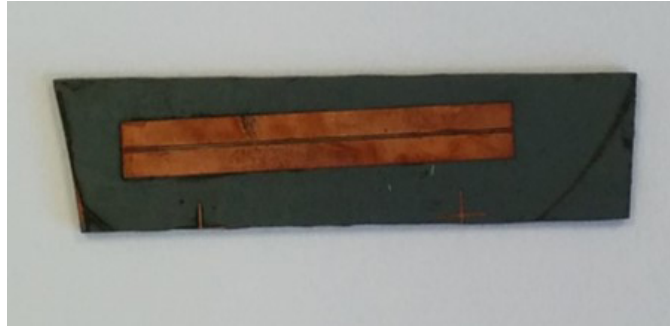


Figure 4.2: Photo of a fabricated CPW on ferrite LTCC

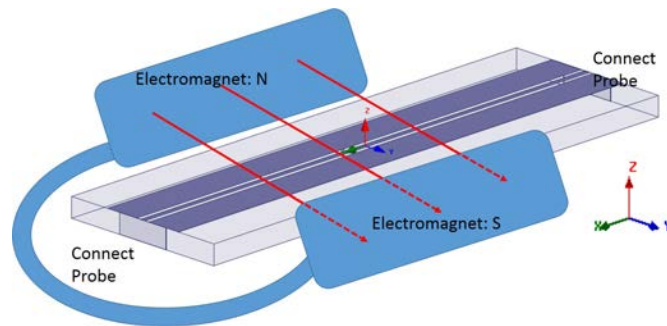


Figure 4.3: Measurement configuration of the CPW with an external electromagnet

4.2.2 Demagnetized ferrite $H_i = 0$

When the ferrite LTCC is totally demagnetized, there is a low field loss below 10 GHz according to the characterization in [15]. The measurement performed by Dr. Didier Vincent confirms this loss as shown in Figure 4.4.

However, the simulator HFSS cannot predict it. Figure 4.5 shows a perfect transmission in HFSS because it considers the demagnetized ferrite as a dielectric material ($M_s = 0$, $M=0$ and $H_i = 0$).

4.2.3 Ferrite biased transversely

When the ferrite is biased in \vec{y} direction, the non-reciprocity could be observed. Figures 4.6a and 4.6b show the comparison of simulated and measured S-parameters

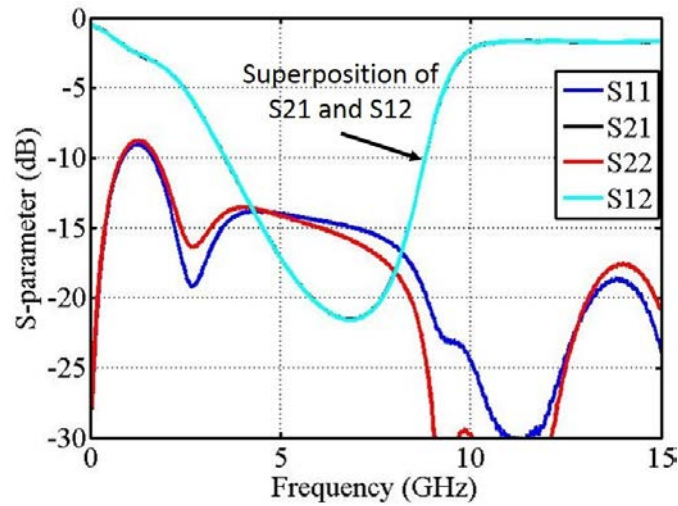


Figure 4.4: Measured S-parameters when ferrite is totally demagnetized

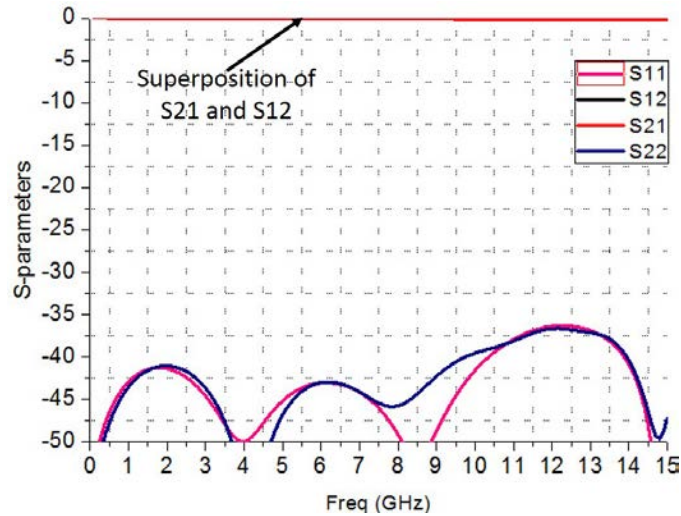


Figure 4.5: Simulated S-parameters when ferrite is totally demagnetized

when the ferrite is biased transversely with an internal magnetic field $H_i = 52 \text{ kA/m}$ (660 Oe). A magnetometer is used to measure the dc bias field near the CPW transmission line. Since a tangential bias is applied, the demagnetization factor is weak and negligible. In general, the simulated S-parameters meet the measured ones, except that the measured resonance frequency is 1.5 GHz lower than the simulated one. This is probably due to the non-uniform magnetic bias fields hence the inaccurate

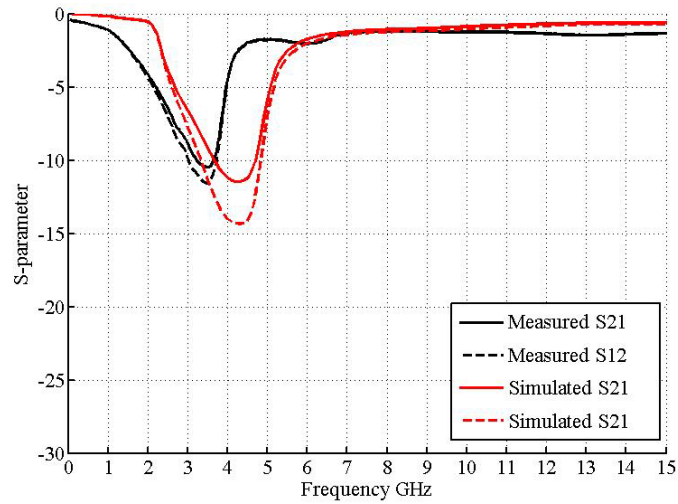


Figure 4.6a: Comparison of S21 and S12 between simulation and measurement when ferrite is biased transversely with internal magnetic field $H_i=660$ Oe

measurements by the magnetometer.

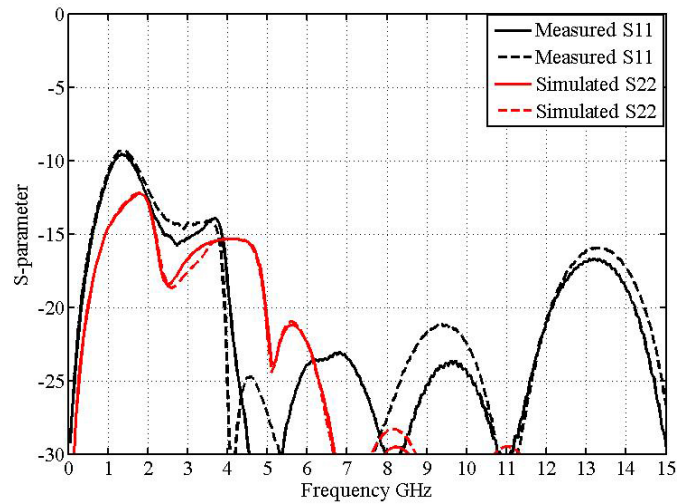


Figure 4.6b: Comparison of S11 and S22 between simulation and measurement when ferrite is biased transversely with internal magnetic field $H_i=660$ Oe

4.2.4 Prototype of a tunable attenuator

Since the demagnetization factors could be ignored when the device is transversely biased, so, according to Kittel's equation, the resonance frequency could be found by

Equation (4.1), where H_a is the applied dc field.

$$f_r = \frac{\mu_0 \gamma}{2\pi} \sqrt{H_a (H_a + M_s)} \quad (4.1)$$

Figure 4.7 shows that the measured resonance frequency depends on the applied field. We then compare the measured resonance frequencies with the calculated ones, as shown in Figure 4.8. Although there is a difference of 1.5 GHz as we explained before, generally they are in agreement.

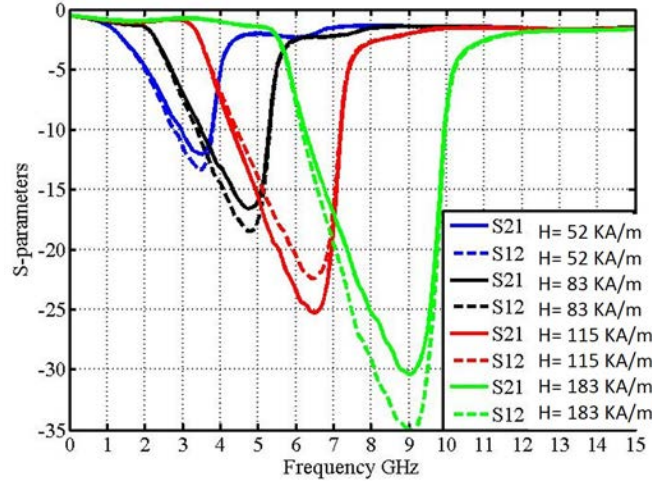


Figure 4.7: Measured resonance frequencies under different bias fields

Based on the theory and the measurements, a prototype of a tunable attenuator could be achieved by varying the transversal bias field. Considering that the ferrite LTCC technology allows 3D design, several windings in series (see Figure 4.9) could be integrated into the CPW structure to provide the internal bias field (without demagnetization field). This design could achieve a multi-functional attenuator: 1. the attenuation frequency could be tuned by changing the dc current which varies the internal magnetization M ; 2. the attenuation level could also be controlled by choosing the number of energized windings.

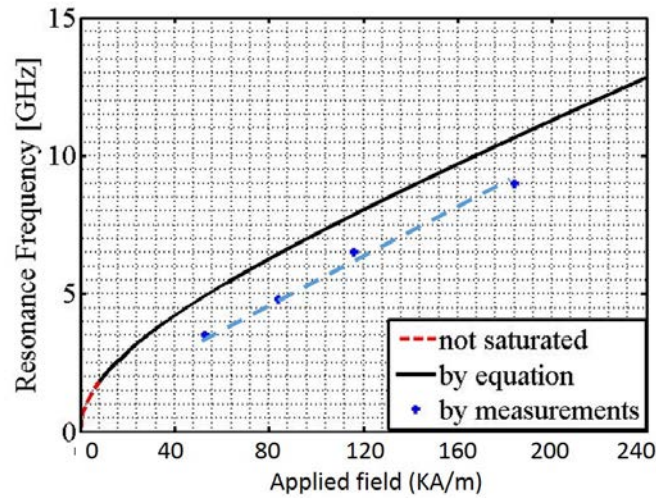


Figure 4.8: Comparison of measured and calculated resonance frequencies under different bias fields

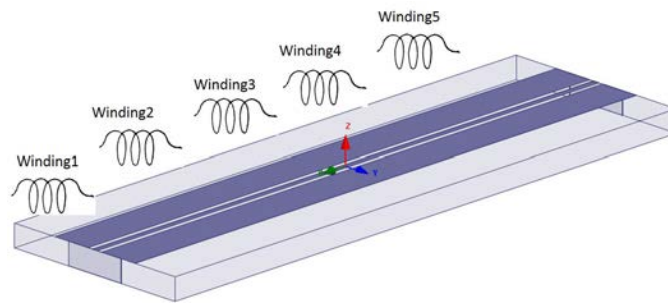


Figure 4.9: Prototype of a tunable attenuator with windings in series

This design is not in the scope of the thesis. However, the simulations and measurements of the ferrite LTCC CPW transmission line allow us to have a first experience in designing ferrite LTCC device.

4.3 Different structures of circulators

After having designed and measured the CPW based on ferrite LTCC, we will present some structures of circulators in theories, especially the stripline structure which is used in our final designs.

4.3.1 Stripline circulator

The conventional stripline circulator is shown in Figure 4.10 [5]. It consists of two metal grounds, a center conductor and two ferrite disks. This is a symmetrical structure. Two ferrite discs are separated by the center conductor and three access transmission lines are spaced 120° from each other. Two ground planes then envelop the structure. The space surrounding the ferrite discs is occupied by dielectric materials. The ferrite material is magnetized perpendicularly to the plane of the disk by an external static magnetic field created by two magnets located on either side of the structure.

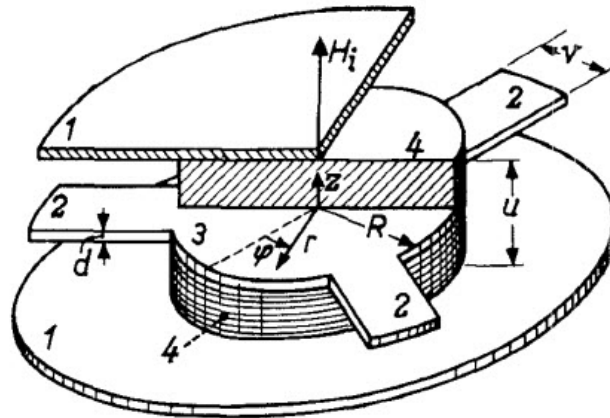


Figure 4.10: Principle construction of a stripline junction circulator: (1) two metal grounds; (2,3) center conductor; (4) ferrite disk; (5) V is the coupling angle; (6) u is the height of the ferrite disk; (7) H_i is the bias field; (8) d is the thickness of conductors; (9) R radius of the center conductor [5]

The possibility of a three-port circulator was firstly postulated by Carlin [100] in 1954 based on the scattering-matrix analysis of the three-port microwave junction. The performance of an early experimental circulator (using waveguide) was described by Chait and Curry [101] in 1959. Since then, various types of circulators: stripline circulators [102–105], three-port ring circulators [106] and other types [107] have

been developed. The operating bands extend from the microwave to the millimeter range [108].

A stripline structure was chosen in this thesis because the two broad metal ground planes allow the bias windings to be placed immediately above and below the circulator core without coupling to the microwave fields. Hence the ground planes provide rf shielding while simultaneously allowing the magnetostatic bias field into the core.

4.3.2 Microstrip circulator

Microstrip line was firstly developed in ITT laboratories [109] and was a competitor of stripline. Now the microstrip line is one of the most popular types of planar transmission lines, primarily because it can be fabricated by photo-lithographic process and easily integrated with other passive and active microwave devices. These make microstrip circulators preferable in some circuit designs because it would provide an ideal compact circuit, compared to (stripline) triplate circulators or waveguide circulators. Conventionally, a Y-junction microstrip circulator consists of a dielectric substrate and a ferrite material which is put on it. A metal ground is located below the dielectric material. Finally, the center conductor of the circulator is designed on the top of the structure (see Figure 4.11 [17]). In some cases, the ferrite disk could also be placed above the center conductor.

The first reported microstrip circulator operating at 8.3 GHz was realized by Hershonov, B. in 1966 [110]. Then another 3-port microstrip circulator was built in 1971 which operates near 30 GHz with an isolation greater than 20 dB and a fractional bandwidth about 6% [111]. Recently, researchers are able to design microstrip circulators using LTCC technology [24]. Besides, thin ferrite film is also used to design a microstrip circulator [112]. Moreover, by depositing barium ferrite films on sapphire

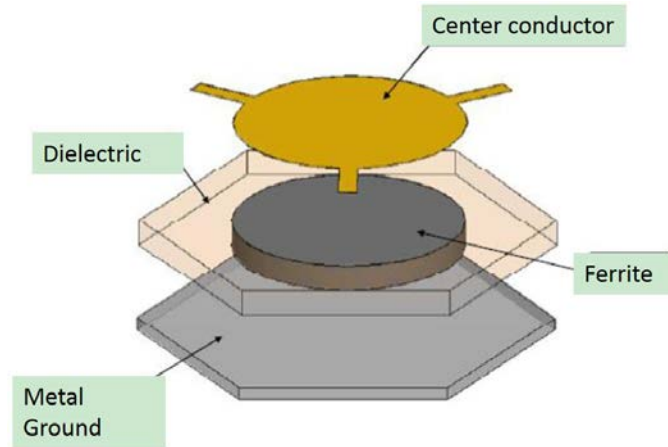


Figure 4.11: Principle construction of a microstrip junction circulator [17]

substrate, a self-biased microstrip junction circulator at 26 GHz was realized [113] in 2011 which allows the integration of ferrite passive nonreciprocal components with monolithic microwave integrated-circuit (MMIC) devices.

4.3.3 Coplanar circulator

A circulator with coplanar waveguide (CPW) structure is also a good candidate for microwave integrated circuits because the transmission line (signal) and the metal grounds (GND) are located in the same plane (usually on the top). Thus, coplanar circulators can be easily fabricated at a low cost by using lithography process. Figure 4.12 [18] shows a typical coplanar structure of a hexagonal circulator with CPW structure.

Wen and Bayard have firstly reported coplanar circulators operating at 7 GHz which need an internal magnetic field greater than 170 kA/m [114, 115]. Then Ogasawara reported that Y-junction circulators with a CPW could successfully operate at different frequencies according to different external dc magnetic fields applied perpendicularly to the ferrite surface [116]. Recently a CPW circulator including BaM

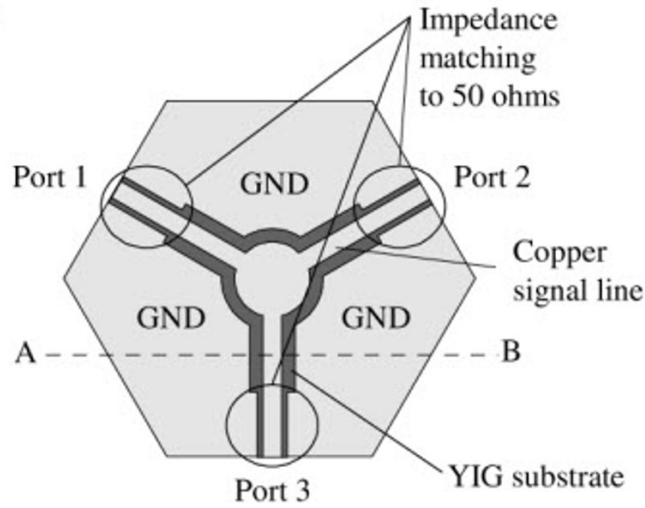


Figure 4.12: Top view of the signal line and the ground plane of a hexagonal circulator with CPW structure [18]

(Barium ferrite) thin films and dielectric layer with a low dielectric constant is also proposed and simulated in [117]. In 2011, a ferrite was formed by embedding magnetic particles into a host dielectric matrix in laboratory LT2C and a coplanar circulator was fabricated based on it [118].

4.4 Theory of stripline junction circulators

As presented before, the design of a stripline Y-junction circulator (see Figure 4.13) is generally based on the work of Bosma [5] who solves the simplified boundary-value problem of the circulator ferrite disk by using a Green function approach. Then Fay and Comstock [38] describe the operation of a circulator in terms of counter-rotating propagation modes in the ferrite disk. Wu and Rosenbaum [39] predict octave bandwidth microstrip circulator operation theoretically using Bosma's Green function analysis. The Green function relates E_z and H_ϕ for lossless circulators when the effective permeability $\mu_{eff} > 0$. Assuming $e^{j\omega t}$ harmonic time dependence,

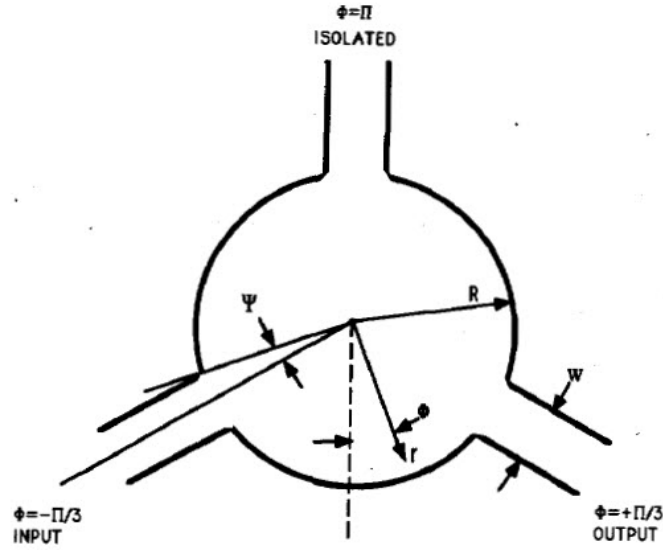


Figure 4.13: Circulator coordinate reference

Bosma's Green function has the following form (see Equation (4.2)):

$$G(r, \phi; R, \phi') = -\frac{jZ_{eff}J_0(kr)}{2\pi J'_0(x)} + \frac{Z_{eff}}{\pi} \sum_{n=1}^{\infty} \frac{\frac{k n J_n(x)}{\mu x} \sin n(\phi - \phi') - jJ'_n(x) \cos n(\phi - \phi')}{\{J'_n(x)\}^2 - \left\{\frac{k n J_n(x)}{\mu x}\right\}^2} \times J_n(kr) \quad (4.2)$$

where:

- κ and μ : Polder tensor elements
- $J_n(x)$: Bessel function of the first kind with order n
- x : $x=kR$
- k : the propagation constant $k = \omega\sqrt{\epsilon_0\mu_0\epsilon_f\mu_{eff}}$
- R : ferrite disk radius

- ω : circulator's operating frequency
- ϵ_0 : permittivity of free-space $\epsilon_0 = 8.854 \times 10^{-12}$
- ϵ_f : relative permittivity of ferrite
- ϵ_d : relative permittivity of dielectric around ferrite
- μ_{eff} : effective permeability of ferrite $\mu_{eff} = \frac{\mu^2 - \kappa^2}{\mu}$
- $J'_n(x)$: derivative of Bessel function $J_n(x)$ with respect to its argument
- Z_d : impedance of the dielectric material
- Z_{eff} : intrinsic wave impedance of ferrite $Z_{eff} = \sqrt{\frac{\mu_0 \mu_{eff}}{\epsilon_0 \epsilon_f}}$

The roots of $J'_n(x) = 0$ are shown in Equation (4.3), where x_{nm} means that the m^{th} order root of $J'_n(x) = 0$.

$$\left\{ \begin{array}{l} x_{11} = 1.841 \\ x_{21} = 3.054 \\ x_{31} = 4.201 \\ x_{12} = 5.331 \end{array} \right. \quad (4.3)$$

However, not all terms are important in practical applications and most circulators operate close to the $n=1$ resonance, so many people consider only the $n=1$ term leading to the formula of the radius R of the ferrite disk (Equation (4.4a)) and the coupling angle Φ (Equation (4.4b)), where Z_d is the wave impedance of the dielectric around the ferrite disk ($Z_d = \frac{120\pi}{\sqrt{\epsilon_d}}$).

$$kR = x_{11} = 1.841 \quad (4.4a)$$

$$\Phi = \frac{\pi}{\sqrt{3}(1.84)} \frac{Z_d}{Z_{eff}} \left| \frac{\kappa}{\mu} \right| \quad (4.4b)$$

Since there are no radial currents at the edge of the ferrite disks except at the three access ports (neglecting fringing), Bosma, Davies and Cohen [119], and others suggest the following boundary condition for the three-port Y-junction circulator (Equation (4.5)):

$$H_\phi(R, \Phi) = \begin{cases} H_1, & -\frac{\pi}{3} - \Psi < \phi < -\frac{\pi}{3} + \Psi \\ H_2, & \frac{\pi}{3} - \Psi < \phi < \frac{\pi}{3} + \Psi \\ H_3, & \pi - \Psi < \phi < \pi + \Psi \\ 0, & \text{elsewhere} \end{cases} \quad (4.5)$$

Equation (4.6) is also employed according to the cyclic symmetry:

$$G\left(\phi + \frac{2\pi}{3}; \phi' + \frac{2\pi}{3}\right) = G(\phi; \phi') \quad (4.6)$$

Since the circulator is symmetrical, the impedance matrix is therefore defined by Equation (4.7).

$$[\eta] = \begin{bmatrix} \eta_{11} & \eta_{31} & \eta_{21} \\ \eta_{21} & \eta_{11} & \eta_{31} \\ \eta_{31} & \eta_{21} & \eta_{11} \end{bmatrix} \quad (4.7)$$

The electric field on any port at the observation point due to a distribution of unit point source is given by the superposition integral (Equation (4.8)) [63]:

$$E_z(R, \phi) = \int_c G(\phi|\phi') H_\phi(R, \phi') d\phi' \quad (4.8)$$

Then the impedance at each port could be derived (Equation (4.9)) because the magnetic field H_Φ is constant at each port according to the boundary condition:

$$\eta = \frac{E_z}{H_\Phi} = \int_c G(\phi|\phi_0) d\phi \quad (4.9)$$

The observation point is assumed to be $\phi_0 = -\pi/3$ in this calculation, then the wave impedance at port 1 is (Equations (4.10a) and (4.10b)):

$$\eta_{11} = \int G\left(\phi \middle| -\frac{\pi}{3}\right) d\phi \quad -\frac{\pi}{3} - \Psi < \phi < -\frac{\pi}{3} + \Psi \quad (4.10a)$$

$$\begin{aligned} \eta_{11} &= - \int_{-\frac{\pi}{3}-\Psi}^{-\frac{\pi}{3}+\Psi} \frac{jZ_{eff}J_0(kr)}{2\pi J'_0(x)} d\phi + \\ &\int_{-\frac{\pi}{3}-\Psi}^{-\frac{\pi}{3}+\Psi} \frac{Z_{eff}}{\pi} \sum_{n=1}^{\infty} \frac{\frac{k n J_n(x)}{\mu x} \sin n\left(\phi + \frac{\pi}{3}\right) - jJ'_n(x) \cos n\left(\phi + \frac{\pi}{3}\right)}{\{J'_n(x)\}^2 - \left\{\frac{k n J_n(x)}{\mu x}\right\}^2} \times J_n(kr) d\phi \\ &= - \frac{jZ_{eff}J_0(kr)}{2\pi J'_0(x)} \times (2\Psi) + \\ &\frac{Z_{eff}}{\pi} \sum_{n=1}^{\infty} \frac{-j2J'_n(x) \Psi \text{sinc}(n\Psi)}{\{J'_n(x)\}^2 - \left\{\frac{k n J_n(x)}{\mu x}\right\}^2} \times J_n(kr) \end{aligned} \quad (4.10b)$$

where $\text{sinc}(n\Psi) = \frac{\sin(n\Psi)}{n\Psi}$

Similarly, the impedance at port 2 and port 3 can be derived in Equation (4.11b) and Equation (4.12b), respectively.

$$\eta_{21} = \int G\left(\phi \middle| -\frac{\pi}{3}\right) d\phi \quad \frac{\pi}{3} - \Psi < \phi < \frac{\pi}{3} + \Psi \quad (4.11a)$$

$$\begin{aligned}
\eta_{21} &= - \int_{\frac{\pi}{3}-\Psi}^{\frac{\pi}{3}+\Psi} \frac{jZ_{eff}J_0(kr)}{2\pi J'_0(x)} d\phi + \\
&\int_{\frac{\pi}{3}-\Psi}^{\frac{\pi}{3}+\Psi} \frac{Z_{eff}}{\pi} \sum_{n=1}^{\infty} \frac{\frac{k n J_n(x)}{\mu x} \sin n \left(\phi + \frac{\pi}{3} \right) - j J'_n(x) \cos n \left(\phi + \frac{\pi}{3} \right)}{\{J'_n(x)\}^2 - \left\{ \frac{k n J_n(x)}{\mu x} \right\}^2} \times J_n(kr) d\phi \\
&= - \frac{jZ_{eff}J_0(kr)}{2\pi J'_0(x)} \times (2\Psi) + \\
&\frac{Z_{eff}}{\pi} \sum_{n=1}^{\infty} \frac{2\Psi \text{sinc}(n\Phi) \left[\frac{\kappa n J_n(x)}{\mu x} \sin \frac{2n\pi}{3} - i J'_n(x) \cos \frac{2n\pi}{3} \right]}{\{J'_n(x)\}^2 - \left\{ \frac{k n J_n(x)}{\mu x} \right\}^2} \times J_n(kr)
\end{aligned} \tag{4.11b}$$

$$\eta_{31} = \int G \left(\phi - \frac{\pi}{3} \right) d\phi \quad \pi - \Psi < \phi < \pi + \Psi \tag{4.12a}$$

$$\begin{aligned}
\eta_{31} &= - \int_{\pi-\Psi}^{\pi+\Psi} \frac{jZ_{eff}J_0(kr)}{2\pi J'_0(x)} d\phi + \\
&\int_{\pi-\Psi}^{\pi+\Psi} \frac{Z_{eff}}{\pi} \sum_{n=1}^{\infty} \frac{\frac{k n J_n(x)}{\mu x} \sin n \left(\phi + \frac{\pi}{3} \right) - j J'_n(x) \cos n \left(\phi + \frac{\pi}{3} \right)}{\{J'_n(x)\}^2 - \left\{ \frac{k n J_n(x)}{\mu x} \right\}^2} \times J_n(kr) d\phi \\
&= - \frac{jZ_{eff}J_0(kr)}{2\pi J'_0(x)} \times (2\Psi) + \\
&\frac{Z_{eff}}{\pi} \sum_{n=1}^{\infty} \frac{2\Psi \text{sinc}(n\Phi) \left[\frac{\kappa n J_n(x)}{\mu x} \sin \frac{4n\pi}{3} - i J'_n(x) \cos \frac{4n\pi}{3} \right]}{\{J'_n(x)\}^2 - \left\{ \frac{k n J_n(x)}{\mu x} \right\}^2} \times J_n(kr)
\end{aligned} \tag{4.12b}$$

Now, we have all elements of the impedance matrix (Equation (4.7)). We then normalize the impedance $[\eta]$ by the dielectric impedance Z_d leading to $[Z]=[\eta]/Z_d$. The next step is to transform the matrix $[Z]$ to matrix $[S]$, by $[S] = [Z + I]^{-1}[Z + I]$, where $[I]$ is identity matrix. Then the elements of $[S]$ could be obtained by Equations (4.13a)

to (4.13c).

$$S_{11} = 1 + \frac{-2Z_d[(Z_{11}^2 + 1) - Z_{21}Z_{31}]}{(Z_{11} + 1)^3 + Z_{21}^3 + Z_{31}^3 - 3Z_{21}Z_{31}(Z_{11} + 1)} \quad (4.13a)$$

$$S_{21} = \frac{-2Z_d[Z_{31}^2 - Z_{21}(Z_{11} + 1)]}{(Z_{11} + 1)^3 + Z_{21}^3 + Z_{31}^3 - 3Z_{21}Z_{31}(Z_{11} + 1)} \quad (4.13b)$$

$$S_{31} = \frac{-2Z_d[Z_{21}^2 - Z_{31}(Z_{11} + 1)]}{(Z_{11} + 1)^3 + Z_{21}^3 + Z_{31}^3 - 3Z_{21}Z_{31}(Z_{11} + 1)} \quad (4.13c)$$

To simplify the expression of these S-parameters, three variables are defined by the Equations (4.14a) to (4.14c):

$$C_1 = j\pi \frac{Z_{11} + 1}{2Z_{eff}} \quad (4.14a)$$

$$C_2 = j\pi \frac{Z_{31}}{2Z_{eff}} \quad (4.14b)$$

$$C_3 = j\pi \frac{Z_{21}}{2Z_{eff}} \quad (4.14c)$$

Hence the elements of [S] (Equations (4.13a) to (4.13c)) can be rewritten in Equations (4.15a), (4.15b) and (4.15c)

$$S_{11} = 1 + \frac{\pi Z_d}{jZ_{eff}} \frac{C_1^2 - C_2C_3}{C_1^3 + C_2^3 + C_3^3 - 3C_1C_2C_3} \quad (4.15a)$$

$$S_{21} = \frac{\pi Z_d}{jZ_{eff}} \frac{C_2^2 - C_1C_3}{C_1^3 + C_2^3 + C_3^3 - 3C_1C_2C_3} \quad (4.15b)$$

$$S_{31} = \frac{\pi Z_d}{jZ_{eff}} \frac{C_3^2 - C_1C_2}{C_1^3 + C_2^3 + C_3^3 - 3C_1C_2C_3} \quad (4.15c)$$

Finally we can get the matrix [S] (see Equation (4.16)) which is in agreement with that in article [120]. For more details of these calculations, please refer to the Appendix A.

$$[S] = \begin{bmatrix} S_{11} & S_{31} & S_{21} \\ S_{21} & S_{11} & S_{31} \\ S_{31} & S_{21} & S_{11} \end{bmatrix} \quad (4.16)$$

A Matlab program is realized based on the above calculations which allows to simulate a circulator mathematically. This is very useful in designing circulators, because this program could give us approximate values of some important parameters such as the radius of ferrite disk, operating frequency, coupling angle, bias field etc, which could be used in the optimization by the EM simulator.

4.5 Ferrite LTCC circulator with external magnet

In order to verify the feasibility of a circulator based on ferrite LTCC technology, a stripline circulator with external magnets is firstly designed, fabricated and measured.

4.5.1 Theory and design

Since the entire volume in this design is ferrite LTCC material, the magnetic wall in Bosma's theory cannot be well defined, so the edge-guided mode structure is chosen. As said before, the edge-guided mode circulator has a potential broadband performance [59] [60]. The edge-guided mode is based on Hine's studies of the edge-guided-wave (EGW) propagation in microwave integrated circuits. The effect of field displacement concentrates the electromagnetic (EM) field on one edge of the stripline for one propagation direction and on the other for the reverse direction.

Although the circulator designed here is an edge-guided mode circulator, the theory of Bosma based on the volume resonance is still useful to predict approximately

the circulator's performance. The analytical Matlab program mentioned in the previous section is employed for this purpose. This program contains two parts: one part to calculate the Polder tensor (μ , κ and μ_z); the other part to calculate Z-parameters and then convert them to S-parameters. As explained, the theory of this calculation has been already presented in the following references [39] [120]. The inputs of this Matlab program are the basic parameters concerning the materials and circulator, such as: relative permittivity of the dielectric ϵ_d , relative permittivity of the ferrite ϵ_f , magnetic saturation of the ferrite M_s , internal H field H_i , damping factor α , circulator's operating frequency f_c , number of modes to be taken into account N, frequency range and step, etc

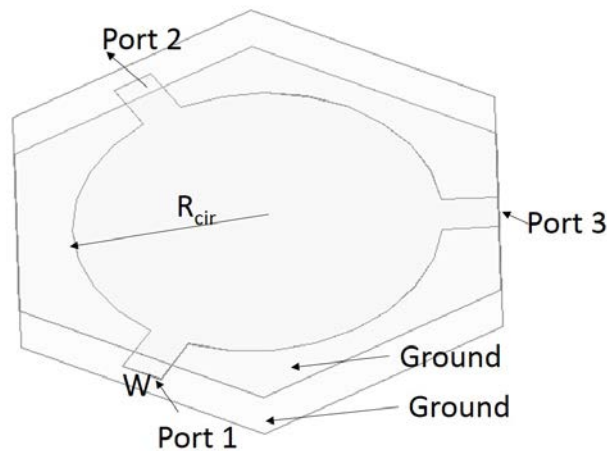


Figure 4.14: Stripline circulator configuration

With these parameters, the Matlab program is able to calculate the circulator's width W and the radius R_{cir} (see Figure 4.14) and then S-parameters could be shown with three curves in dB: transmission S_{31} , isolation S_{21} and reflection S_{11} . Figure 4.15 indicates a possible circulation in Matlab at 15 GHz with $R_{cir}=3$ mm and $W=0.4$ mm. If the approximation based on the Bosma's theory (Equations (4.4a) and (4.4b) [39]) is not good, the width W and R_{cir} could also be entered manually,

which allows us to apply an improved approximation.

The problem of this mathematical approximation is that the height of the model cannot be considered, so an EM simulator is still necessary to finalize the design by optimizing the previous parameters found by the analytical program.

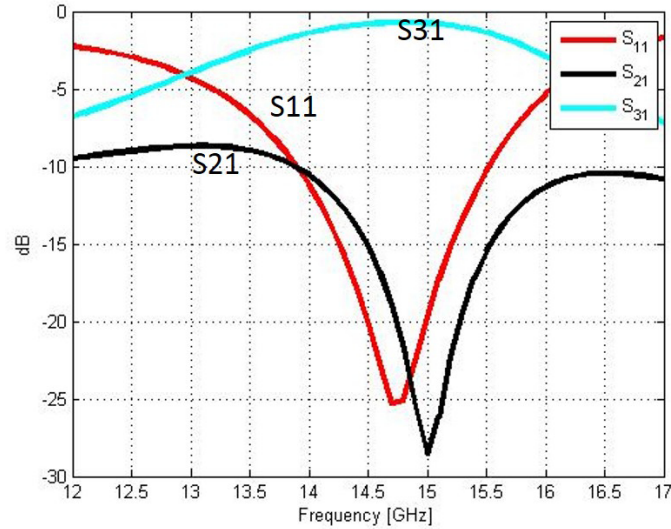


Figure 4.15: Calculated S-parameters in Matlab

An edge-guided circulator is then designed in Ansys HFSS. The theories about edge-guided circulators with three ports are presented in [59,60]. The key parameters are the radius R which gives the curvature (see Figure 4.16) and the width W which is the open width of the center conductor. These parameters must be determined according to the operating frequency and the material's properties. Furthermore, the two metal grounds are placed on the layer above the center conductor and the layer below. By optimizing the W , R and R_{cir} , the operating frequency is fixed to 15 GHz to avoid low-field losses. The next difficulty consists in the transition from CPW (on the top layer) to stripline (circulator). Three CPW transmission lines are designed on the top layer and the lower ground plane of the circulator is designed to have three hands to connect the vias from the top layer (see Figure 4.17). Then,

each ground of one CPW transmission line is connected to both ground planes of the circulator by two vias: one goes down to the upper ground, the other goes to the lower one, finally the CPW line's signal conductor is connected to the circulator's center conductor. The reason why all the metal grounds are connected is to avoid exciting a parallel-plate mode.

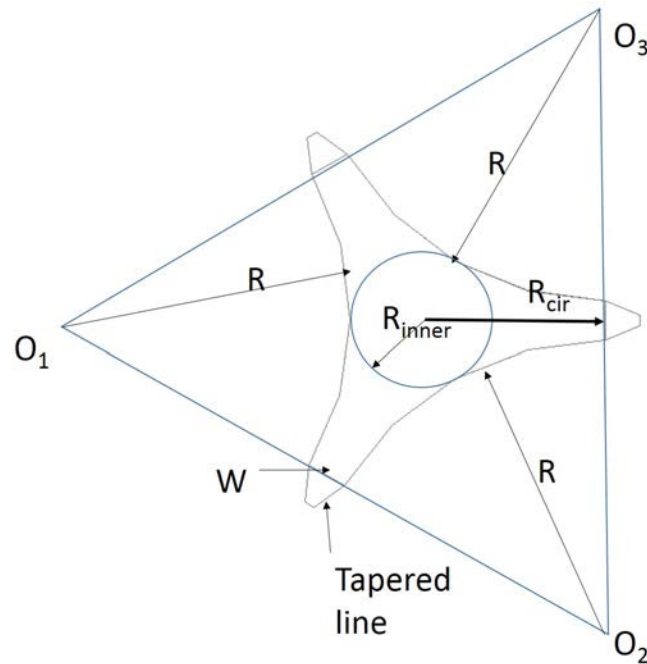


Figure 4.16: Parameters of an edge-guided circulator

The optimization is performed using Ansoft HFSS software and leads to the final dimensions $R_{cir}=2.8$ mm, $W=0.38$ mm (see Figure 4.17), the magnetic-biased area has a diameter of 1 mm and the internal H-field is close to 120 kA/m which is much smaller than the one given in reference [24]. The simulation result, shown in Figure 4.18, meets that of Matlab: transmission -0.84 dB, isolation -29 dB and the reflection approximately -19 dB. The operating frequency is 14 GHz from HFSS instead of 15 GHz predicted by the analytical program. This is probably due to: 1. the Matlab program performs only a 2D mathematical analysis; 2. The 3D model in

HFSS is an edge-guide mode circulator. One CPW transmission line is also fabricated to serve the network analyzer calibration.

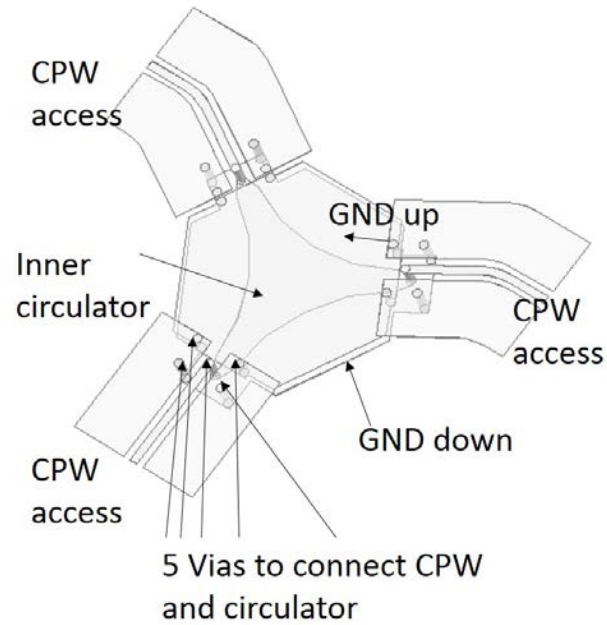


Figure 4.17: Edge-guided circulator's 3D design

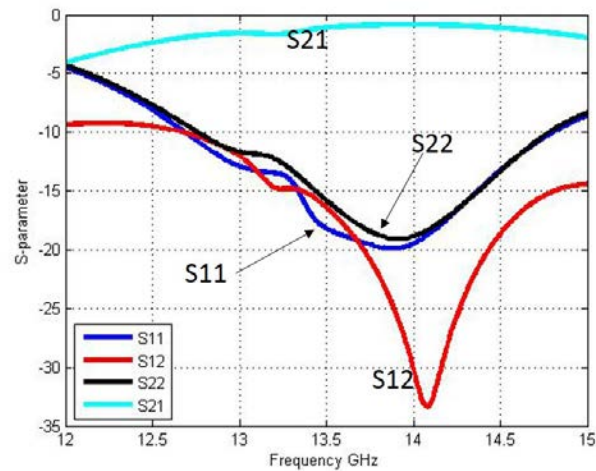


Figure 4.18: Simulated S-parameters in HFSS when port 3 is matched: a circulator working at 15 GHz

4.5.2 Measurement

The LTCC edge-guided circulator is then fabricated. For the probe station, the angle between two adjacent ports is 90° , so two of the CPW feed lines contain small bends to accommodate the probe station and care is taken to ensure that these bends do not cause reflections at 15 GHz. The measurement of the CPW line is shown in Figure 4.19, which shows that the performance of the unbiased LTCC material is good between 10 GHz and 17 GHz. As predicted [121], the attenuation is indeed strong below 10 GHz due to the low-field losses as explained in the previous chapter.

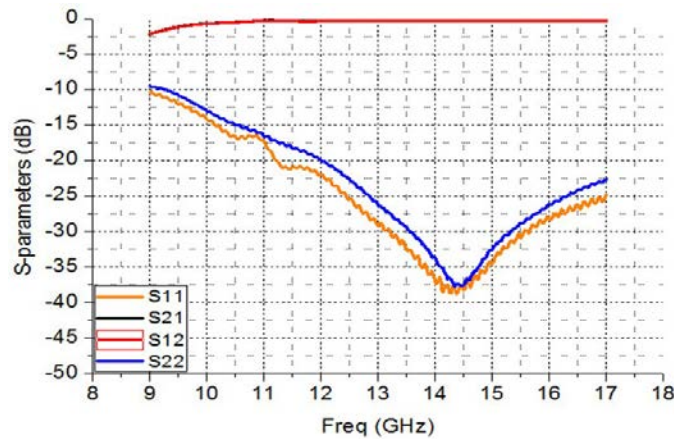


Figure 4.19: The measurement of the CPW verifies the calibration and demonstrates that the loss below 10 GHz is strong

We connect the port 3 of the circulator to a matched load and then the circulator is measured. The internal magnetic field bias is obtained by applying a carefully chosen external magnet with a surface field 5233 Gauss on the top layer of the substrate. The bias magnetized area diameter is 1.59 mm which is larger than the diameter (1 mm) predicted by HFSS. The measurement of the circulators is performed with a two-port network analyzer, with the third port (North) being matched (50Ω). The measured transmission and isolation is approximately -1.8 dB and -20 dB respectively as shown in Figure 4.20. The measurement also shows that the operating frequency is about

15 GHz and at this center frequency, the return loss is better than 20 dB. An internal resonance is also observed from the transmission parameter (S_{21}) at approximately 15.5 GHz. This is perhaps due to the placement of the metallized magnet on the top layer coupling with the rf field. Since the whole volume is ferrite material, the magnets could probably only saturate the center leading to other parts partially magnetized, which is likely the cause of the higher than expected insertion loss. Although a small magnet is desired in this work, the insertion loss could be improved by using a larger and more powerful magnet.

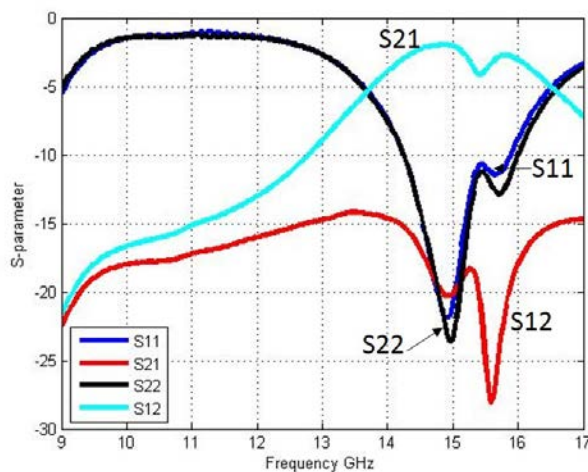


Figure 4.20: The measurement of the circulator shows the working frequency is 15 GHz

4.6 Ferrite LTCC circulator with integrated winding

The above design demonstrates that circulators could be designed on the ferrite LTCC substrate. In order to remove the bulky external magnet and avoid the demagnetization factor, in this section, a circulator with an integrated winding using the same

ferrite LTCC tape will be presented.

4.6.1 Bias winding design

It would be best if the winding could provide a uniform and perpendicular (z -direction) magnetostatic bias field in the circulator core, generating a wide range of magnetization value in the ferrite LTCC. The hexagonal planar coil is chosen for this purpose, because it approaches a circular coil which has the maximum area for a given radius.

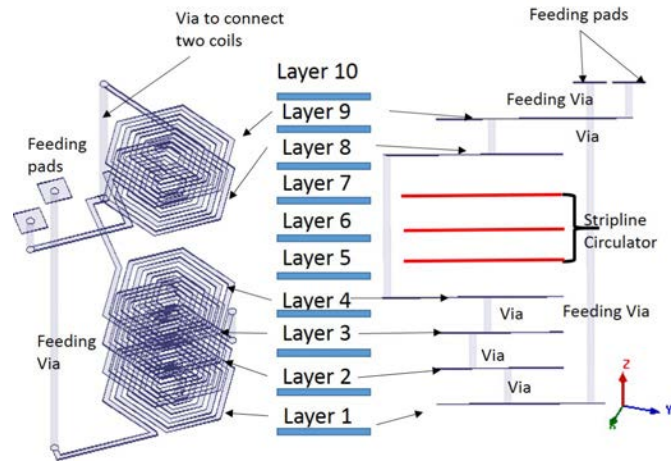


Figure 4.21a: The dc winding consists of 4 coils below the circulator and 2 coils above it

As shown in Figure 4.21a, the space priority is given to the winding. Stripline circulator only occupies three layers (5-7) and the top layer is reserved for connections, therefore, all the other layers are used to design the winding. The winding consists of four coils below the circulator on layer 1-4 and two coils above the circulator on layer 8 and 9. The 2D coil design is shown in Figure 4.21b. Each coil consists of 5 turns of a 0.1-mm wide conductor with a 0.1-mm spacing: both are the minimum values allowed in the fabrication process. The inner coil turn has a side-to-side width of 0.4

mm whereas the outer turn has a side-to-side width of 2.2 mm. The reason why we don't use the conception which has three coils below the circulator and three coils above the circulator is that the circulator's metal ground will block the interconnection via between the upper coils and lower coils. Therefore the number of the coils should be even in our case.

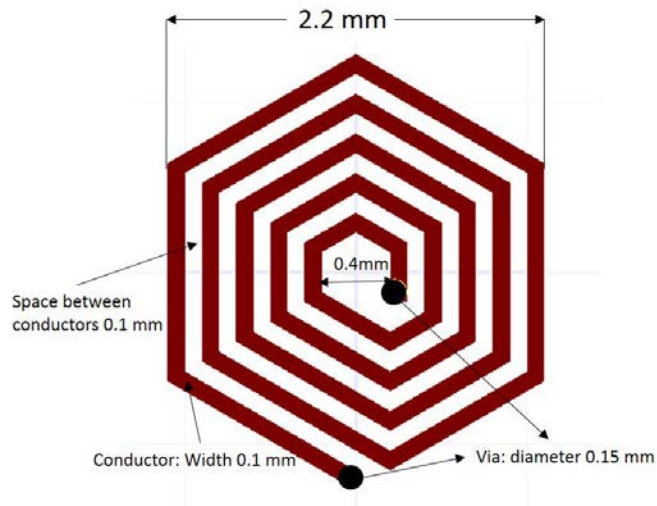


Figure 4.21b: Hexagonal coil dimensions

Current in the winding is supplied by two top-layer dc pads and 150- μm diameter vias are used to connect the coils as shown in Figure 4.21a. The current returns to the top layer from the bottom layer through a stacked via that is placed beside the hexagonal ground planes of the circulator. Figure 4.21c demonstrates the desired 2-D conceptual sketch of the biasing magnetic flux.

Magnetostatic simulation by Ansys Maxwell 3D

The magnetostatic simulation is performed with Ansys Maxwell 3D by putting the winding into a block of ferrite LTCC that has the same dimensions as the anticipated diced prototypes. The B-H curve of the ESL 40012 material is used for this simulation

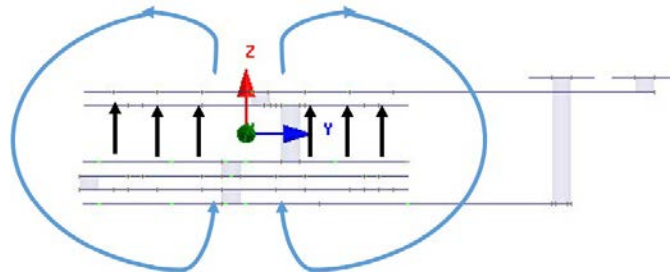


Figure 4.21c: 2D conceptual sketch of the biasing magnetic flux

[27]. Figure 4.22a shows the strength of the internal magnetic field B_i along the z-axis in the middle of the winding (the dash cut line).

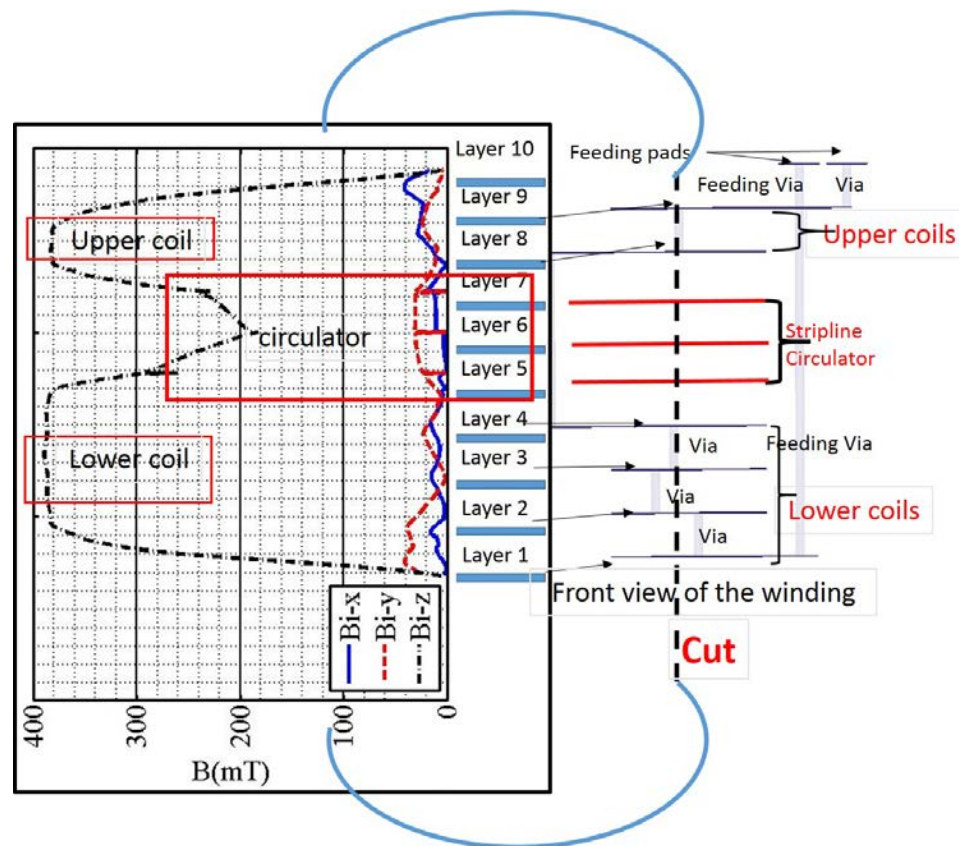


Figure 4.22a: Magneto-static simulation of winding in ferrite LTCC with a B-H curve: B_i along Z axis

The simulated dc magnetic field mainly follows the direction of z-axis which meets our expectation. Although high at the centre of the upper and lower coils, the Z

component of the internal field is only approximately 200 mT on the layer of the circulator when the applied current is 300 mA. Figure 4.22b shows the magnetic field strength on the layer of the circulator's center conductor. This plot indicates that the field follows z-axis for a radius ≤ 0.6 mm, and beyond that the field turns to the plane x-y.

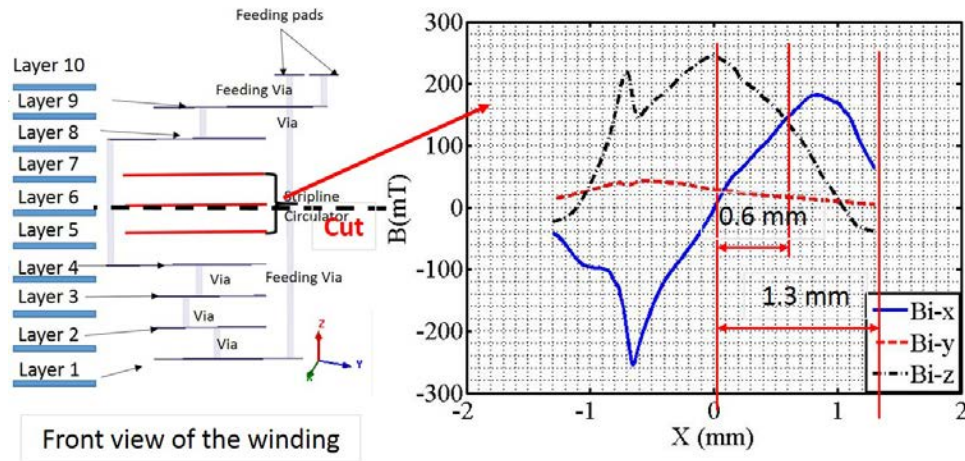


Figure 4.22b: Magneto-static simulation of winding in ferrite LTCC with a B-H curve: \mathbf{B}_i along X axis on layer 6 (circulator inner conductor)

The reason for the lower than expected z-polarized magnetostatic field in the core of the circulator has to do with the flux return paths inside the ferrite medium. The ferrite-air boundary represents a high reluctance path, whereas the lateral (xy) paths inside the ferrite present a much lower reluctance to the flux. As such, the magnetostatic field tends to create a closed dipole field around the upper and lower coils separately instead of producing a mutual z-directed flux path between the coils, where the circulator is located. Furthermore, the xy flux paths are quite thin and tend to saturate first, which further limits the magnetostatic flux in the core.

Figure 4.22c shows the strength of the internal magnetic field along the x-axis on layer 9. On this layer, most of the magnetic fields are in the xy-plane as we expect, and the strength is higher than 350 mT. In addition, the fields are strong near the

winding conductors and they are less uniform than that in the middle of the winding. This illustrates the challenges when windings are designed in a homogeneous ferrite medium. Although more outer turns could be added to the coils, they would not add significantly more bias field to the core because the z -component is inversely proportional to the square of the distance. Higher flux densities could be obtained by adding more LTCC layers, but this adversely impacts the fabrication cost. Higher flux densities could also be obtained by using more turns per unit area, but this would require thinner lines that would pose a risk of melting when biased by the current. Using thinner layers ($58 \mu\text{m}$) is another solution to get a higher flux densities [28], but the special fabrication process should be used. Hence the five turns coil represents a trade-off between the strength of the field created and the size of the coils.

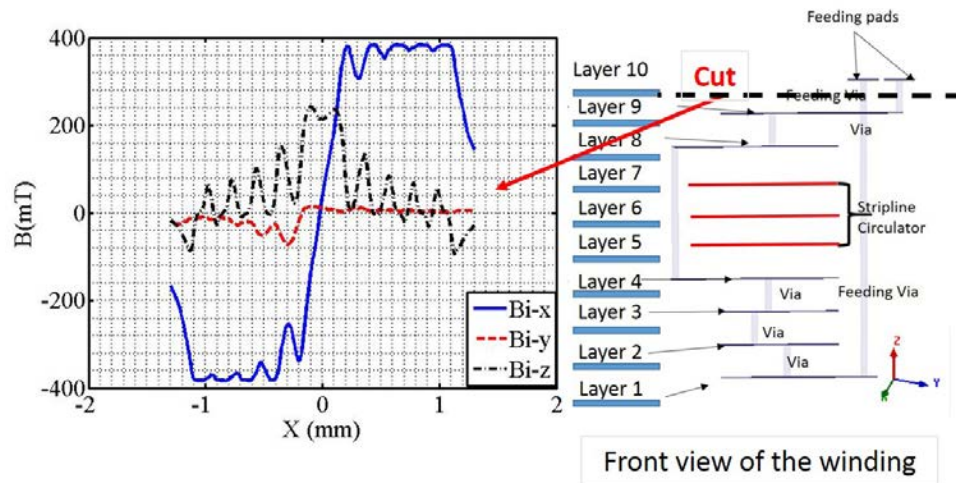


Figure 4.22c: Magneto-static simulation of winding in ferrite LTCC with a B-H curve: \mathbf{B}_i along X axis on layer 9

The magnetization values obtained from the magnetostatic simulations could be used to calculate the elements of the permeability tensor.

4.6.2 Y-junction edge-guided circulator design

The structure of the proposed circulator is shown in Figure 4.23. A stripline design is chosen specifically because the two broad metal ground planes allow the bias windings to be placed immediately above and below the circulator core without coupling to the microwave fields [5, 37]. Hence the ground planes provide rf shielding while simultaneously allowing the magnetostatic bias field into the core. The proposed circulator uses the edge-guided mode of operation because of its known broadband performance [59, 60, 122]. The design of the circulator uses 10 layers of ESL 40012 ferrite LTCC, in which each layer has a fired thickness of 110 μm . The magnetostatic and microwave (X-band) properties of this ferrite have already presented: a saturation magnetization $\mu_0 M_s = 400$ mT, a relative permittivity of $\epsilon_r = 14.6$, a loss tangent 4.24×10^{-3} . The damping factor α is found to be around 0.35 by measuring a CPW transmission line on ESL 40012 [94]. Hence the line width ΔH equals 250 Oe according to Equation (4.17) [9]. This material is lossy below 10 GHz due to the low-field losses, especially if it is totally demagnetized. The magnetization frequency is defined as $f_m = \gamma \mu_0 M_s$ (11.2 GHz), so an operating frequency of 14 GHz is chosen to avoid the low-field losses.

$$\Delta H = \frac{2\alpha\omega}{\mu_0\gamma} \quad (4.17)$$

According to the characterization of this ferrite LTCC [15], integrated windings could generate a field which is less than the M_s of the ferrite, leaving the material only partially magnetized. The theories of partially magnetized ferrites are given in [85, 86, 89, 91]. As we presented in the previous chapter, the model of Rado performs a spatial average of the domains in the ferrite [85]. For frequencies above the resonance, a good approximation for the extra-diagonal term κ is obtained but not for the diagonal

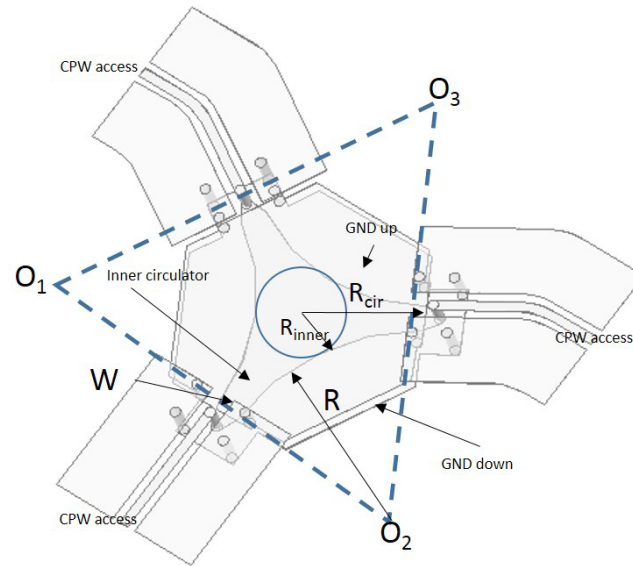


Figure 4.23: Edge-guided hexagonal circulator 3-D design for LTCC implementation

ones μ and μ_z . An improved tensor model is proposed by Igarashi and Naïto [86], however, preliminary measurement should be performed to determine some variables, especially when the applied field is relatively high. A generalized permeability tensor (GPT) model which works for both saturated and partially magnetized ferrite is described [89]. The GPT model takes into account the demagnetizing field, the anisotropic field, the interactions between the adjacent domains, etc leading to a more rigorous tensor model. Due to a complex calculation, this model is difficult to be implemented into EM simulators. Therefore, we employ the Green and Sandy's tensor model in this design. The model is obtained based on the measurement of the experimental characterization cells. It is valid when the operating frequency is higher than the resonance which meets our requirements. Moreover, this model is easier to be implemented than the model of GPT. Finally, a tunable antenna on a partially magnetized ferrite LTCC substrate [28] used this permeability tensor model in [91] and obtained good theory-measurement agreement. In our design, the same ferrite LTCC substrate is used. The Green and Sandy's equations which explain the

behavior of a partially magnetized ferrite material when using Z-bias (magnetic bias perpendicular to the circulators plane) are given by Equations (4.18) to (4.23), where μ'_0 is the initial relative permeability of the substrate in the demagnetized state, the relative μ and κ values replace the standard elements of the Polder permeability tensor, M and M_s are the partial and saturation magnetization, f is the circulator's working frequency and n is the coefficient expressing the deviation of κ from Rado's model, which is assumed for this work to be 0.5 since the same ferrite LTCC material ESL 40012 is used [28].

$$\text{Permeability} = \mu_0 \begin{bmatrix} \mu & -j\kappa & 0 \\ j\kappa & \mu & 0 \\ 0 & 0 & \mu_z \end{bmatrix} \quad (4.18)$$

$$\mu'_0 = \frac{2}{3} \left[1 - \left(\frac{\gamma 4\pi M_s}{\omega} \right)^2 \right]^{0.5} + \frac{1}{3} \quad (4.19)$$

$$\mu = \mu'_0 + (1 - \mu'_0) \left(\frac{M}{M_s} \right)^{1.5} \quad (4.20)$$

$$\kappa = n \frac{\gamma 4\pi M}{\omega} \quad (4.21)$$

$$\mu_z = \mu'_0 \left(1 - \left(\frac{M}{M_s} \right)^{2.5} \right) \quad (4.22)$$

$$\mu_{eff} = \frac{\mu^2 - \kappa^2}{\mu} \quad (4.23)$$

The circulator's working frequency could be calculated by Equation (4.24) for a

given value of the circulator’s radius R_{cir} (Figure 4.23), where the μ_0 is the permeability of free space, ε_f is the permittivity of the ferrite, ϵ_0 is the permittivity of the space and μ_{eff} is the effective permeability of the ferrite [37].

$$f = \frac{1.84}{2\pi R_{cir} \sqrt{\varepsilon_0 \mu_0 \varepsilon_f \mu_{eff}}} \tag{4.24}$$

The value of R_{cir} assumed for this work is 1.79 mm which is chosen for a circulator working at 14 GHz as shown in Figure 4.24. It is obtained by Matlab using Green and Sandy’s partially magnetized ferrite tensor when magnetization $\mu M=200$ mT. This magnetization value is the maximum value created by the winding as discussed in the winding’s design section. The reason why we use the approximate dimensions of a Bosma theory is that it gives us the smallest radius of the circulator (principal mode of the circulation). As is known, a small bias area requires reduced bias energy.

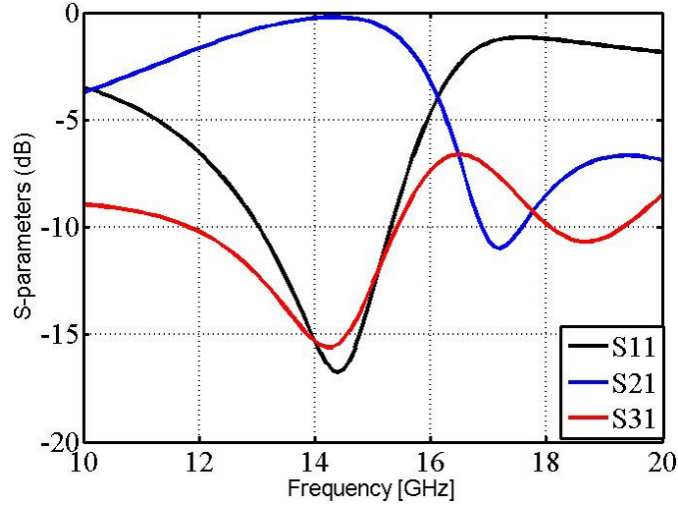


Figure 4.24: The simulated S-parameters in Matlab by employing Green and Sandy’s partially magnetized tensor model when $\mu M=200$ mT and $R=1.79$ mm

When we vary the internal magnetization μM , the circulation under different μM could be shown in Figure 4.25. When $\mu M=0$, there is a superposition of S21 and S12 curve meaning that the circulator works as a power divider. When we increase the

internal μM gradually, we create the circulation (separate S12 and S21) along with a frequency variation.

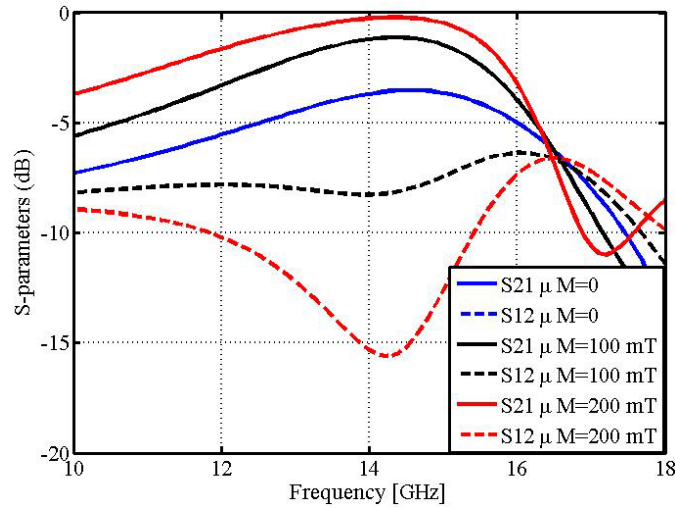


Figure 4.25: The simulated S-parameters in Matlab with Green and Sandy’s partially magnetized tensor model under different internal magnetization μM

Figure 4.26 demonstrates that in a partially magnetized ferrite, the circulator’s working frequency is in inverse proportion to μM when $n=0.5$. The frequency decreases from 14.6 GHz to 14.2 GHz when μM changes from 0 to 0.2 T leading to a variation of 0.4 GHz.

EM simulation by Ansys HFSS 15 (Ansys Electromagnetics Suite)

Figure 4.21a shows the stack-up of the 10 LTCC layers. As we said before, space priority is given to the dc windings, so the circulator is designed using a minimum number of layers: the stripline ground planes are on layers 5 and 7, whereas the circulator’s inner conductor is on layer 6. Referring to Figure 4.23, key parameters of an edge-guided circulator are the radius of curvature R and the width W of the center conductor at the circulator’s edge. The next difficulty consists in feeding the embedded circulator because it can only be probed on the top layer (layer 10). To

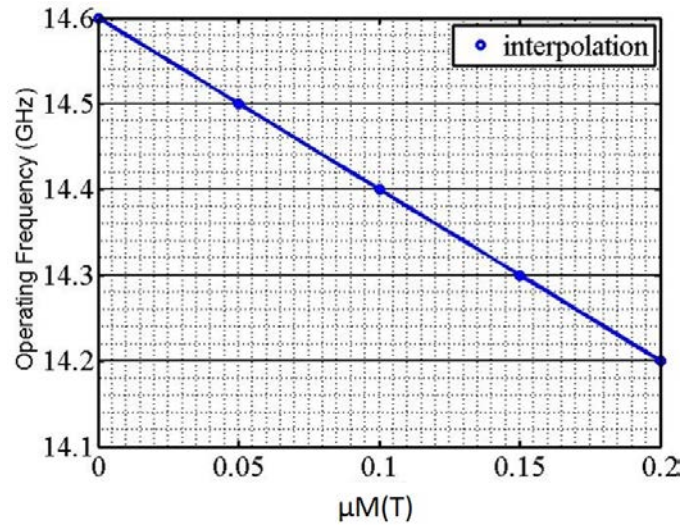


Figure 4.26: The circulator's working frequency in terms of the internal magnetization μM

solve this problem, three CPW transmission feed lines are designed on the top layer. The transition from the CPW feed lines to the embedded stripline circulator is shown in Figure 4.27, where five stacked vias are used to connect the signal lines and the ground planes. Both of the stripline ground planes are bonded by the vias to avoid exciting parasitic parallel plate modes.

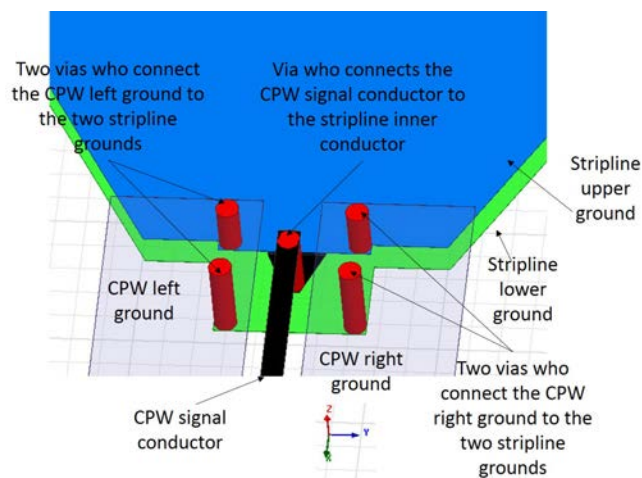


Figure 4.27: Transition from CPW transmission line to stripline

The simulator Ansys HFSS has predefined Polder equations for the ferrite's permeability tensor, and this is the only model allowed in HFSS. However, Polder model only works for saturated ferrites [9]. At that moment, we had only this simulator, so we performed the simulation anyway. In order to complete an approximate simulation for partially magnetized ferrites in HFSS, the magnetization M could be used instead of saturation magnetization M_s along with the corresponding internal H_i bias which can be found in [15]. For example, the circulator simulated above in Matlab has a partial magnetization $\mu M=0.2$ T, so the $\mu_0 M_s=400$ mT is replaced by $\mu M=0.2$ T and the H_i is set to be 500 A/m. This method allows to give an approximate simulation.

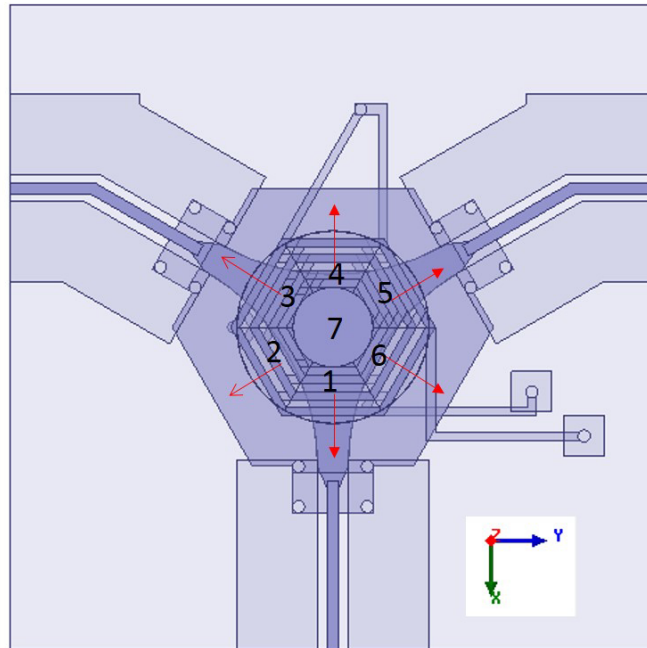


Figure 4.28a: Magnetic bias model in HFSS

In order to take the non-uniform magnetic field into account, a set of biased ferrites is manually created. Figure 4.22b shows that the \vec{B}_i vector has a dominant z-direction when x ranges from 0 to 0.6 mm. Then \vec{B}_i vector turns towards to the x-direction

(in xy plane) gradually for x from 0.6 mm to 1.3 mm. According to these features, the magnetic bias is designed to have 7 parts in HFSS as shown in Figure 4.28a. Part 7 is the center bias following the z-axis with an average value of 199 mT. Parts 1- 6 have the fields who have radial directions from the center (red arrows) with an average value of 132 mT. As known, HFSS allows non-uniform magnetic bias by using a co-simulation with Maxwell 3D. However, HFSS employs only Polder's equations to calculate the permeability tensor, therefore, we have to define the M_s of the ferrites in HFSS. Obviously, a $\mu_0 M_s = 0.4$ T is not accurate to model a partially magnetized ferrite. That's the reason why we use the model of 7 parts of ferrites whose M_s are replaced by M. The circulator is then optimized using Ansys HFSS which led to the final dimensions of the circulator: $R = 2.8$ mm and $W = 0.38$ mm, so R_{cir} equals 1.73 mm which is in agreement with the Matlab analysis ($R_{cir} = 1.79$ mm).

The simulated transmission coefficients by HFSS and Matlab are shown in Figure 4.28b. The simulation in Matlab uses Green and Sandy's model, and HFSS uses Polder's equations with 7 parts of ferrites whose M_s are replaced by M. Although the comparison seems to be unnecessary because they use totally two different ferrite models, however, this tells that the approximate model in HFSS still works to some extent. They both give a circulation at 14 GHz while Matlab has a better insertion loss.

According to the contact with Ansys, HFSS will probably allow user-defined tensor model such as ferrite permeability tensor in the version of 2016.

4.6.3 Measurements

The fabrication is performed by VTT Technical Research Centre of Finland with the help of Dr Atif Shamim at King Abdullah University of Science and Technology

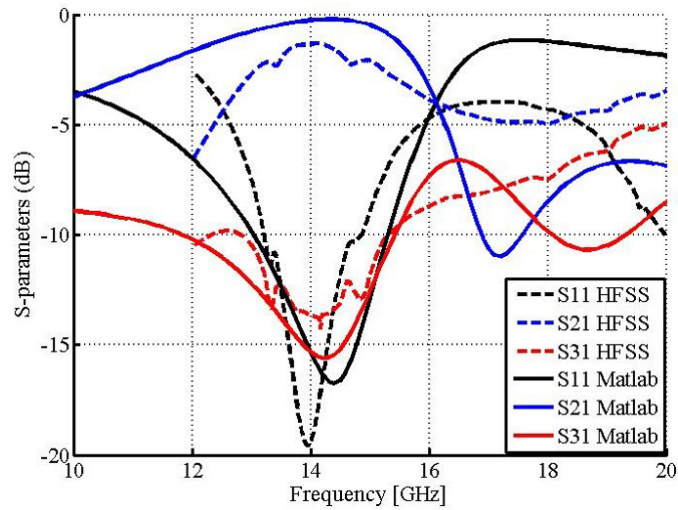


Figure 4.28b: Simulated S-parameters in HFSS and Matlab

in Saudi Arabia. A photograph of the three fabricated ferrite LTCC edge-guided circulators and one CPW thru line of 2.7 mm are shown in Figure 4.29. Note how the three ports of the circulator have been arranged in a T shape to accommodate the probing station's perpendicular probe arms. A bend in two of the CPW lines is therefore required and care is taken to ensure that these bends would not cause reflections near 14 GHz (see Figure 4.30). Two GSG rf probes ($500 \mu\text{m}$) are used to connect the port 1 and 2. An external dc source is connected to the dc pads by two dc-needles. An ampere meter is used to show the current strength in the winding. The network analyzer is the Agilent (Keysight) N5244A, 4-port (dual source) to 43.5 GHz. The measurement of a CPW thru is shown in Figure 4.31, which shows that the performance of the unbiased LTCC material is good between 10 GHz and 17 GHz. As expected in [121], the attenuation is indeed strong below 10 GHz due to the low-field losses.



Figure 4.29: Prototypes of the ferrite LTCC circulator

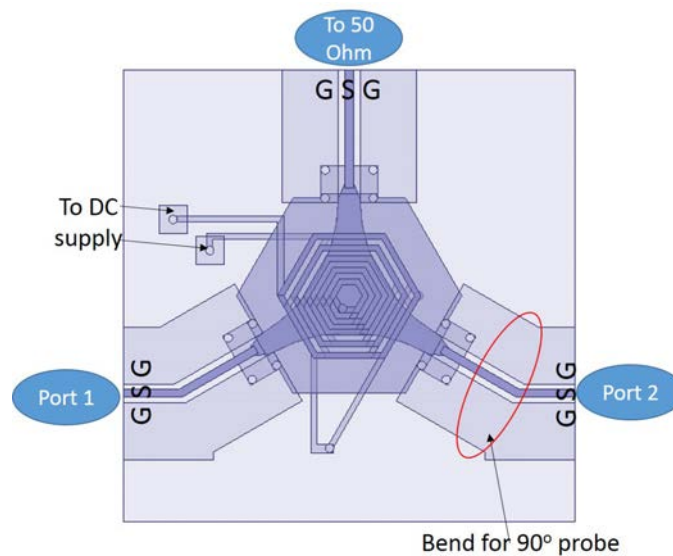


Figure 4.30: S-parameters measurement configuration

Measurement with bias current only

The measurement of the circulators is performed with a two-port network analyzer, with the third port (North) being matched (50Ω). When the windings are not energized, a matching point is found at 14.8 GHz as shown in Figure 4.32. The transmission and the isolation are identical with a value of -5 dB. This indicates that the

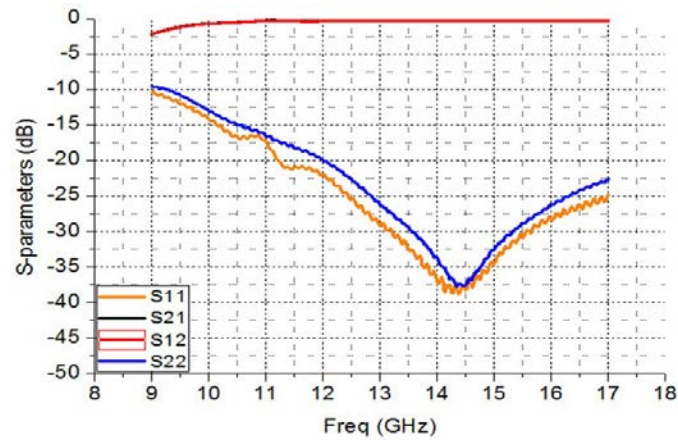


Figure 4.31: CPW transmission line measurement: S-parameters

circulator operates as a power divider (with losses) when it is not biased. There is a loss of 2 dB because the material has a loss of 1.5 dB/cm at 14 GHz for a transmission line [15]. The input-to-output length of our circulator is about 8.6mm, so the loss is approximately $1.5 \times 0.86 = 1.3$ dB which is in agreement with the measurement.

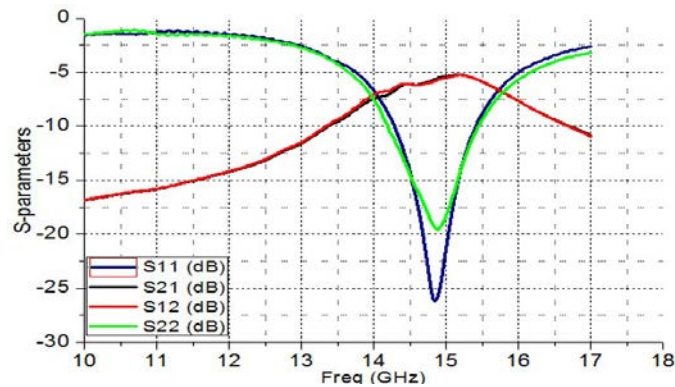


Figure 4.32: Measured S-parameters: Circulator without current

When a current of 100 mA is injected into the winding, circulation becomes apparent (see Figure 4.33). The transmission is pushed up to -4 dB and the isolation goes down to -7 dB at 14.67 GHz, whereas the reflections remain below -20 dB. When the current is increased to 300 mA, the performance of the circulator is further improved (see Figure 4.33). The transmission is about -3 dB and the isolation about -8 dB

at 14.2 GHz. A stronger current may be applied, but this could melt the winding. Moreover, the operating frequency is shifted as well from 14.8 GHz to 14.2 GHz in the measurement. We believed at that moment that the frequency variation was caused by the change of the internal magnetization M as expected in Matlab, however, this is finally proven that it is mainly caused by the temperature rise in the substrate and we will explain it later.

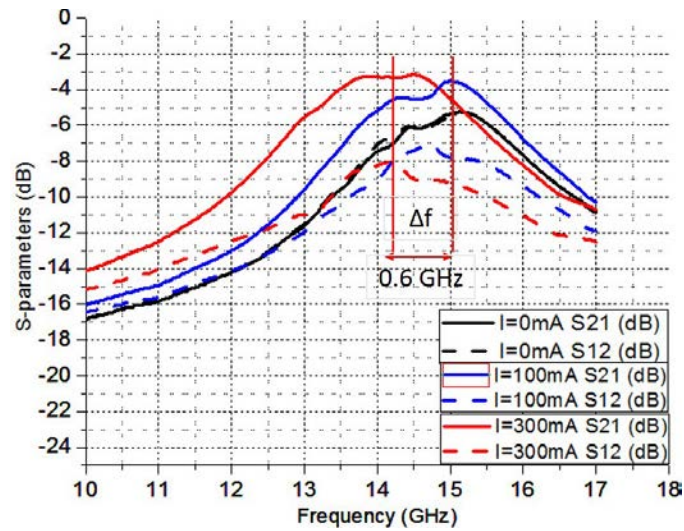


Figure 4.33: Measured S-parameters with current: S21 and S12 in terms of current

Figure 4.34a shows the comparison of simulated S21 and S12 between HFSS and the measurement, when a 300 mA current is injected into the winding. HFSS gives better insertion loss and isolation than the measurement. This is probably due to the additional losses of a partially magnetized ferrite and the inaccurate ferrite model in HFSS.

However, the simulation has a good agreement with the measurement in terms of reflections S11 and S22, as shown in Figure 4.34b. The circulator's operating frequency is also well predicted by the simulation.

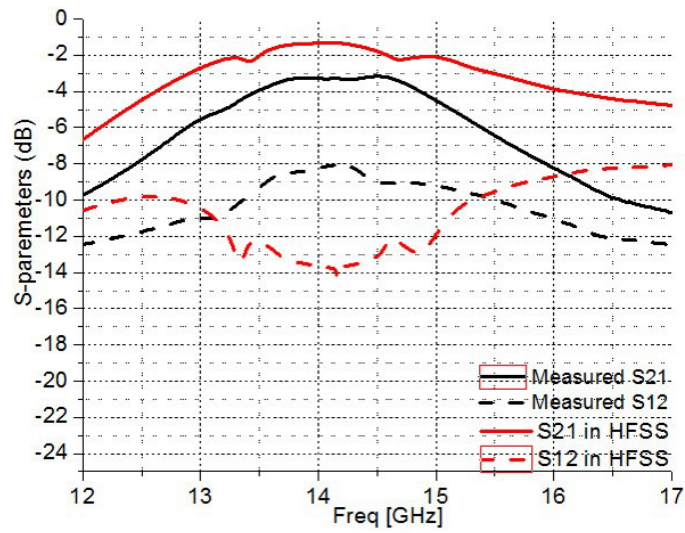


Figure 4.34a: Comparison of measurement and HFSS: S21 and S12

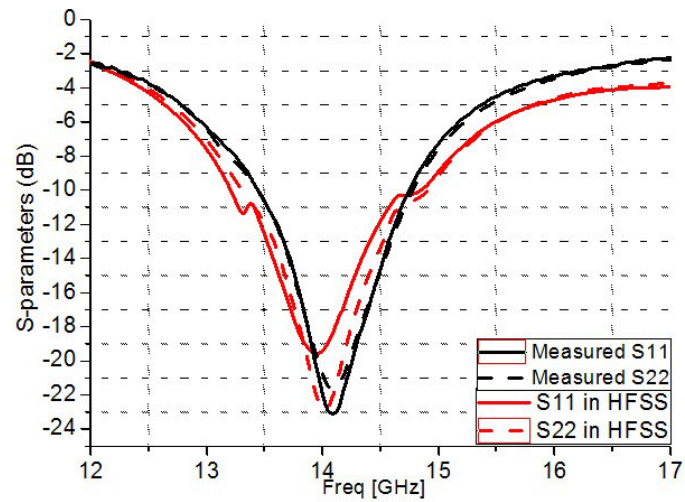


Figure 4.34b: Comparison of measurement and HFSS: S11 and S22

In addition, Figure 4.34c shows the S-parameters when the current is switched. As expected, the circulators' circulation is switched to the opposite direction.

Measurement with magnets

The measurement with the current confirms that the circulator is not well saturated using only the windings, so measurements with external magnets are performed as

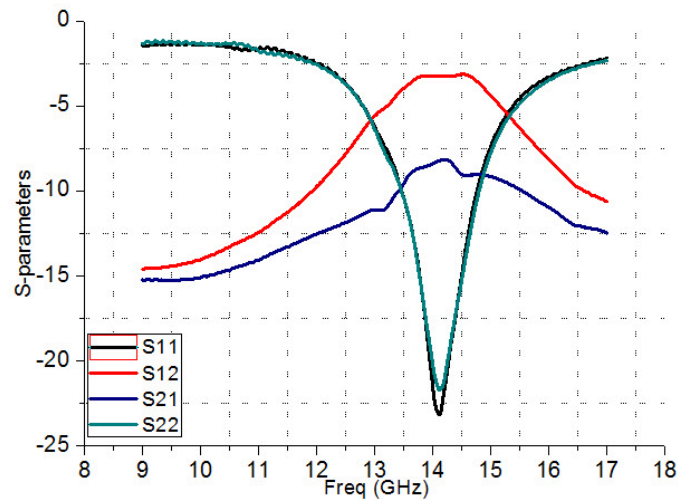


Figure 4.34c: Circulator with an opposite direction of 300 mA dc current: S-parameters

well. An external magnet with a surface field of 5200 Gauss plus a second one with 5903 Gauss surface field are applied on the top layer of the substrate and the bias diameter is 1/16 inch (1.5875 mm), as shown in Figure 4.35.

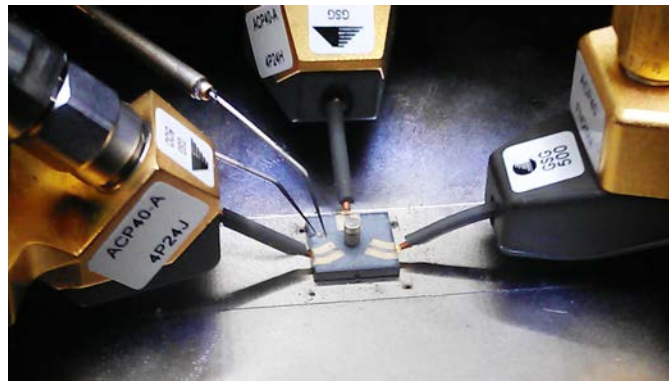


Figure 4.35: Measurement probe station photo

Figures 4.36a and 4.36b shows that the internal magnetic field \vec{B}_i is higher than 400 mT in the core of the circulator for a radius from 0 to 0.5 mm, therefore, the magnets could saturate the ferrite.

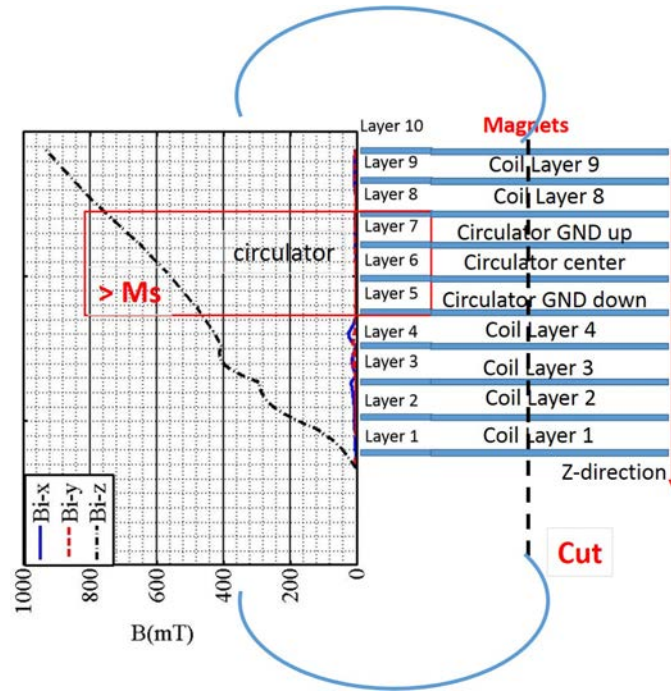


Figure 4.36a: Magneto-static simulation of the magnets in ferrite LTCC with a B-H curve: \mathbf{B}_i along Z axis

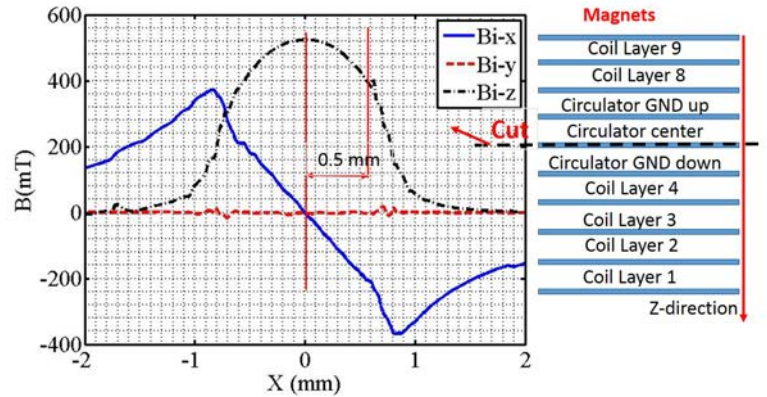


Figure 4.36b: Magneto-static simulation of the magnets in ferrite LTCC with a B-H curve: \mathbf{B}_i along X axis

Then we performed the measurements with the external magnets. The magnets greatly improve the performance of the circulator. The measured transmission and isolation is approximately -1.8 dB and -18 dB, respectively, when current $I=0$ mA is injected, as shown in Figure 4.37a, while the return loss is better than 20 dB

(Figure 4.37b).

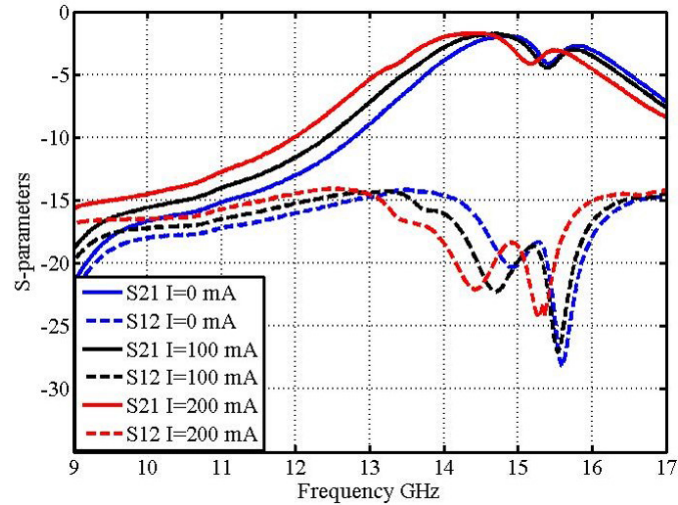


Figure 4.37a: S-parameters with magnets: S21 and S22 in terms of current

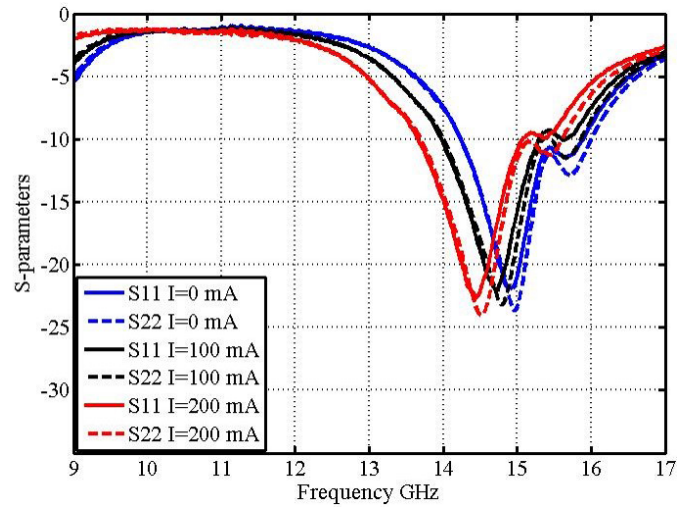


Figure 4.37b: S-parameters with magnets: S11 and S22 in terms of current

With the magnets, the internal magnetization can be adjusted by changing the current in the windings. When a current of 100 mA is applied to the windings (the H field created by the winding has the same direction of magnet's field), the circulator performance is shown in Figure 4.37a and Figure 4.37b. The isolation goes down to

-22 dB instead of -18 dB. When the current is increased to be 200 mA, the result is further improved. The transmission is about -1.6 dB, isolation is -23 dB and return loss is better than -20 dB. However, in this measurement, a frequency shift is also observed: from 14.8 GHz to 14.2 GHz.

This is interesting: we said before that the frequency variation was caused by the change of the internal magnetization M . However, in this measurement, the field created by the magnets is so strong that the field created by the winding could be negligible. Why do we still observe a frequency variation of 0.6 GHz? The hypothesis is that the temperature also affects the frequency variation. To prove that, we performed another measurement.

This time, the field created by the winding is opposite to the field of the magnets. We find that the frequency goes up a little when 120 mA current is injected, then the frequency goes down again if we continue increasing the current, as shown in Figure 4.37c. This measurement indicates that the variation of the circulator's frequency is not only caused by the change of the internal magnetization. The explanation of the frequency variation is that there are two elements that changes the circulator's operating frequency: the first is the change of magnetization M (hence μ_{eff}) by the winding, the second is the temperature rise in the substrate which affects μ and M_s leading to the variation of μ_{eff} . The temperature increases the ferrites μ as explained in [91] leading to the increase of μ_{eff} . Moreover, the temperature decreases the magnetization saturation M_s which increases the μ_{eff} as well when the ferrite is partially magnetized (Figure 4.37d). In conclusion, the frequency variation is achieved initially by the change of internal magnetization M , then the temperature plays a more important role in changing the μ_{eff} , as this ferrite LTCC substrate ESL 40012 is sensitive to the temperature.

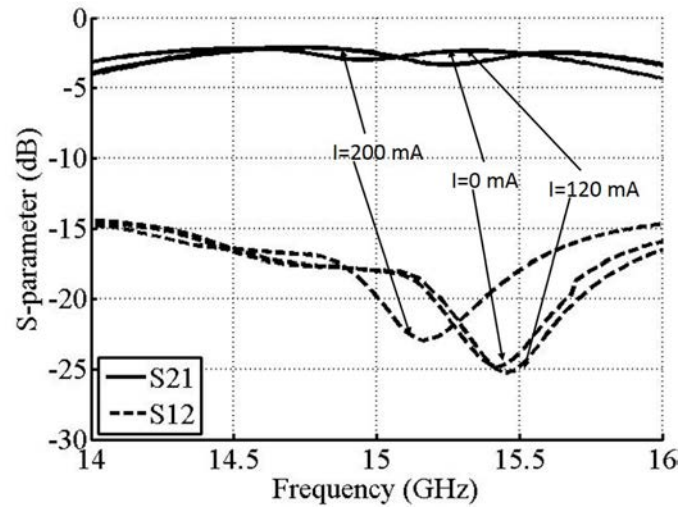


Figure 4.37c: Isolation and transmission curves when windings with the current is biased that opposes the magnetic fields of the magnet

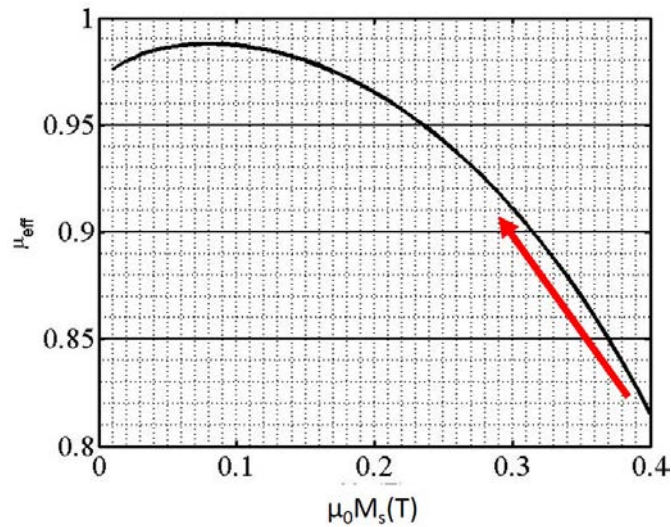


Figure 4.37d: μ_{eff} in terms of magnetization saturation $\mu_0 M_s$ with $\mu M = 0.2T$ when the ferrite is partially magnetized using the model of Green and Sandy

4.6.4 Retro Analysis

EM simulation by CST Studio

As discussed before, the simulator Ansys HFSS uses the Polder equations [123] to simulate saturated ferrites. This year, we finally have the access to CST Studio which

allows one to apply user-defined tensors manually [124], therefore we performed retro analysis with Green and Sandy's partially magnetized ferrite model in CST Studio, as shown in Figure 4.38a. The side-to-side length of the winding is 2.2 mm, so the radius of the bias area is set to be 1.27 mm. The remaining ferrite is assumed to be totally demagnetized with $M = 0$ and $M_s = 0$.

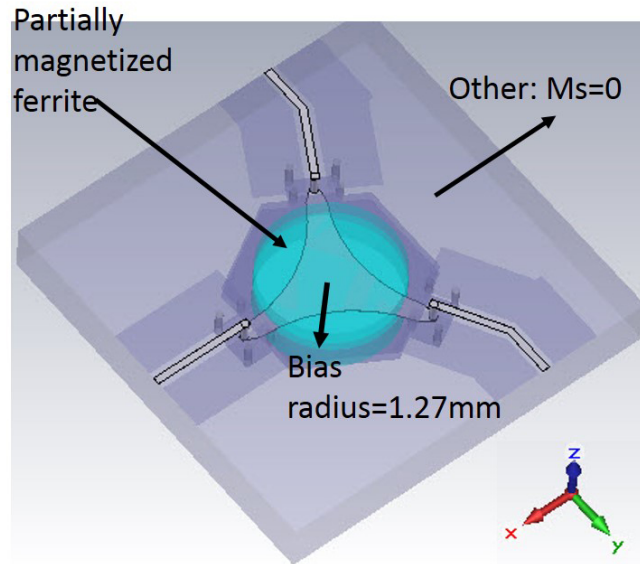


Figure 4.38a: Magnetic bias model in CST

Then the simulation is performed and we compare the simulated S-parameters with the measured ones when the internal magnetization μM is 200 mT, as shown in Figures 4.38b and 4.38c. CST gives a more close result for the transmission and isolation, however, the reflection is not accurate which is probably because we used a simplified and uniform bias field. However, the working frequency is also well predicted. At 14 GHz, the transmission and isolation is -3 dB and -9 dB respectively. More important, since Green and Sandy's partially magnetized ferrite model is used, we can perform the simulations with different internal magnetization μM . A frequency variation of 0.2 GHz is then observed when μM goes from 0 to 200mT, as shown

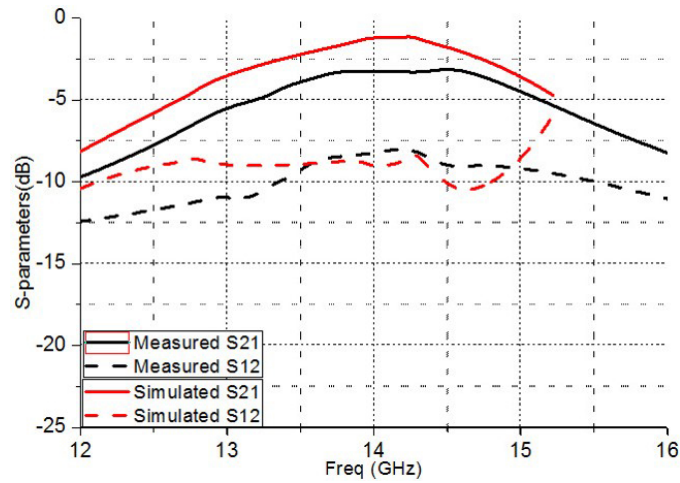


Figure 4.38b: Comparison of measured and simulated S21 and S12 by CST when internal magnetization μM is 200 mT

in Figure 4.38d. However, in the measurement, the variation is 0.6 GHz and the difference is due to the temperature rise in the substrate.

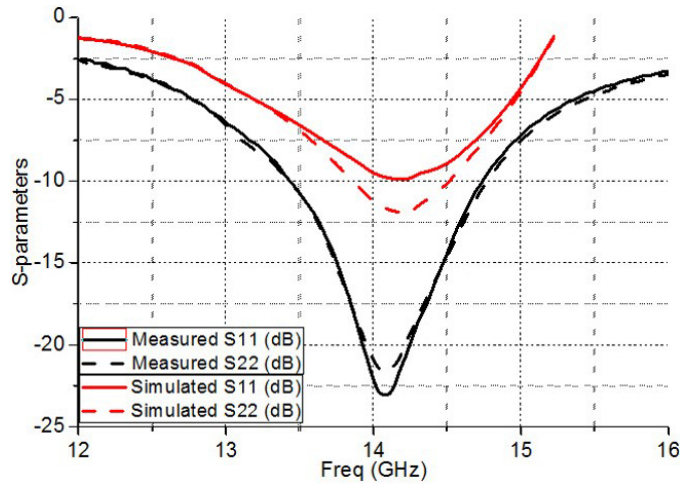


Figure 4.38c: Comparison of measured and simulated S11 and S22 by CST when internal magnetization μM is 200 mT

The final dimensions of the circulator: $R = 2.8$ mm and $W = 0.38$ mm, so R_{cir} equals 1.73 mm which is in agreement with the Matlab analysis ($R_{cir}=1.79$ mm).

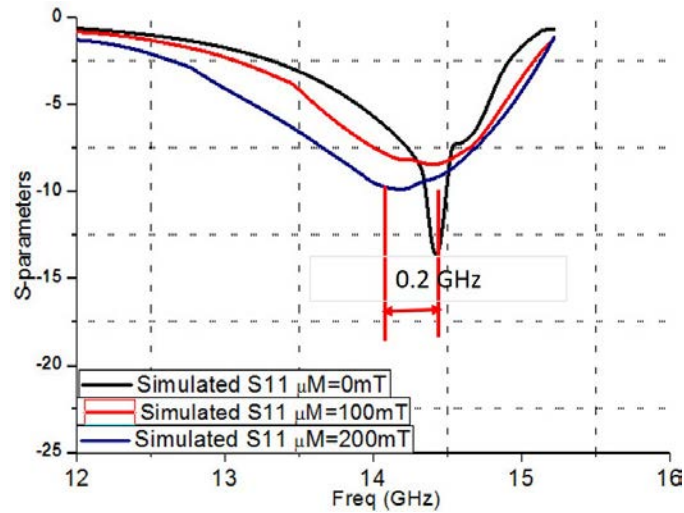


Figure 4.38d: Simulated circulator's frequency variation (S11 in dB) in terms of magnetization μM

4.6.5 Power Capability IP3

Given that ferrite devices are perceived as being nonlinear, so it is necessary to measure the third-order intercept point of a circulator made of ESL 40012 ferrite LTCC.

A two tone test is applied to the circulator in an attempt to measure its third-order intercept point. The 10-layer ESL 40012 ferrite LTCC with integrated winding circulator was used as the device under test. Two stacked magnets DH11 on top of DH101 (K&J magnetics) are employed to provide the external magnetic fields. Three 500 mm pitch GSG with 2.92 mm coaxial inputs and two DC probes are used. Two active RF ports are connected to the probes (port 3 of the circulator is terminated in a matched load). The analyzer is Agilent N5244A PNA-X with Option 87 (IMD). The calibration is realized as per instructions for Option 87 IMD measurements (ECal and power meter). Then we performed the swept-power IMD measurement (intermodulation measurement only). Figure 4.39 lists the details of the measurement.

Although oftentimes ignored, IM3 can actually vary as a function of: the input

power, the centre frequency, and the spacing of the two tones. Option 87 of the PNA-X allows IM3 measurements to be performed while sweeping any of these parameters. For simplicity, only the input power will be swept in this measurement, the rationale being that the best circulator performance was achieved around a centre frequency of 14.5 GHz, and using different Δf values won't offer any additional insight into the behaviour of the circulator. Only third order intermodulation measurement at 14.5 GHz are performed with an average of 64 sweeps. The variation of the frequency is 10 MHz. Input test tone power swept from -20 dBm to +5 dBm, levelled at port 1 and spectrum was measured at port 2 (output). Figure 4.39 lists the details of the measurements.

Circulator	10-layer ESL40012 ferrite LTCC with internal DC winding
Magnets	two stacked cylindrical magnets: DH11 on top of a DH101 (the latter contacts the LTCC)
Probes	Three 500 μm pitch GSG with 2.92 mm coaxial inputs, two DC probes
Ports	Two active RF ports (port 3 of the circulator is terminated in a matched load)
Analyzer	Agilent N5244A PNA-X with Option 87 (IMD)
Calibration	As per instructions for Option 87 IMD measurements (ECal and power meter)
DC bias	0, 350 mA and 430 mA

Figure 4.39: IP3 measurement details

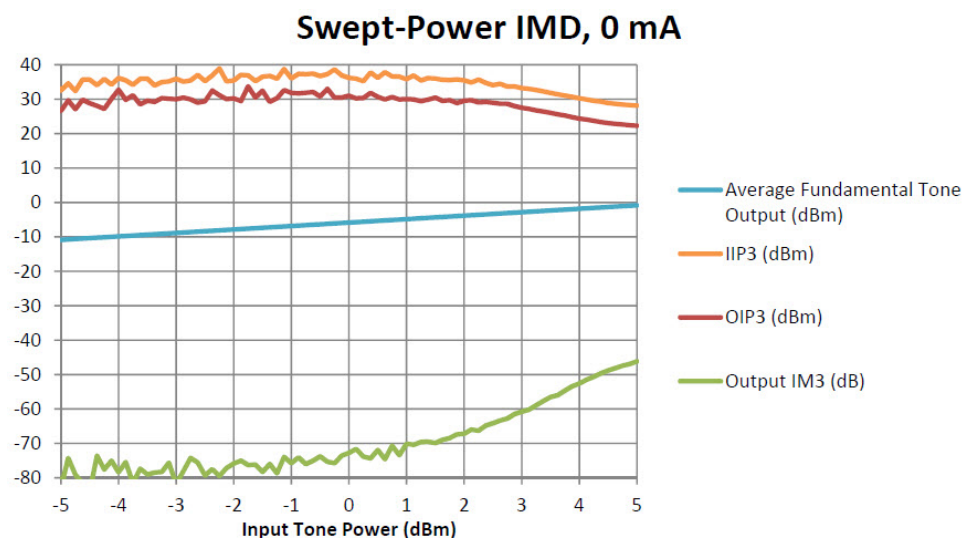


Figure 4.40: Swept-Power IMD Test when current $I=0$ mA

Figure 4.41 shows that the IM3 is lost in the noise for Input Tone Powers below approximately +1 dBm. As such, the data should only be trusted above this value. The IIP3 varies from approximately +35 to +28 dBm for input tone powers between +2 and +5 dBm. There is a clear downward trend, indicating more nonlinearity (decrease of IP3) as the input power is increased. It appears that the value is levelling-off at +5 dBm, but we would need more input power to verify if this is true or not. However, input power +5 dBm is the maximum power available of the equipment. The OIP3 is higher than the IIP3 because the output power is lower than the input lower due to the losses in the device.

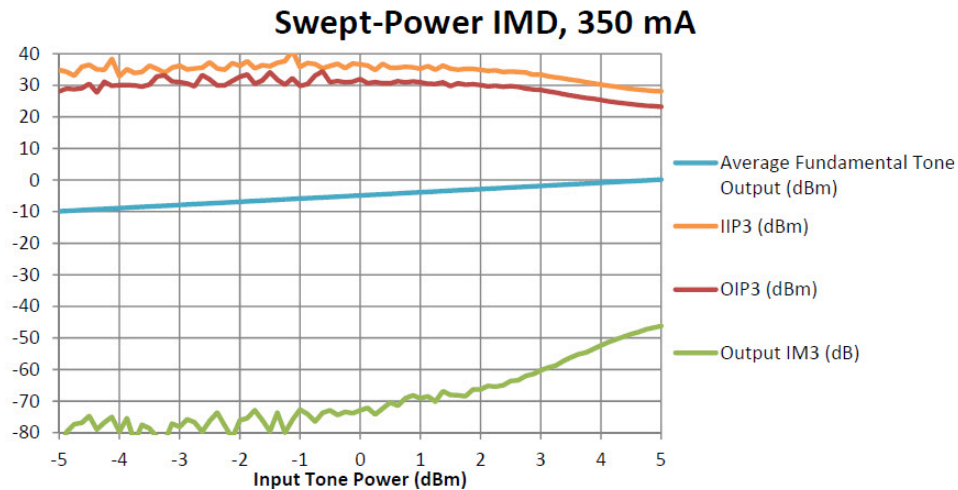


Figure 4.41: Swept-Power IMD Test when current $I=350$ mA

The results in Figures 4.41 and 4.42 are similar when a dc bias of 350 mA or 430 mA is applied, respectively: the IIP3 varies from approximately +35 to +28 dBm for input tone powers between +2 and +5 dBm. Therefore, the IP3 is about +30 dBm overall and the P1dB compression point is about 20 dBm.



Figure 4.42: Swept-Power IMD Test when current $I=430$ mA

4.6.6 Comparison and conclusion

The table below shows the main performance of different circulators realized by ferrite LTCC and conventional LTCC technology.

	F (GHz)	IL(dB)	ISO (dB)	RL(dB)	P1 (dBm)	Tech	Year
Our circulator only with current	14	3	8	20	NA	Ferrite LTCC	2015
Our circulator with magnets	14	1.6	23	22	20	Ferrite LTCC	2015
Circulator by T. Jensen	7.4	1.7	25	25	NA	LTCC	2011
Circulator by Jianhua Ji	15	0.84	26.7	NA	NA	LTCC	2009
Circulator by Raymond van Dijk	5.4	0.5	22	NA	45	LTCC	2014
Circulator by Raymond van Dijk	12	1.25	25	NA	43	LTCC	2014

Figure 4.43: Comparison of circulators realized by ferrite LTCC and conventional LTCC technology

When only current is used in our circulator, the device has an insertion loss 3 dB but the isolation is only 8 dB, so it is hard to call it a circulator. When external magnets are applied, the circulator has a better performance leading to an insertion loss about 1.6 dB and an isolation better than 20 dB. When it is compared with other circulators, especially the circulator at 15 GHz by Jianhua Ji, the insertion loss is less competitive. However, our circulators are approaching the performance of the

circulators realized by co-firing ferrite and conventional LTCC tapes. There are a number of ferrites which are compatible (shrink rate) with the conventional LTCC ceramic substrate. Designers have the freedom in ferrite selection and have taken the losses, working frequency, power requirement etc into account at that stage. However, there are few ferrite LTCC substrate suppliers in the market now and the ESL 40012 is sensitive to the temperature which limits our circulator's power capability. In the future, improved ferrite LTCC materials will lead to a competitive circulator's performance. Moreover, the main advantage of the ferrite LTCC technology over LTCC technology is that it allows to make stacking structures. In the later section, we will present a wide-band stacking circulator.

4.7 Coplanar ferrite LTCC circulators

4.7.1 Introduction

Previous section has already presented coplanar circulators, which can be easily fabricated at a low cost by using a lithography process. In our laboratory, several coplanar circulators with different operating frequencies are designed, fabricated and measured. This work demonstrates the feasibility of coplanar circulators based on ferrite LTCC and the maximum working frequency at which circulators can operate.

4.7.2 Design of coplanar circulators

The same ferrite LTCC tape ESL 40012 is used to design the coplanar circulators, but only 5 layers of tapes are employed. A coplanar circulator consists of a center conductor and metal grounds at the same level, connected to three CPW transmission line. Figure 4.44 [17] shows the top view of a conventional coplanar circulator design.

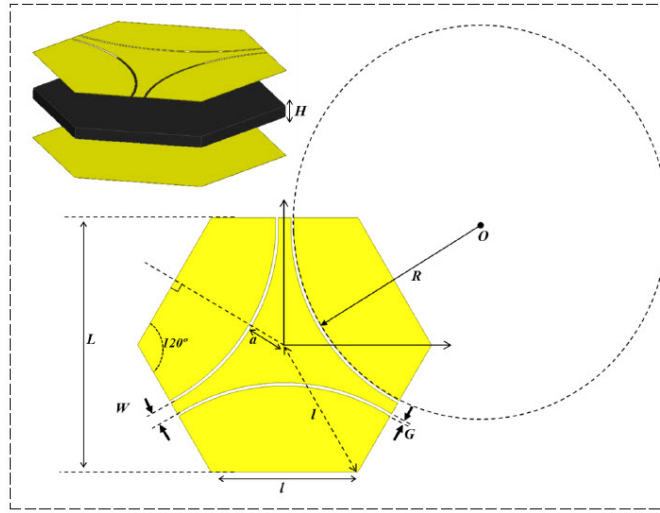


Figure 4.44: Design of a coplanar circulator (top view) [17]

The edge of the center conductor is an arc of a circle having a radius R . The circulator is fed by a CPW transmission line where the width is assumed to be W and the gap is G . The magnetic bias is provided externally by the magnet D101-N52 (K&J magnetics). Circulations at different frequencies could be found, by optimizing the metal ground size l , W , G and R .

Figure 4.45 shows different fabricated coplanar circulators operating at 18 GHz, 20 GHz, 22 GHz, 25 GHz, 27 GHz and 29 GHz, respectively. The simulated results have insertion loss better than 1 dB, isolation and return loss higher than 20 dB. Each circulator has two samples. CPW thru is also fabricated for the purpose of calibration.

4.7.3 Measurements

Due to a careless manipulation in the fabrication, the circulators have some defects leading to more losses and mismatch. Only the measurements of the circulators at 18 GHz, 22 GHz and 25 GHz are presented here.

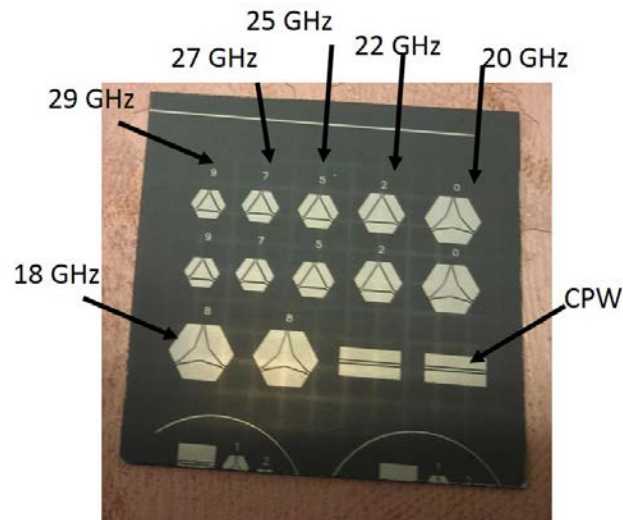


Figure 4.45: Fabricated CPW and coplanar circulators operating at different frequencies

Figure 4.46 shows a circulation around 18 GHz. The insertion loss is 4 dB which is a high loss, however the isolation is 23 dB. The matching is not good due to the defects during the fabrication.

The measured S-parameters of the coplanar circulator working at 22 GHz are shown in Figure 4.47. The matching is better than that of 18 GHz circulator leading to an insertion loss about 3 dB and the isolation remains higher than 20 dB.

As for the circulator at 27 GHz, the transmission and isolation start approaching to each other (toward -5 dB) as shown in Figure 4.48. This measurement demonstrates the difficulty of designing a high frequency circulator.

According to the above measurements, ferrite LTCC ESL40012 could be used to design circulators working from X band to K band. Higher frequencies could probably be realized when more powerful magnets are applied, but the characterization of this material over 30 GHz remains to be performed.

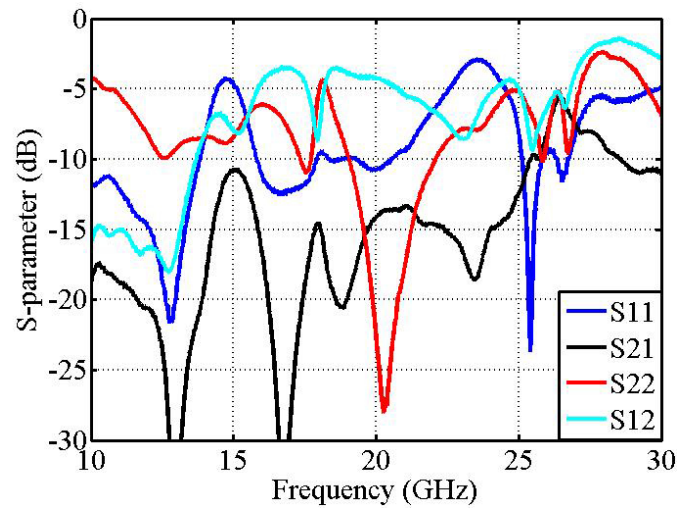


Figure 4.46: Measured S-parameters: coplanar circulator operating at 18 GHz

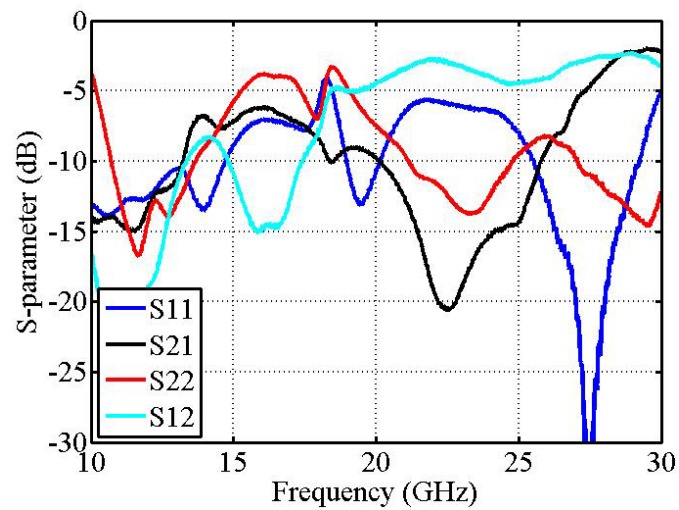


Figure 4.47: Measured S-parameters: coplanar circulator operating at 22 GHz

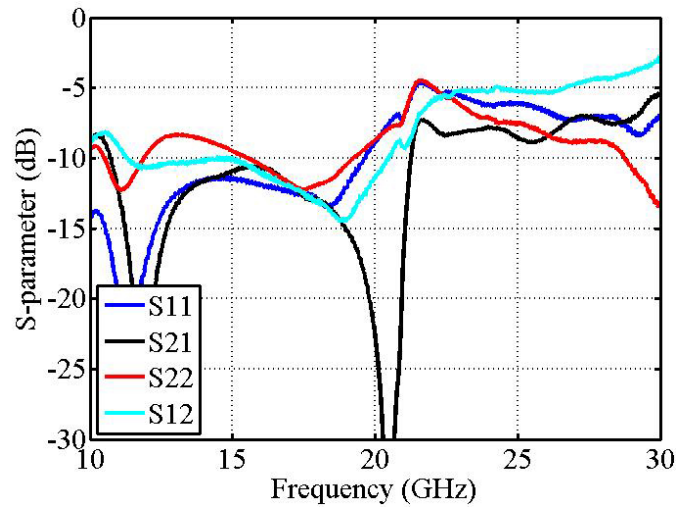


Figure 4.48: Measured S-parameters: coplanar circulator operating at 27 GHz

4.8 Wideband circulator by stacking two circulators

4.8.1 Introduction

The conventional circulator with stripline structure is designed to operate at a specific frequency. To expand the bandwidth, we usually work on the shape of the center conductor, or use a mode of "edge-guided" [59, 60, 122]. However, the 3D design capacity of the ferrite LTCC technology can be used to increase the bandwidth. This work presents a new wideband circulator operating at K-band. The design is realized by stacking two circulators (gyrators) with different working frequencies into the ferrite LTCC substrate to expand the overall bandwidth. The obtained bandwidth by simulator Ansys HFSS is 11 GHz (15.5 GHz to 26.5 GHz) which covers the K-band. The reflections and isolation are below -20 dB while the insertion loss is between 1.5 dB and 3 dB.

4.8.2 Theory and design

A stripline circulator is chosen because of the two metal ground planes that avoid the external environment [5,37]. The circulator design uses ten layers of ESL 40012 ferrite LTCC, where each layer has a thickness of $110 \mu\text{m}$. The electromagnetic properties of this ferrite have already been presented in previous sections.

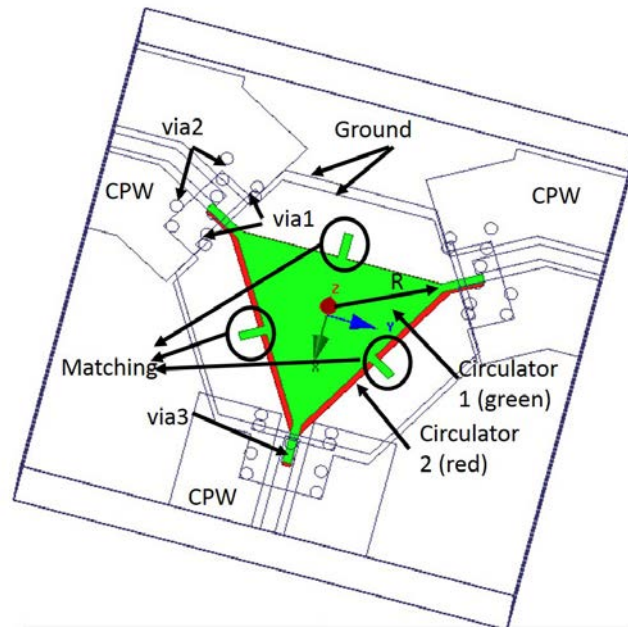


Figure 4.49a: Design of a wideband circulator by stacking two circulators

The design of this two stacking circulator is shown in Figure 4.49a. It is realized using a minimum number of layers: the two metal grounds are located above and below the center conductors of two circulators. Figure 4.49b shows the ten layers of LTCC ferrite. The additional layers where there are no conductors (layer 1-3 and 8-10) allow a better bias polarization in the ferrite. These layers help make the magnetic field perpendicular to the circulator plane (H_i follows the direction Z in Figure 4.49a). The CPW accesses are located on the top layer (layer 10) and allow the connection to the probe station. The external magnet is put below the device. The

two center conductors have a triangular shape which provides a wide bandwidth [46]. The dimensions of the two center conductors of the circulators are slightly different to further extend the bandwidth. The design also includes the impedance matching (see Figure 4.49a). One of the design challenges is to feed the two stripline circulators at the same time, because they can only be connected on the top layer (layer 10). The transition from CPW lines to stripline is represented in Figure 4.49b, where two vias of type 1 connect the two grounds of CPW to the upper ground of the stripline; similarly for the vias of type 2, which connect the two grounds of CPW to the lower ground of the stripline; and finally, a via of type 3 connects the signal conductor of CPW to the two circulators' center conductors. The fact that all ground planes are connected by vias prevents the excitation of parasitic modes. As there is no metal ground between the two center conductors, the two circulators are coupled. The equivalent circulator has a total dimension (L * W * H) 8mm * 8mm * 1.1mm.



Figure 4.49b: Ferrite LTCC layers configuration

The external magnet (D42B-N52 from K&J magnetics), produces a surface field about 5233 Gauss and has a residual flux density $B_{r_{max}} = 14800$ Gauss. Its diameter is 6.35 mm (1/4 inch) and the height is 3.175 mm (1/8 inches). The magnet is placed below the substrate. A simulation in Ansys Maxwell 3D is performed to find the

distribution of the internal field in the circulator structure (see Figure 4.50a).

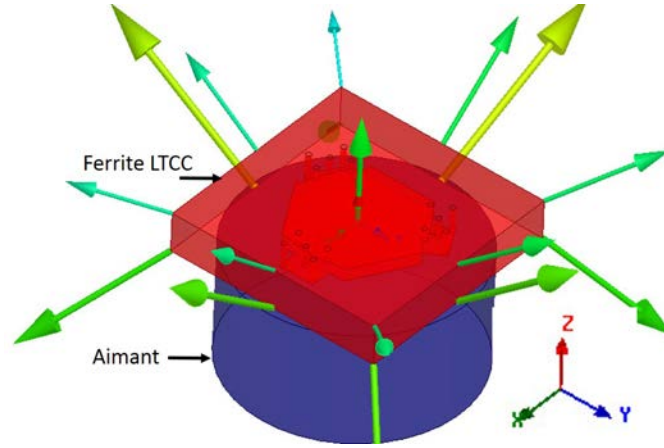


Figure 4.50a: Distribution of magnetic field H_i in ferrite LTCC

Figure 4.50b shows the internal field B_i along the axis \vec{z} . According to this plot, the magnetic field mainly follows the z-direction as we expected. The magnetic field strength between the layer 4 and 7 (where there are two cores of the circulators) is greater than M_s which means that the magnets could saturate the ferrite material [15].

4.8.3 Simulation

Firstly, an approximate simulation (the program in Matlab described before) is performed using the mathematical calculations proposed by Bosma [122]. Although this design is not a traditional stripline circulator, the program still gives an approximate dimension of the center conductor which favors the optimization in Ansys HFSS. Matlab shows a possible circulation at K-band with a radius $R_{cir} = 1.385$ mm (which is the R in Figure 4.49a).

Although the bias field is nearly uniform, any form of ferrite material has a nonuniform demagnetizing field, resulting in a non-uniform internal field in the ferrite (see Figure 4.50a). In practice, a uniform bias field is difficult to achieve. To model a

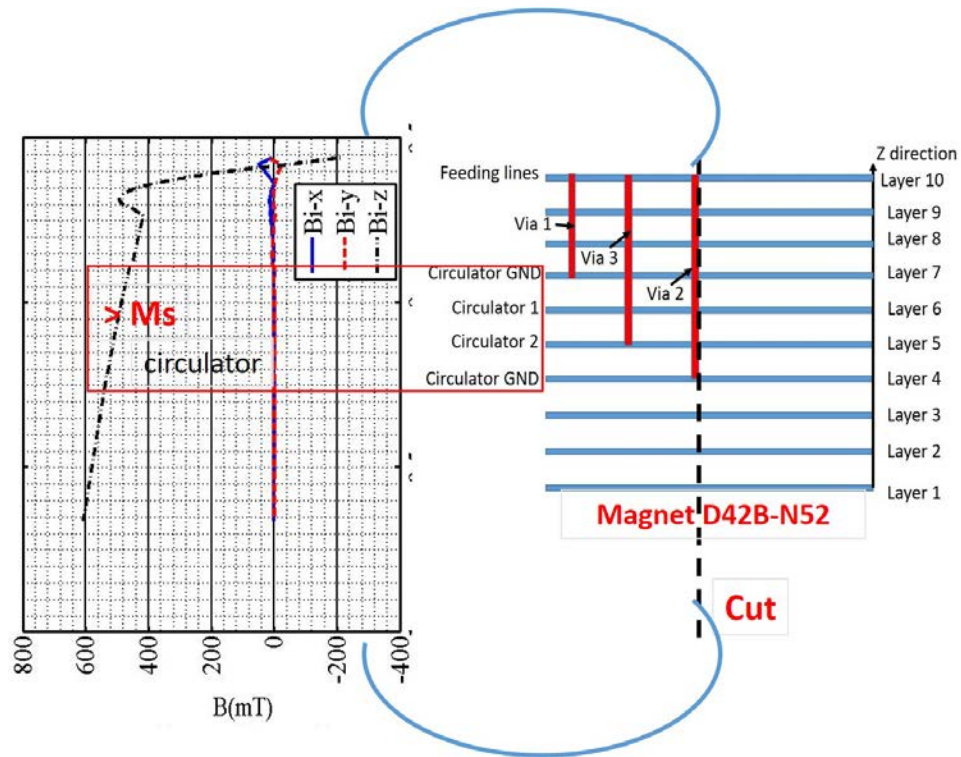


Figure 4.50b: Internal bias field B_i in terms of Z

ferrite polarized by a static magnetic field, we need to know the value and the direction of the bias field at any point in the structure. In this design, in order to account for this non-uniform dc bias field, we use the "non-uniform magnetic bias" in Ansys HFSS software which calls Maxwell 3D to generate a solution of the non-uniform magnetostatic magnetic fields. Once the dc simulation is performed, the distribution of the internal magnetic field can be imported into ANSYS HFSS automatically and then be used to perform a rigorous simulation.

We optimize the dimension of each circulator to obtain a wide bandwidth at K-band. The final simulations lead to $R_1 = 1.5$ mm and $R_2 = 1.6$ mm for circulator 1 and 2, respectively, which is in agreement with the analytical simulation.

Figure 4.51 shows that the circulator has an optimized bandwidth of 11 GHz (15.5-26.5 GHz) which covers the K band. The reflections and isolation are higher

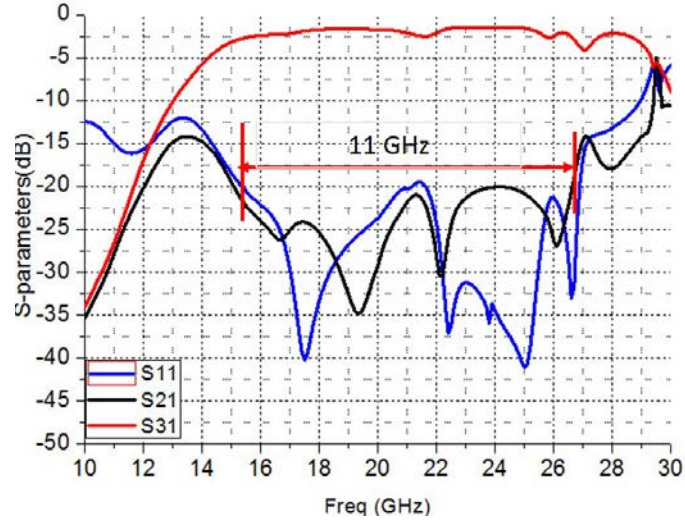


Figure 4.51: S-parameters by co-simulation in HFSS and Maxwell 3D

Table 4.1: Compare of circulators realized with LTCC technology

F(GHz)	Bandwidth(GHz)	IL(dB)	ISO	Reference
7.4	0.1	1.7	30	[24]
15-17	2	<1	25	[23]
11.5-13.5	2	<1	>22	[23]
15.5-26.5	11	1.5-3	>20	this design

than 20 dB and the insertion loss is between 1.5 dB and 3 dB. Table 4.1 shows the performance of different circulators realized with LTCC technology. Our circulator has an impressive wide-band performance compared with the other three cited circulators, but the insertion loss is higher due to the magnetic material losses ($\Delta H = 250$ Oe).

4.9 Conclusion

In this chapter, a CPW transmission line is measured to have a first impression of the ferrite LTCC device. Then an edge-guided circulator with external magnets is realized

with a full ferrite LTCC tape without any other ferrites or dielectric materials. At the operating frequency of 15 GHz, the transmission is approximately -1.8 dB, the isolation is -20 dB and the reflection is better than -20 dB. This work demonstrates that circulators and isolators can be integrated into the ferrite LTCC substrate and has shown the potentiality as a candidate for System-in-Package(SiP).

Then a study of a novel circulator with integrated winding is presented, for the first time. The device exhibits a multifunctional device controlled by the winding. When the windings are not energized by the current, the material is not magnetized, so this device operates as a power divider. Each port has a power of -5 dB with a return loss better than 20 dB at 14.8 GHz. When the windings are energized by a current, this device operates as a circulator. In addition, the circulator's circulation direction can be changed by switching the feeding current's direction. With a current of 300 mA, the circulator shows a transmission of -3 dB, an isolation of -8 dB and the return loss better than -20 dB at 14.2 GHz. With an external magnet, the material gets a stronger internal field which improves greatly the performance: transmission -1.8 dB, isolation -18 dB and return loss better than -20 dB at 14.8 GHz. When external magnets and current are both applied, adjustment of the internal H field by changing the current is possible to get a better result: transmission -1.6 dB with isolation and return loss both better than 20 dB at 14.2 GHz. The circulator's working frequency variation is 0.6 GHz. This is caused firstly by the change of internal magnetization M when current is less than 120 mA, then the heat due to the winding increases the ferrite's μ_{eff} leading to more frequency shifting. This novel circulator's performance is limited by the ferrite LTCC material. There are currently few commercially available ferrite LTCC materials, none specifically for microwave. A fully magnet-free, frequency tunable, and multifunctional circulator controlled by the winding is expected, as better materials with temperature stability, low-loss and

more layer-capacity become available.

Finally a design of a wideband circulator by stacking two circulators in ferrite LTCC is described. It is possible to integrate circulators with different operating frequencies into ferrite LTCC to create dual-band or tri-band circulators or combine their effects to achieve a broadband circulator. Although losses are still too high, simulated performance is significant for a very wide fractional bandwidth (50 %).

Chapter 5

Conclusion and perspectives

5.1 Conclusion

The thesis studies rf non-reciprocal components (circulators) based on ferrite LTCC. We investigate original circulator design fully embedded in ferrite LTCC, study the performance of a ferrite LTCC circulator with integrated winding and investigate a wide-band circulator based on the ferrite LTCC substrate. The works are realized at University of Saint Etienne France, Laboratory Hubert Curien UMR CNRS 5516, Carleton University Canada and Royal Military College Canada.

The thesis follows the scenario of designing a ferrite LTCC circulator with integrated winding as follows: Conception of the circulator \Rightarrow Magnetic material \Rightarrow Operating point \Rightarrow DC simulation of the winding \Rightarrow Matlab simulation \Rightarrow EM simulation \Rightarrow Fabrication and measurements \Rightarrow Retro-analysis.

The conception of the circulator is located in Chapter 2. In our design, the junction circulator is employed because it is well studied by the researchers and widely employed in microwave applications, such as radars. In the circulator, we also have different structures, such as stripline structure, microstrip structure and coplanar structure. Since we will integrate a winding into the circulator, we must protect

it from the interface of the winding. Therefore, the stripline line structure is chosen because the two metal grounds provide rf shielding against the winding while simultaneously allowing the magneto-static bias field into the ferrite core.

The magnetic material and the choosing of the operating point are in Chapter 3. The main difference between ferrite materials and dielectric materials is the permeability. For ferrites, as an example, the permeability is a tensor instead of a constant. Circulators commonly work on saturated ferrites and Polder's equations are used to calculate the tensor elements. If the ferrite is partially magnetized, there are a number of theories to model the permeability tensor. In this thesis, we use Green and Sandy model, which is obtained based on the measurements of the experimental characterization cells. It is valid when the operating frequency is higher than the resonance. This model is easier to be implemented than the GPT model. Moreover, this model has been implemented to analyze a patch antenna based on the partially magnetized ferrite LTCC ESL 40012 substrate and proven to be a good approximate model. The magnetization frequency is 11.2 GHz when $\mu_0 M_s = 0.4$ T, so an operating frequency higher than 14 GHz is chosen to avoid low-field losses. We operate our circulators in low Hi zone which requires a weak H field. If the ferrite is partially magnetized, the tensor element μ or κ is a function of the internal magnetization M and they are in proportional. The μ_{eff} is also a function of the internal magnetization M, which could be used to analyze the circulator's operating frequency variation.

In Chapter 4, we present the design, simulation and measurement of the winding and the circulator with integrated winding. 10 ferrite LTCC layers were used and the space priority is given to the DC winding. The stripline circulator only occupies three layers (5-7) and the top layer is reserved for the connections, so all the other layers are used to design the winding. Therefore, we have four coils below the circulator on layers 1-4 and two coils above the circulator on layers 8 and 9. On each layer of the

winding, hexagonal planar coil is chosen because it approaches to a circulator one. Each coil consists of 5 turns of a 0.1-mm wide conductor with a 0.1-mm spacing, both are the minimum values allowed in the fabrication process. The inner coil turn has a side-to-side width of 0.4 mm whereas the outer turn has a side-to-side width of 2.2 mm. 150- μm diameter vias are used to connect the coils and DC current in the winding is supplied by two dc pads on the top layer. Then we performed the dc simulation in Maxwell 3D. The internal magnetic field is approximately 200 mT in the core of the circulator when the applied current is 300 mA. The magneto-static field tends to create a closed dipole field around the upper and lower coils because the ferrite-air boundary limits the field in the ferrite material and the xy flux paths are thin and tend to saturate first. On the layer 9, the dc magnetic field is in the plane xy as we expected and on the layer of the center conductor of the circulator, the dc magnetic field mainly follows the z-direction for a radius of 0.6 mm and then it turns to the plane xy. Based on the theory of Bosma, we performed the S-parameters simulations when the internal magnetization μM is 200 mT. A circulation at 14 GHz is found and the radius of the circulator is found to be about 1.79mm. Matlab uses Green and Sandys model, so the circulator's operating frequency f is a function of μ_{eff} . However, μ_{eff} depends on then internal magnetization M , so f is a function of M as well. Therefore, we performed several S-parameters simulations with different internal magnetization M . When $M=0$, we see the superposition of the curve S_{12} and S_{21} which means that the circulator operates as a power divider. When we increase the M , we separate these two curves, creating the circulator along with a frequency variation. According to these simulations, the circulator's operating frequency is inversely proportional to the M . We then designed the circulator in HFSS. HFSS uses Polder's equations for saturated ferrites. In order to perform an approximate simulation in HFSS, seven parts of ferrites are defined in HFSS whose M_s are replaced by the M because the

ferrite is not fully saturate. The part 7 follows the z-direction with an average value about 199 mT and the parts 1-6 have radial directions with an average value about 132 mT. Then we performed the simulation in HFSS and compare the result with Matlab. Both give a circulation at about 14 GHz. The optimized radius of the circulator in HFSS is 1.73mm which is in agreement with the Matlab simulation 1.79 mm. Matlab has a better insertion loss. This comparison tells that our approximate model works to some extent. Then we fabricated them with a price of 30,000 euros for a panel of 5cm*5cm. We then performed the S-parameters measurements when a current 300 mA is injected and compared the result with HFSS. HFSS gives a good result for reflections, but not accurate for the insertion loss and isolation due to the inaccurate ferrite model in HFSS. However, the operating frequency 14 GHz is well predicted. Since the ferrite is not saturated, we performed S-parameters simulation with external magnets. The presence of the magnets greatly improved the performance, leading to an insertion loss 1.6 dB and an isolation over 20 dB. However, we observed a frequency variation about 0.6 GHz. The variation of the circulator's working frequency is 0.6 GHz. This is achieved firstly by the change of internal magnetization M when current is less than 120 mA, then the heat in the substrate due to the winding introduces more frequency shifting. Later, we performed the retro-analysis using CST studio where Green and Sandy's model is entered. The simulation in CST gives a close result for the insertion loss and isolation but the reflection result is not accurate, which is probably because we used a simplified and uniform bias field in CST. A frequency variation about 0.2 GHz is observed when μM goes from 0 to 0.2 T. Then we measured the IP3 about 30 dBm leading to a P1dB about 20dBm. Then we compared our ferrite LTCC circulator with other LTCC circulators. The comparison shows that our circulators are approaching the performance of the circulators realized by co-firing ferrite and LTCC tapes. Since there are a number of ferrite materials

which could be co-fired with LTCC substrate, designers have the freedom to choose the right ferrite (losses, power, M_s etc) for their devices. However, there are few commercial ferrite LTCC substrates and ESL 40012 is sensitive to the temperature which limits the power capability. Later we tested several coplanar circulators to find the maximum operating frequency that the material can support. Finally a design of a wideband circulator by stacking two circulators in ferrite LTCC was described. It is possible to integrate circulators with different operating frequencies into ferrite LTCC to create dual-band, tri-band circulators or combine their bandwidths to achieve a broadband circulator. Although the insertion loss is about 1.5 dB, the bandwidth is really impressive, about 11 GHz.

In summary, a study of a circulator with integrated winding based on ferrite LTCC is performed. The circulator needs to maintain the dc current which is less reliable than the external magnets. The performance is less competitive than the circulators based on conventional LTCC due to the limit of the ferrite LTCC substrate. However, a fully magnet-free, frequency tunable and multifunctional circulator controlled by the winding is expected, as better materials with temperature stability, low-loss and more layer-capacity become available. Besides, the thesis demonstrates that the ferrite stacking feature allows to design a wide-band circulator by stacking two circulators with different operating frequencies.

5.2 Perspectives

Improved performance of the circulator with integrated winding is expected when improved commercial ferrite LTCC materials become available, especially the ones with high temperature capability and low losses. Besides, advanced fabrication process with more layers capability could also contribute to the winding design leading

to more dc magnetic field in the circulator. We could also use the GPT permeability tensor model to improve the circulator design and optimization.

In the future, circulators could be integrated with other rf components such as oscillators, power amplifiers, filters, antennas etc using ferrite LTCC technology to achieve final products. LTCC technology could also offer multi-material modules, where materials with different electrical properties could be combined within the substrate.

In order to increase the internal magnetic field, small magnets could be integrated into the ferrite LTCC substrate creating the bias field from the inside. This will greatly improve the strength of the internal magnetic field, since there is no demagnetization fields.

We could also expect a "hard" ferrite LTCC substrate which allows to embed a winding. By energizing the winding with a pulse of current, a latching switch could be realized based on a circulator.

Dual-band or multi-band circulator by stacking several circulators with different bands are possible.

Integrated active elements or varactors could be used to perform matching compensation for the impedance variation of the circulator.

List of References

- [1] I. JQL Electronics, “Curie temperature,” *official website*, 2015.
- [2] P. Semiconductors, “Circulators and isolators, unique passive devices,” *Philips Semiconductors*, 1998.
- [3] E. Ohm, “A broad-band microwave circulator,” *IRE Transactions on Microwave Theory and Techniques*, vol. 4, no. 4, pp. 210–217, 1956.
- [4] S. Ewing and J. Weiss, “Ring circulator theory, design, and performance,” *IEEE Trans. MTT*, vol. 15, no. 11, pp. 623–628, 1967.
- [5] H. Bosma, “On stripline Y-circulation at UHF,” *IEEE Trans. MTT*, vol. 12, no. 1, pp. 61–72, 1964.
- [6] H. Dong, J. Smith, and J. Young, “A wide-band, high isolation UHF lumped-element ferrite circulator,” *Microwave and Wireless Components Letters, IEEE*, vol. 23, no. 6, pp. 294–296, 2013.
- [7] J. Wang, A. Yang, Y. Chen, Z. Chen, A. Geiler, S. Gillette, V. G. Harris, and C. Vittoria, “Self biased Y-junction circulator at ku band,” *Microwave and Wireless Components Letters, IEEE*, vol. 21, no. 6, pp. 292–294, 2011.
- [8] N. Estep, D. Sounas, and A. Alu, “Magnetic-free, fully integrated, compact microwave circulator using angular-momentum biasing,” *Antennas and Propagation Society International Symposium (APSURSI), 2014 IEEE*, pp. 340–341, 2014.
- [9] D. M. Pozar, “Microwave engineering 4th edition,” *John Wiley and Sons, Inc*, 2011.
- [10] A. N. ANL, “Ferrite material,” *Microwave Physics and Techniques*, 2003.

- [11] MMG, “Magnetic materials background information,” *University of Birmingham*, 2015.
- [12] B. Bayard, “Thesis report: Contribution au developpement de composants passifs magnetiques pour l’electronique hyperfrequence,” *Université Jean Monnet Saint Etienne France*, 2000.
- [13] R. Center, “Resource center,” *NDT Course Material*, p. 3, 2015.
- [14] T. CERAMICS, “Temex: Microwave ferrite materials,” *Microwave Ferrites*, 2015.
- [15] A. Shamim, J. Bray, N. Hojjat, R. A. Elasoued, and D. Baillargeat, “Microwave and magnetostatic characterization of ferrite LTCC for tunable and reconfigurable sip applications,” *Microwave Symposium, 2007. IEEE/MTT-S International*, pp. 691–694, 2007.
- [16] Y. Imanaka, “Multilayered low temperature cofired ceramics (ltcc) technology,” *Springer*, 2005.
- [17] A. TCHANGOULIAN, “Thesis report: Utilisation de matériaux composites magnétiques à nanoparticules pour la réalisation de composants passifs non réciproques micro-ondes,” *Université Jean Monnet Saint Etienne France*, 2014.
- [18] K. Oshiro, H. Mikami, S. Fujii, T. Tanaka, H. Fujimori, M. Matsuura, and S. Yamamoto, “Fabrication of circulator with coplanar wave guide structure,” *IEEE Trans. Magnetics*, vol. 41, no. 10, pp. 3550–3552, 2005.
- [19] T. Wada, R. Nakajima, H. Obiya, T. Ogami, M. Koshino, M. Kawashima, and N. Nakajima, “A miniaturized broadband lumped element circulator for reconfigurable front-end system,” *Microwave Symposium (IMS), 2014 IEEE MTT-S International*, pp. 1–3, 2014.
- [20] G. Radosavljevic, L. Zivanov, W. Smetana, A. Maric, M. Unger, and L. Nad, “A wireless embedded resonant pressure sensor fabricated in the standard LTCC technology,” *IEEE J.SENSOR*, vol. 9, no. 12, pp. 1956–1962, 2009.
- [21] K.-L. Wu and Y. Huang, “LTCC technology and its applications in high frequency front end modules,” *Antennas, Propagation and EM Theory, 2003. ARTICLE. 2003 6th International Symposium on*, pp. 730–734, 2003.

- [22] C. Atzlesberger and W. Smetana, "Evaluation of a centrifugal micropump realized in LTCC-technology," *Electronics Technology, 30th International Spring Seminar on*, pp. 243–247, 2007.
- [23] I. Ii, Y. Li, S. Ruan, I. Zhou, and Y. Fei, "Integrated ltcc transmitter module at ku band," *Microwave Technology and Computational Electromagnetics, 2009. ICMTCE. International Conference on*, pp. 214–217, 2009.
- [24] T. Jensen, V. Krozer, and C. Kjaergaard, "Realisation of microstrip junction circulator using LTCC technology," *Electronics Letters*, vol. 47, no. 2, pp. 111–113, 2011.
- [25] R. van Dijk, G. van der Bent, M. Ashari, and M. McKay, "Circulator integrated in low temperature co-fired ceramics technology," *European Microwave Conference 2014 Rome*, p. 1544 C 1547, 2014.
- [26] F. Ghaffar and A. Shamim, "A ferrite LTCC based dual purpose helical antenna providing bias for tunability," *Antennas and Wireless Propagation Letters, IEEE*, to be published. Early Access.
- [27] A. Shamim, J. R. Bray, N. Hojjat, and L. Roy, "Ferrite ltcc-based antennas for tunable sop applications," *IEEE Transactions on Components, Packaging and Manufacturing Technology*, vol. 1, no. 7, pp. 999–1006, 2011.
- [28] F. A. Ghaffar, J. R. Bray, and A. Shamim, "Theory and design of a tunable antenna on a partially magnetized ferrite LTCC substrate," *IEEE Trans. Antennas and Propagation*, vol. 62, no. 3, pp. 1238–1245, 2014.
- [29] E. Arabi, F. Ghaffar, and A. Shamim, "Tunable bandpass filter based on partially magnetized ferrite LTCC with embedded windings for SoP applications," *Microwave and Wireless Components Letters, IEEE*, vol. 25, no. 1, pp. 16–18, 2015.
- [30] J. Bray and L. Roy, "Development of a millimeter-wave ferrite-filled anti-symmetrically biased rectangular waveguide phase shifter embedded in low-temperature cofired ceramic," *IEEE Trans. MTT*, vol. 52, no. 7, pp. 1732–1739, 2004.
- [31] J. Adam, G. F. Dionne, E. Schloemann, and S. Stitzer, "Ferrite devices and materials," *IEEE Trans. MTT*, vol. 50, no. 3, pp. 721–737, 2002.

- [32] Ü. Özgür, Y. Alivov, and H. Morkoç, "Microwave ferrites," *Journal of Materials Sciences: Materials in Electronics*, 2009.
- [33] N. Zeina, H. How, C. Vittoria, and R. West, "Self-biasing circulators operating at ka-band utilizing m-type hexagonal ferrites," *IEEE Trans. Magnetics*, vol. 28, no. 5, pp. 3219–3221, 1992.
- [34] C. L. Hogan, "The ferromagnetic faraday effect at microwave frequencies and its applications: The microwave gyrator," vol. 31, no. 1, pp. 1–31, 1952. Bell System Technical Journal.
- [35] J. Helszajn and P. Walker, "Operation of high peak power differential phase shift circulators at direct magnetic fields between subsidiary and main resonances," *IEEE Trans. MTT*, vol. 26, no. 9, pp. 653–658, 1978.
- [36] Button and J. Kenneth, "Theoretical analysis of the operation of the field-displacement ferrite isolator," *IRE Transactions on Microwave Theory and Techniques*, vol. 6, no. 3, pp. 303–308, 1958.
- [37] H. Bosma, "On the principle of stripline circulation," *ARTICLE of the IEE-Part B: Electronic and Communication Engineering*, vol. 109, no. 21, pp. 137–146, 1962.
- [38] C. Fay and R. Comstock, "Operation of the ferrite junction circulator," *IEEE Trans. MTT*, vol. 13, no. 1, pp. 15–27, 1965.
- [39] Y. S. WU and F. J. Rosenbaum, "Wide-band operation of microstrip circulators," *IEEE Trans. MTT*, vol. 22, no. 10, pp. 849–856, 1974.
- [40] S. Ayter and Y. Ayasli, "The frequency behavior of stripline circulator junctions," *IEEE Trans. MTT*, vol. 26, no. 3, pp. 197–202, 1978.
- [41] J. Helszajn, "Frequency response of quarter-wave coupled reciprocal stripline junctions," *IEEE Trans. MTT*, vol. 21, no. 8, pp. 533–537, 1973.
- [42] E. Schloemann and R. Blight, "Broad-band stripline circulators based on yig and li-ferrite single crystals," *IEEE Trans. MTT*, vol. 34, no. 12, pp. 1394–1400, 1986.
- [43] J. Weiss, N. Watson, and G. Dionne, "New uniaxial-ferrite millimeter-wave junction circulators," *Microwave Symposium Digest, 1989., IEEE MTT-S International*, pp. 145–148, 1989.

- [44] V. Laur, G. Vérisimo, P. Queffelec, L. A. Farhat, H. Alaaeddine, J.-C. Reihls, E. Laroche, G. Martin, R. Lebourgeois, and J.-P. Ganne, “Modélisation et caractérisation d’un circulateur auto-polarisé en bande millimétrique,” *XIXèmes Journées Nationales Microondes 3-4-5 Juin 2015 - Bordeaux*, 2015.
- [45] V. Laur, J. Mattei, and P. Queffelec, “Conception et réalisation d’un circulateur en technologie siw à base de nanocomposites ferrimagnétiques,” *XIXèmes Journées Nationales Microondes 3-4-5 Juin 2015 - Bordeaux*, 2015.
- [46] T. Boyadjian, “Thesis report: Étude et réalisation dun circulateur hyperfréquence à nano particules magnétiques orientées dans la bande 40-60 ghz,” *Université Jean Monnet Saint Etienne France*, 2011.
- [47] L. G. Maloratsky, “Passive rf and microwave integrated circuits,” *Elsevier Inc*, 2004.
- [48] I. MECA Electronics, “isolators,” *official website*, 2015.
- [49] Wikipedia, “Curie temperature,” *Wikipedia*, 2015.
- [50] B. Dillon and A. Gibson, “Finite element analysis of high power differential phase shift circulators,” *Antennas and Propagation, 2001. Eleventh International Conference on (IEE Conf. Publ. No. 480)*, vol. 2, pp. 871–875, 2001.
- [51] P. J. Allen, “The turnstile circulator,” *IRE Transactions on Microwave Theory and Techniques*, vol. 4, no. 4, pp. 223–227, 1956.
- [52] M. Shalaby, M. Peccianti, Y. Ozturk, and R. Morandotti, “A non-reciprocal broadband terahertz isolator,” *Lasers and Electro-Optics (CLEO), 2013 Conference on*, pp. 1–2, 2013.
- [53] S. Ju, S. Jeong, Y. Kim, P. Watekar, and W.-T. Han, “Demonstration of all-optical fiber isolator based on a cdse quantum dots doped optical fiber operating at 660 nm,” *Journal of Lightwave Technology*, vol. 31, no. 16, pp. 2793–2798, 2013.
- [54] J. Weiss, “Circulator synthesis,” *IEEE Trans. MTT*, vol. 13, no. 1, pp. 38–44, 1965.
- [55] W. Siekanowicz, R. Paglione, and T. E. Walsh, “A latching ring-and-post ferrite waveguide circulator,” *IEEE Trans. MTT*, vol. 18, no. 4, pp. 212–216, 1970.

- [56] J. Helszajn, "A ferrite ring stripline junction circulator," *Radio and Electronic Engineer*, vol. 32, no. 1, pp. 55–60, 1966.
- [57] U. MILANO, J. H. SAUNDERS, and J. L. DAVIS, "A Y-junction strip-line circulator," *IRE Transactions on Microwave Theory and Techniques*, vol. 8, no. 3, pp. 346–351, 1960.
- [58] H. Carlin, "Non-reciprocal network theory applied to ferrite microwave devices," *ARTICLE of the IEE-Part B: Radio and Electronic Engineering*, vol. 104, no. 6, pp. 316–319, 1957.
- [59] P. D. Santis and F. Pucci, "The edge-guided-wave circulator (short papers)," *IEEE Trans. MTT*, vol. 23, no. 6, pp. 516–519, 1975.
- [60] P. Santis and F. Pucci, "Symmetrical four-port edge-guided wave circulators," *IEEE Trans. MTT*, vol. 24, no. 1, pp. 10–18, 1976.
- [61] K. Araki, T. Koyama, and Y. Naito, "New edge guided mode devices," *Microwave Symposium, 1975 IEEE-MTT-S International*, pp. 250–253, 1975.
- [62] M. Hines, "Reciprocal and nonreciprocal modes of propagation in ferrite stripline and microstrip devices," *IEEE Trans. MTT*, vol. 19, no. 5, pp. 442–451, 1971.
- [63] J. Helszajn, "The lumped element circulator," *The Stripline Circulators: Theory and Practice*, pp. 221–237, 2008.
- [64] Y. Konishi, "Lumped element Y circulator," *IEEE Trans. MTT*, vol. 13, no. 6, pp. 852–864, 1965.
- [65] C. Christensen, "Synthesis of lumped element ferrite circulators," *Microwave Conference, 1971. 2nd European*, vol. 2, pp. 1–4, 1971.
- [66] T. Wada, R. Nakajima, H. Obiwa, T. Ogami, and M. Koshino, "A miniaturized broadband lumped element circulator for reconfigurable front-end system," *Microwave Symposium (IMS), 2014 IEEE MTT-S International*, pp. 1–3, 2014.
- [67] Y. AKAIWA and T. OKAZAK, "An application of a hexagonal ferrite to a millimeter-wave Y circulator," *IEEE Trans. Magnetism*, vol. 10, no. 2, pp. 374–378, 1974.

- [68] E. Schloemann, "Circulators for microwave and millimeter-wave integrated circuits," *Proceedings of the IEEE*, vol. 76, no. 2, pp. 188–200, 1988.
- [69] D. L. Sounas, C. Caloz, and A. Al, "Giant non-reciprocity at the subwavelength scale using angular momentum-biased metamaterials," *Nat. Commun*, 2013.
- [70] I. Korn, "OQPSK and MSK systems with bandlimiting filters in transmitter and receiver and various detector filters," *IEE ARTICLE F Communications, Radar and Signal Processing*, vol. 127, no. 6, pp. 439–447, 1980.
- [71] W. Campbell and T. Parks, "Optimal design of transmitter and receiver filters with mixed performance objectives," *Acoustics, Speech, and Signal Processing, 1996. ICASSP-96. Conference ARTICLE., 1996 IEEE International Conference on*, vol. 3, pp. 1527–1529, 1996.
- [72] Wikipedia, "Isolator(microwave)," *Wikipedia*, p. 3, 2015.
- [73] B. Bayard, B. Sauviac, and D. Vincent, "Encyclopedia of rf and microwave engineering," *John Wiley and Sons, Inc*, no. 6, 2005.
- [74] E. Salonen and P. Jokela, "The effects of dry snow on reflector antennas," *Antennas and Propagation, 1991. ICAP 91., Seventh International Conference on (IEE)*, pp. 17–20, 1991.
- [75] M. Microwave, "Overview of phase shifters and switches," *MESL Microwave*, p. 3, 2015.
- [76] I. Harris and A. Williams, "Magnetic materials," *School of Metallurgy and Materials, University of Birmingham*, 2005.
- [77] Wikipedia, "Wikipedia paramagnetism," *Wikipedia*, p. 3, 2015.
- [78] Wikipedia, "Wikipedia ferromagnetism," *Wikipedia*, p. 3, 2015.
- [79] D. S. Mathew and R.-S. Juang, "An overview of magnetism of spinel nanoferrite particles and a study of chromium substituted zn-mn ferrites nanostructures via sol-gel method," *Nanoscience, Engineering and Technology (ICONSET), 2011 International Conference on*, pp. 119–124, 2011.
- [80] Wikipedia, "Wikipedia antiferromagnetism," *Wikipedia*, p. 3, 2015.

- [81] K. K. Mallick, P. Shepherd, and R. J. Green, “Magnetic properties of cobalt substituted m-type barium hexaferrite prepared by co-precipitation,” *JMMM*, 2006.
- [82] W. Kezhu, J. Renpei, and L. Shigen, “New technique of microwave ferrite and application,” *National Defense Industry Press*, 2013.
- [83] E. Schlömann, “Behavior of ferrites in the microwave frequency range,” *J. App. Phys*, vol. 41, no. 1, p. 529, 1970.
- [84] P. Gelin and K. B. Pichavant, “New consistent model for ferrite permeability tensor with arbitrary magnetization state,” *IEEE Trans. MTT*, vol. 45, no. 8, pp. 1185–1192, 1997.
- [85] G. T. Rado, “Theory of the microwave permeability tensor and faraday effect in nonsaturated ferromagnetic materials,” *Phys. Rev*, vol. 89, p. 529, 1953.
- [86] M. Igarashi and Y. Naito, “Tensor permeability of partially magnetized ferrites,” *IEEE Trans. Magnetics*, vol. 13, no. 5, pp. 1664–1668, 1977.
- [87] M. Igarashi and Y. Natio, “Parallel component u_z of partially magnetized microwave ferrites,” *IEEE Trans. MTT*, vol. 29, no. 6, pp. 568–571, 1981.
- [88] P. Gelin and P. Quéffélec, “Generalized permeability tensor model: Application to barium hexaferrite in a remanent state for self-biased circulators,” *IEEE Trans. Magnetics*, vol. 44, no. 1, pp. 24–31, 2008.
- [89] P. Quéffélec, M. L. Floc’h, and P. Gelin, “New method for determining the permeability tensor of magnetized ferrites in a wide frequency range,” *IEEE Trans. MTT*, vol. 48, no. 8, pp. 1344–1351, 2000.
- [90] P. Gelin, P. Quéffélec, and F. L. Pennec, “Effect of domain and grain shapes on the dynamical behavior of polycrystalline ferrites: Application to the initial permeability,” *IEEE Trans. MTT*, vol. 29, no. 6, pp. 568–571, 1981.
- [91] J. J.Green and F. Sandy, “Microwave characterization of partially magnetized ferrites,” *IEEE Trans. MTT*, vol. 22, no. 6, pp. 641–645, 1974.
- [92] B. Lax and K.J.Button, “Microwave ferrites and ferrimagnetics,” *McGraw-Hill New York*, 1962.
- [93] E. ElectroScience, “Esl40012 ferrite ltcc tape,” *ESL ElectroScience*, no. 6, 2015.

- [94] D. Vincent, T. Rouiller, C. Simovsky, B. Bayard, and G. Noyel, "A new broadband method for magnetic thin-film characterization in the microwave range," *IEEE Trans. MTT*, vol. 53, no. 4, pp. 1174–1180, 2005.
- [95] P.L.Fulmek, P. Haumer, I. Atassi, B.Schweighofer, and H. Wegleiter, "Magnetic DC-properties of LTCC-ferrite material and their temperature dependence," *IEEE Trans. Magnetism*, vol. 48, no. 4, pp. 1541–1544, 2012.
- [96] J. R. Bray, K. T. Kautio, and L. Roy, "Characterization of an experimental ferrite LTCC tape system for microwave and millimeter-wave applications," *IEEE Trans. Advanced Packaging*, vol. 27, no. 3, pp. 558–565, 2004.
- [97] F. Ghaffar and A. Shamim, "A ferrite LTCC based dual purpose helical antenna providing bias for tunability," *Antennas and Wireless Propagation Letters, IEEE*, vol. 14, pp. 831–834, 2015.
- [98] A. Abdul Ghaffar, F. ; Shamim, "A partially magnetized ferrite LTCC based siw phase shifter for phased array applications," *IEEE Trans. Magnetism*, to be published. Early Access.
- [99] E. Arabi and A. Shamim, "The effect of self-heating on the performance of a tunable filter with embedded windings in a ferrite LTCC package," *IEEE Transactions on Components, Packaging and Manufacturing Technology*, vol. 5, no. 3, pp. 365–371, 2015.
- [100] H. J. Carlin, "Principles of gyrator networks," *Proc. Modern Advances in Microwave Tech. Symp*, pp. 175–204, 1954.
- [101] B. A. Auld, "The synthesis of symmetrical waveguide circulators," *IRE Transactions on Microwave Theory and Techniques*, vol. 7, no. 2, pp. 238–246, 1959.
- [102] G. Buehler and A. Eikenberg, "Stripline Y-circulator for the 100 to 400 mc region," *Proc. IRE*, vol. 49, p. 518, 1961.
- [103] J. Clark, "Perturbation techniques for miniaturized coaxial Y- junction circulator," *Journal of Applied Physics*, vol. 32, p. 3238, 1961.
- [104] L. Davis, U. Milano, and J. Saunders, "A stripline L-band compact circulator," *Proc. IRE*, vol. 48, p. 115, 1960.
- [105] S. Yoshida, "Stripline Y-circulator," *Proc. IRE*, vol. 48, p. 1664, 1960.

- [106] M. Grace and F. Arams, "Three-port ring circulators," *Journal of Applied Physics*, vol. 48, p. 1497, 1960.
- [107] J. Pippin, "Microwave ferrite device," *Microwave Journal*, vol. 11, pp. 29–45, 1960.
- [108] J. S. Chang, "Master report: The design of three-port strip line circulator," *University of Missouri Rolla-USA*, 1969.
- [109] D.D.Grieg and H.F.Englemann, "Microstrip-a new transmission technique for the kilomegacycle range," *Proceedings of the IRE*, vol. 40, no. 12, pp. 1644–1650, 1952.
- [110] B. Hershenov, "X-band microstrip circulator," *Proceedings of the IEEE*, vol. 54, no. 12, pp. 2022–2023, 1966.
- [111] R. Trambarulo, "A 30-GHz inverted-microstrip circulator (correspondence)," *IEEE Trans. MTT*, vol. 19, no. 7, pp. 662–664, 1971.
- [112] B. Peng, W. Zhang, Y. Sun, J. Lin, W. Zhang, and H. Li, "Design of microstrip Y-junction circulator based on ferrite thin films," *Microwave Conference Proceedings (CJMW), 2011 China-Japan Joint*, pp. 1–4, 2011.
- [113] W. Peng, Bin; Huizhong Xu; Hui Li; Wenxu Zhang; Yuan Wang; Zhang, "Self-biased microstrip junction circulator based on barium ferrite thin films for monolithic microwave integrated circuits," *IEEE Trans. Magnetics*, vol. 47, no. 6, pp. 1674–1677, 2011.
- [114] C. P. Wen, "Coplanar waveguide, a surface strip transmission line suitable for nonreciprocal gyromagnetic device applications," *Microwave Symposium, 1969 G-MTT International*, pp. 110–115, 1969.
- [115] B. Bayard, D. Yincen, C. R. Simovski, and G. Noyel, "Electromagnetic study of a ferrite coplanar isolator suitable for integration," *IEEE Trans. MTT*, vol. 51, no. 7, pp. 1809–1814, 2003.
- [116] N. Ogasawara and M. Kaji, "Coplanar-guide and slot-guide junction circulators," *Electronics Letters*, vol. 7, no. 9, pp. 220–221, 1971.
- [117] B. Wang, Y.and Peng and W.-L. Zhang, "Simulation of self-biased coplanar circulator using barium ferrite thin films," *Microwave and Millimeter Wave Technology (ICMMT), 2010 International Conference on*, pp. 543–546, 2010.

- [118] T. Boyajian, D. Vincent, S. Neveu, M. LeBerre, and J. Rousseau, “Coplanar circulator made from composite magnetic material,” *Microwave Symposium Digest (MTT), 2011 IEEE MTT-S International*, 2011.
- [119] J. B. Davies and P. Cohen, “Theoretical design of symmetrical junction stripline circulators,” *IEEE Trans. MTT*, vol. 11, no. 6, pp. 506–512, 1963.
- [120] R. E. Neidert and P. M. Phillips, “Losses in Y-junction stripline and microstrip ferrite circulators,” *IEEE Trans. MTT*, vol. 41, no. 6, pp. 1081–1086, 1993.
- [121] C. K. Seewald and J. R. Bray, “Ferrite-filled antisymmetrically biased rectangular waveguide isolator using magnetostatic surface wave modes,” *IEEE Trans. MTT*, vol. 58, no. 6, pp. 1493–1501, 2010.
- [122] S. Yang, D. Vincent, J. R. Bray, and L. Roy, “Ferrite ltcc edge-guided circulator,” *European Microwave Conference 2014, Rome*, 2014.
- [123] R. Soohoo, “Theory and application of ferrites, englewood cliffs, nj:prentice-hall,1960, pp 83–111,” *Englewood Cliffs, NJ:Prentice-Hall*, pp. 83–111, 1960.
- [124] S. Yang, L. Roy, J. R. Bray, and D. Vincent, “Modeling and simulation of a partially-magnetized ferrite ltcc circulator,” *IEEE-MTT-Numerical Electromagnetic and Multiphysics Modeling and Optimization for RF, Microwave, and Terahertz Applications*, 2015.

Publications

Journal

Shicheng Yang; Vincent, D.; Bray, J.R.; Roy, L., "Study of a Ferrite LTCC Multifunctional Circulator With Integrated Winding," in Components, Packaging and Manufacturing Technology, IEEE Transactions on , vol.5, no.7, pp.879-886, July 2015, doi: 10.1109/TCPMT.2015.2440660)

International Conferences

Shicheng Yang; Vincent, D.; Bray, J.R.; Roy, L., "Ferrite LTCC edge-guided circulator," in Microwave Conference (EuMC), 2014 44th European , vol., no., pp.1540-1543, 6-9 Oct. 2014, doi: 10.1109/EuMC.2014.6986743

Modeling and Simulation of a Partially-Magnetized Ferrite LTCC Circulator", IEEE Numerical Electromagnetic and Multiphysics Modeling and Optimization for RF, Microwave, and Terahertz Applications, August, Ottawa, Canada, 2015

National Conference

Shicheng Yang, Didier Vincent, Joey R Bray, Langis Roy, "Circulateur LTCC Ferrite large-bande à structures empilées en bande K", 19èmes Journées Nationales Micro-ondes, 2015, Bordeaux, France, 2015

Appendix A

S-parameters calculation

Calculation of S-parameters (Stripline Circulators)

Before calculation:

$$\mu_0 = 4\pi \times 10^{-7} \text{ H/m}$$

$$\epsilon_0 = 8.854 \times 10^{-12} \text{ F/m}$$

$$\epsilon_f = 14.6 \text{ \% relative permittivity of ferrite}$$

$$\epsilon_d = 14.6 \text{ \% relative permittivity of dielectric}$$

The roots of $J_n'(x) = 0$ are:

$$\left\{ \begin{array}{l} x_{11} = 1.84118378134066 \\ x_{21} = 3.054232692822714 \\ x_{31} = 4.201 \\ x_{12} = 5.33144277352503 \end{array} \right.$$

$$\omega_c = 2\pi f_c \text{ \% circulator's operating frequency.}$$

Tensor of Polder:

$$M_s = 4000 \text{ Gauss}$$

$$H_i \text{ \% internal } H_i \text{ field.}$$

$$\alpha = 0.35 \text{ \% damping factor}$$

$$\gamma = 2\pi \times 28 \times 10^9 = 1.759 \times 10^{11} \text{ c/kg}$$

$$\Rightarrow \omega_m = \gamma \mu_0 M_s$$

$$\omega_r = \mu_0 H_0 \gamma$$

$$\left\{ \begin{array}{l} \mu = \frac{(\omega_r + j\alpha\omega)\omega_m}{(\omega_r + j\alpha\omega)^2 - \omega^2} + 1 \\ k = \frac{\omega\omega_m}{(\omega_r + j\alpha\omega)^2 - \omega^2} \end{array} \right.$$

$$[\mu] = \begin{bmatrix} \mu & jk & 0 \\ -jk & \mu & 0 \\ 0 & 0 & 1 \end{bmatrix} \Leftarrow \text{z biased.}$$

We can also calculate:

$$\mu_{\text{eff}} = \frac{\mu^2 - k^2}{\mu}$$

$$k_c = \omega_c \sqrt{\epsilon_0 \mu_0 \epsilon_f \mu_{\text{eff}}} \quad \Delta k_c \text{ is not } k.$$

$$Z_{\text{eff}} = \sqrt{\frac{\mu_0 \mu_{\text{eff}}}{\epsilon_0 \epsilon_f}}$$

$$R = \frac{\kappa_{11}}{k_c} \quad \% \text{ the radius of ferrite/circulator}$$

(mode I, we can also use $\kappa_{21}, \kappa_{31}, \dots$ for other modes).

$$k_d = \omega_c \sqrt{\epsilon_0 \mu_0 \epsilon_d} \quad \% \text{ propagation constant in dielectric.}$$

$$Z_{d0} = \frac{120\pi}{\sqrt{\epsilon_d}}$$

$$\psi_c = \frac{\pi}{\sqrt{3} (1.84)} \frac{Z_d}{Z_{\text{eff}}} \left| \frac{\mu}{R} \right| \quad \% \text{ coupling angle.}$$

Calculation begins:

Green function:

$$G(r, \phi; R, \phi') = -\frac{i Z_{\text{eff}} J_0(kr)}{2\pi J_0'(x)} + \frac{Z_{\text{eff}}}{\pi} \sum_{n=1}^{\infty} \frac{\frac{k}{\mu} \frac{n J_n(x)}{x} \sin n(\phi - \phi') - i J_n'(x) \cos n(\phi - \phi')}{[J_n'(x)]^2 - \left[\frac{k}{\mu} \frac{n J_n(x)}{x} \right]^2} J_n(kr)$$

Magnetic wall boundary condition is applied:

$$H\phi = \begin{cases} H_1 & -\frac{\pi}{3} - \psi < \phi < -\frac{\pi}{3} + \psi \\ H_2 & \frac{\pi}{3} - \psi < \phi < \frac{\pi}{3} + \psi \\ H_3 & \pi - \psi < \phi < \pi + \psi \end{cases}$$

Then :

$$E_z(R, \phi') = \int_C G(\phi|\phi') H_\phi(R, \phi') d\phi$$

\Rightarrow Impedance at each port :

$$\eta(\phi|\phi_0) = \frac{E_z(R, \phi_0)}{H_\phi(R, \phi_0)} = \int_C G(\phi|\phi_0) d\phi$$

\Rightarrow The observation port is assumed to be $\phi_0 = -\frac{\pi}{3}$

$$\text{So } \eta_{11} = \int_C G(\phi|-\frac{\pi}{3}) d\phi \quad -\frac{\pi}{3} - \psi < \phi < -\frac{\pi}{3} + \psi$$

$$\hookrightarrow \eta_{11} = \int_{-\frac{\pi}{3} - \psi}^{-\frac{\pi}{3} + \psi} G(\phi|-\frac{\pi}{3}) d\phi$$

Assume that :

$$A = \frac{Z_{eff}}{\pi} \frac{\frac{k}{\mu} \frac{n J_n(x)}{x}}{[J_n'(x)]^2 - [\frac{k}{\mu} \frac{n J_n(x)}{x}]^2} J_n(kr)$$

$$B = \frac{Z_{eff}}{\pi} \frac{i J_n'(x)}{[J_n'(x)]^2 - [\frac{k}{\mu} \frac{n J_n(x)}{x}]^2} J_n(kr)$$

$$a_0 = - \frac{i Z_{eff} J_0(kr)}{2\pi J_0'(x)}$$

$$\begin{aligned}
 \eta_{11} &= \int_{-\frac{\pi}{3}-\psi}^{-\frac{\pi}{3}+\psi} a_0 d\phi + \int_{-\frac{\pi}{3}-\psi}^{-\frac{\pi}{3}+\psi} A \sin n(\phi + \frac{\pi}{3}) - B \cos n(\phi - \frac{\pi}{3}) d\phi \\
 &= 2\psi a_0 + \left. -\frac{A}{n} \cos n(\phi + \frac{\pi}{3}) \right|_{-\frac{\pi}{3}-\psi}^{-\frac{\pi}{3}+\psi} - \left. \frac{B}{n} \sin n(\phi + \frac{\pi}{3}) \right|_{-\frac{\pi}{3}-\psi}^{-\frac{\pi}{3}+\psi} \\
 &= 2\psi a_0 - \frac{A}{n} [\cos n\psi - \cos(-n\psi)] - \frac{B}{n} [\sin n(\psi) - \sin(-n\psi)] \\
 &= 2\psi a_0 - 2B\psi \operatorname{sinc}(n\psi)
 \end{aligned}$$

$$\begin{aligned}
 \eta_{21} &= \int_{\frac{\pi}{3}-\psi}^{\frac{\pi}{3}+\psi} G(\phi | -\frac{\pi}{3}) d\phi \\
 &= \int_{\frac{\pi}{3}-\psi}^{\frac{\pi}{3}+\psi} a_0 d\phi + \int_{\frac{\pi}{3}-\psi}^{\frac{\pi}{3}+\psi} A \sin n(\phi + \frac{\pi}{3}) - B \cos n(\phi + \frac{\pi}{3}) d\phi \\
 &= 2\psi a_0 - \left. \frac{A}{n} \cos n(\phi + \frac{\pi}{3}) \right|_{\frac{\pi}{3}-\psi}^{\frac{\pi}{3}+\psi} - \left. \frac{B}{n} \sin n(\phi + \frac{\pi}{3}) \right|_{\frac{\pi}{3}-\psi}^{\frac{\pi}{3}+\psi} \\
 &= 2\psi a_0 - \frac{A}{n} [\cos n(\frac{2\pi}{3} + \psi) - \cos n(\frac{2\pi}{3} - \psi)] - \frac{B}{n} [\sin n(\frac{2\pi}{3} + \psi) - \sin n(\frac{2\pi}{3} - \psi)] \\
 &= 2\psi a_0 - \frac{A}{n} (-2 \sin \frac{2n\pi}{3} \operatorname{sinc} n\psi) - \frac{B}{n} (2 \cos \frac{2n\pi}{3} \operatorname{sinc} n\psi) \\
 &= 2\psi a_0 + 2\psi [A \sin \frac{2n\pi}{3} \operatorname{sinc}(n\psi) - B \cos \frac{2n\pi}{3} \operatorname{sinc}(n\psi)] \\
 &= 2\psi a_0 + 2\psi \operatorname{sinc}(n\psi) [A \sin \frac{2n\pi}{3} - B \cos \frac{2n\pi}{3}]
 \end{aligned}$$

$$\begin{aligned}
 \eta_{31} &= \int_{\pi-\psi}^{\pi+\psi} G(\phi | -\frac{\pi}{3}) d\phi \\
 &= \int_{\pi-\psi}^{\pi+\psi} a_0 d\phi + \int_{\pi-\psi}^{\pi+\psi} A \sin n(\phi + \frac{\pi}{3}) - B \cos n(\phi + \frac{\pi}{3}) d\phi \\
 &= 2\psi a_0 - \left. \frac{A}{n} \cos n(\phi + \frac{\pi}{3}) \right|_{\pi-\psi}^{\pi+\psi} - \left. \frac{B}{n} \sin n(\phi + \frac{\pi}{3}) \right|_{\pi-\psi}^{\pi+\psi} \\
 &= 2\psi a_0 - \frac{A}{n} [\cos n(\frac{4\pi}{3} + \psi) - \cos n(\frac{4\pi}{3} - \psi)] - \frac{B}{n} [\sin n(\frac{4\pi}{3} + \psi) - \sin n(\frac{4\pi}{3} - \psi)] \\
 &= 2\psi a_0 + 2\psi \operatorname{sinc}(n\psi) [A \sin \frac{4n\pi}{3} - B \cos \frac{4n\pi}{3}]
 \end{aligned}$$

The final results of $[\eta]$ is :

$$\eta_{11} = -\frac{i Z_{eff} J_0(kr)}{2\pi J_0'(x)} 2\psi + \frac{Z_{eff}}{\pi} \sum_{n=1}^{\infty} \frac{-i 2 J_n'(x) \psi \operatorname{sinc}(n\psi)}{[J_n'(x)]^2 - \left[\frac{k}{u} \frac{n J_n(x)}{x}\right]^2} J_n(kr)$$

$$\eta_{21} = -\frac{i Z_{eff} J_0(kr)}{2\pi J_0'(x)} 2\psi + \dots + \frac{Z_{eff}}{\pi} \sum_{n=1}^{\infty} \frac{2\psi \operatorname{sinc}(n\psi) \left[\frac{k}{u} \frac{n J_n(x)}{x} \sin \frac{2n\pi}{3} - i J_n'(x) \cos \frac{2n\pi}{3} \right]}{[J_n'(x)]^2 - \left[\frac{k}{u} \frac{n J_n(x)}{x}\right]^2} J_n(kr).$$

$$\eta_{31} = -\frac{i Z_{eff} J_0(kr)}{2\pi J_0'(x)} 2\psi + \dots + \frac{Z_{eff}}{\pi} \sum_{n=1}^{\infty} \frac{2\psi \operatorname{sinc}(n\psi) \left[\frac{k}{u} \frac{n J_n(x)}{x} \sin \frac{4n\pi}{3} - i J_n'(x) \cos \frac{4n\pi}{3} \right]}{[J_n'(x)]^2 - \left[\frac{k}{u} \frac{n J_n(x)}{x}\right]^2} J_n(kr)$$

$$[\eta] = \begin{bmatrix} \eta_{11} & \eta_{31} & \eta_{21} \\ \eta_{21} & \eta_{11} & \eta_{31} \\ \eta_{31} & \eta_{21} & \eta_{11} \end{bmatrix} \xrightarrow[\substack{\text{Normalized by} \\ Z_0 = \frac{120\pi}{\sqrt{\epsilon_d}}}}{[Z]} = \begin{bmatrix} Z_{11} & Z_{31} & Z_{21} \\ Z_{21} & Z_{11} & Z_{31} \\ Z_{31} & Z_{21} & Z_{11} \end{bmatrix}$$

Now we calculate the $[S]$ by $[S] = [Z+I]^{-1} [Z+I]$

$$[Z+I] = \begin{bmatrix} Z_{11}+1 & Z_{31} & Z_{21} \\ Z_{21} & Z_{11}+1 & Z_{31} \\ Z_{31} & Z_{21} & Z_{11}+1 \end{bmatrix}$$

$$[Z+I]^{-1} = \frac{1}{\det(Z+I)} \operatorname{adj}(Z+I)$$

$$\operatorname{adj}(Z+I) = \begin{bmatrix} (Z_{11}+1)^2 - Z_{21} Z_{31} & Z_{21}^2 - Z_{31}(Z_{11}+1) & Z_{31}^2 - Z_{21}(Z_{11}+1) \\ Z_{31}^2 - Z_{21}(Z_{11}+1) & (Z_{11}+1)^2 - Z_{21} Z_{31} & Z_{21}^2 - Z_{31}(Z_{11}+1) \\ Z_{21}^2 - Z_{31}(Z_{11}+1) & Z_{31}^2 - Z_{21}(Z_{11}+1) & (Z_{11}+1)^2 - Z_{21} Z_{31} \end{bmatrix}$$

if $A = (Z_{11}+1)^2 - Z_{21} Z_{31}$

$B = Z_{31}^2 - Z_{21}(Z_{11}+1)$

$C = Z_{21}^2 - Z_{31}(Z_{11}+1)$.

$$[Z+I]^* = \begin{bmatrix} A & c & B \\ B & A & c \\ c & B & A \end{bmatrix}$$

$$\det |Z+I| = (z_{11}+1)^3 + z_{21}^3 + z_{31}^3 - 3(z_{11}+1)z_{21}z_{31}$$

$$[S] = [Z+I]^{-1} [Z-I]$$

$$= \frac{1}{\det |Z+I|} \begin{bmatrix} A & c & B \\ B & A & c \\ c & B & A \end{bmatrix} \begin{bmatrix} z_{11}-1 & z_{31} & z_{21} \\ z_{21} & z_{11}-1 & z_{31} \\ z_{31} & z_{21} & z_{11}-1 \end{bmatrix}$$

$$= \frac{1}{\det |Z+I|} \begin{bmatrix} A(z_{11}-1) + Cz_{21} + Bz_{31} & Az_{31} + C(z_{11}-1) + Bz_{21} & Az_{21} + C(z_{31} + B(z_{11}-1)) \\ B(z_{11}-1) + Az_{21} + Cz_{31} & Bz_{31} + A(z_{11}-1) + Cz_{21} & Bz_{21} + Az_{31} + C(z_{11}-1) \\ C(z_{11}-1) + Bz_{21} + Az_{31} & Cz_{31} + B(z_{11}-1) + Az_{21} & Cz_{21} + Bz_{31} + A(z_{11}-1) \end{bmatrix}$$

\Rightarrow

$$S_{11} = \frac{1}{\det |Z+I|} [A(z_{11}-1) + Cz_{21} + Bz_{31}]$$

$$= \frac{1}{\det |Z+I|} \left\{ [(z_{11}+1)^2 - z_{21}z_{31}] (z_{11}-1) + z_{21}^3 - z_{21}z_{31}(z_{11}+1) + z_{31}^3 - z_{31}z_{21}(z_{11}+1) \right\}$$

$$= \frac{1}{\det |Z+I|} \left\{ [(z_{11}+1)^2 - z_{21}z_{31}] (z_{11}+1) - 2[(z_{11}+1)^2 - z_{21}z_{31}] + z_{21}^3 - z_{21}z_{31}(z_{11}+1) + z_{31}^3 - z_{21}z_{31}(z_{11}+1) \right\}$$

$$= 1 + \frac{-2}{\det |Z+I|} [(z_{11}+1)^2 - z_{21}z_{31}]$$

$$= 1 + \frac{-2 [(z_{11}+1)^2 - z_{21}z_{31}] z_d}{(z_{11}+1)^3 + z_{21}^3 + z_{31}^3 - 3z_{21}z_{31}(z_{11}+1)}$$

$$\begin{aligned}
 S_{21} &= \frac{1}{\det |z+I|} [B(z_{11}-1) + A z_{21} + C z_{31}] \\
 &= \frac{1}{\det |z+I|} \left\{ [z_{31}^2 - z_{21}(z_{11}+1)](z_{11}+1) - 2[z_{31}^2 - z_{21}(z_{11}+1)] + [(z_{11}+1)^2 - z_{21}z_{31}]z_{21} \right. \\
 &\quad \left. + [z_{21}^2 - z_{31}(z_{11}+1)]z_{31} \right\} \\
 &= \frac{1}{\det |z+I|} \left\{ -2[z_{31}^2 - z_{21}(z_{11}+1)] \right\} \\
 &= - \frac{2[z_{31}^2 - z_{21}(z_{11}+1)]z_d}{(z_{11}+1)^3 + z_{21}^3 + z_{31}^3 - 3z_{21}z_{31}(z_{11}+1)}
 \end{aligned}$$

$$\begin{aligned}
 S_{31} &= \frac{1}{\det |z+I|} [C(z_{11}-1) + B z_{21} + A z_{31}] \\
 &= \frac{1}{\det |z+I|} \left\{ [z_{21}^2 - z_{31}(z_{11}+1)](z_{11}+1) - 2[z_{21}^2 - z_{31}(z_{11}+1)] + z_{31}^2 z_{21} - z_{21}^2(z_{11}+1) \right. \\
 &\quad \left. + z_{31}(z_{11}+1)^2 - z_{21}z_{31}^2 \right\} \\
 &= - \frac{2[z_{21}^2 - z_{31}(z_{11}+1)]z_d}{(z_{11}+1)^3 + z_{21}^3 + z_{31}^3 - 3z_{21}z_{31}(z_{11}+1)}
 \end{aligned}$$

$$\Rightarrow S = \begin{bmatrix} S_{11} & S_{31} & S_{21} \\ S_{21} & S_{11} & S_{31} \\ z S_{31} & S_{21} & S_{11} \end{bmatrix}$$

Let's :

$$\begin{aligned}
 C_1 &= j\pi \frac{z_{11}+1}{2z_{\text{eff}}} & \Rightarrow z_{11}+1 &= \frac{2C_1 z_{\text{eff}}}{j\pi} \\
 C_2 &= j\pi \frac{z_{31}}{2z_{\text{eff}}} & \Rightarrow z_{31} &= \frac{2C_2 z_{\text{eff}}}{j\pi} \\
 C_3 &= j\pi \frac{z_{21}}{2z_{\text{eff}}} & \Rightarrow z_{21} &= \frac{2C_3 z_{\text{eff}}}{j\pi}
 \end{aligned}$$

$$S_{11} = 1 + \frac{-2 [(z_{11}+1)^2 - z_{21} z_{31}] z_d}{(z_{11}+1)^3 + z_{21}^3 + z_{31}^3 - 3 z_{21} z_{31} (z_{11}+1)}$$

$$= 1 + (-2) \frac{1}{\frac{2 z_{eff}}{j\pi z_d}} \cdot \frac{C_1^2 - C_2 C_3}{C_1^3 + C_2^3 + C_3^3 - 3 C_1 C_2 C_3}$$

$$= 1 + \frac{\pi z_d}{j z_{eff}} \frac{C_1^2 - C_2 C_3}{C_1^3 + C_2^3 + C_3^3 - 3 C_1 C_2 C_3}$$

$$S_{21} = \frac{-2 [z_{31}^2 - z_{21} (z_{11}+1)] z_d}{(z_{11}+1)^3 + z_{21}^3 + z_{31}^3 - 3 z_{21} z_{31} (z_{11}+1)}$$

$$= -2 \times \frac{j\pi z_d}{2 z_{eff}} \cdot \frac{C_2^2 - C_1 C_3}{C_1^3 + C_2^3 + C_3^3 - 3 C_1 C_2 C_3}$$

$$= \frac{\pi z_d}{j z_{eff}} \frac{C_2^2 - C_1 C_3}{C_1^3 + C_2^3 + C_3^3 - 3 C_1 C_2 C_3}$$

$$\Rightarrow S_{31} = \frac{\pi z_d}{j z_{eff}} \frac{C_3^2 - C_1 C_2}{C_1^3 + C_2^3 + C_3^3 - 3 C_1 C_2 C_3}$$

$$[S] = \begin{bmatrix} S_{11} & S_{31} & S_{21} \\ S_{21} & S_{11} & S_{31} \\ S_{31} & S_{21} & S_{11} \end{bmatrix}$$

RESUME

Composants passifs non réciproques hyperfréquences sur substrat ferrite LTCC

Cette thèse concerne de l'étude de composants passifs non-réciproque (circulateurs) fabriqué sur substrat LTCC ferrite. Les aimants externes utilisés dans les circulateurs classiques doivent créer un champ magnétique intense pour compenser le champs de démagnétisant dans le ferrite. Le nouveau circulateur présenté ici utilise une bobine intégrée dans le LTCC ferrite pour magnétiser le matériau de l'intérieur, pour réduire considérablement les effets des champs démagnétisants. Il est possible de contrôler le champ de polarisation rendant le dispositif multifonctionnel: lorsque la bobine est excitée par un courant, le dispositif fonctionne comme un circulateur dynamique dans lequel la direction de circulation peut être basculée en changeant la direction du courant. Si un aimant externe est placé sur le circulateur, sa fréquence de fonctionnement peut être accordée en ajustant le courant de polarisation. Contrairement à d'autres circulateurs LTCC avec aimants externes, le dispositif proposé peut même fonctionner comme un diviseur de puissance sans courant de polarisation. Un prototype de circulateur a été réalisé et caractérisé dans trois états: 1. démagnétisé, 2. magnétisé par la bobine, 3. magnétisé par la bobine et des aimants externes. En l'absence de courant appliqué, la transmission de chaque port est d'environ -5 dB avec un coefficient de réflexion inférieur à -20 dB à 14,8 GHz. Quand un courant de 300 mA est injecté dans la bobine, les pertes d'insertion et l'isolation mesurées sont d'environ 3 dB et 8 dB, respectivement. Le coefficient de réflexion est inférieur à -20 dB à 14,2 GHz. Lorsque les aimants externes sont ajoutés avec un courant de 200 mA, les pertes d'insertion et l'isolation a été améliorée à 1,6 dB et 23 dB, respectivement à 14,2 GHz. La variation de la fréquence de travail du circulateur est de 0,6 GHz. Elle est due par la variation de l'aimantation M interne lorsque le courant est inférieur à 120 mA, puis par l'augmentation de la température créée par le courant dans la bobine. La taille (L * W * H) totale du circulateur réalisé est de 8mm * 8mm * 1.1mm. Ce travail montre qu'il est possible d'intégrer (MMIC) sur un substrat LTCC ferrite des circuits passifs non-réciproques.

ABSTRACT

Non reciprocal passive components on LTCC ferrite substrate

This thesis investigates passive non-reciprocal components (mainly circulators) based on ferrite Low Temperature Co-fired Ceramic (LTCC) substrate. The external magnets used in conventional circulators must be strong to overcome the ferrite's demagnetization field. The novel circulator presented herein uses an embedded winding within the ferrite substrate to magnetize the material from the inside, thereby significantly reducing the demagnetization effects. Because of the controllability of the bias field, the resulting device is also multifunctional: when the windings are energized by a current, the device operates as a dynamic circulator in which the circulation direction can be changed by switching the direction of the current. Unlike other LTCC circulators with external magnets, the proposed device can even operate as a power splitter by removing the bias current. A circulator prototype has been characterized in three states: unbiased, biased by winding and biased by winding and external magnets. When no current is applied, the transmission of each port is about -5 dB with return loss better than 20 dB at 14.8 GHz. When a current of 300 mA is injected into the winding, the measured insertion loss and isolation of the circulator is approximately 3 dB and 8 dB, respectively, whereas the return loss is better than 20 dB at 14.2 GHz. When external magnets are added in addition to the current of 200 mA, the insertion loss and isolation is improved to 1.6 dB and 23 dB, respectively at 14.2 GHz. The variation of the circulator's working frequency is 0.6 GHz. This is achieved firstly by the change of internal magnetization M when current is less than 120 mA, then the heat in the substrate due to the winding introduces more frequency shifting. The total size (L*W*H) is 8mm*8mm*1.1mm.